METHODS FOR COMPUTING CURRENT PROFILES;
applied on tidal currents in the Barents sea

by

ELISABETH NØST

Department of Mathematics University of Oslo
P.O.Box 1053 Blindern Oslo Norway

January 25, 1992

Abstract

The method of extracting current profiles from vertically integrated hydrodynamic models, developed by A.M.Davies (1987, 1990), is extended to incorporate more general boundary conditions, and the consistency of the method is closely investigated.
By using this method the tidal current profiles are studied in view of variations of water depth, geographical latitude, surface boundary condition and different vertical variations of the eddy viscosity.
The current profiles are then computed at eight special chosen stations where there exists current measurements in up to six different depths which the computed profiles are compared with. The observation stations are located in the Barents sea close to the critical latitude for the largest semi-diurnal constituents and the current profiles are therefore sensitive for variations of magnitude and vertical distribution of the eddy viscosity. In four of the stations there are under-ice measurements and the effects of an ice covered ocean has upon the tidal currents profiles are also investigated.

Contents

1 Introduction 2
2 Basic equations 4
2.1 Equations of motion 4
2.2 Boundary conditions 6
2.3 Turbulent closure approximations 7
3 Numerical methods 10
3.1 Computation procedure 10
3.2 The Galerkin method 10
3.2.1 Ice covered ocean surface 13
3.2.2 Free ocean surface 14
3.3 Numerical solution of the eigenvalue problem 14
4 Tidal flow 20
4.1 Equations of motion in rotary form 20
4.2 Analytical solution 23
4.3 Turbulent boundary layer thickness 24
4.4 Numerical solution 25
4.4.1 Solution using the Galerkin method 25
4.4.2 Consistency of the method 27
4.5 Current profile calculations 28
4.5.1 Parameter dependence 28
4.5.2 Accuracy of the numerical solution 31
5 Tidal current profiles in the Barents sea 39
5.1 Tidal current profiles under a free ocean surface 40
5.2 Tidal current profiles under an ice covered ocean surface 45
6 Conclusions 60

1. Introduction

The two-dimensional depth integrated numerical ocean models are well established and extensively used to study the tidal dynamics. The model may cover large global oceans (Schwiderski, 1980) or smaller limited ocean regions (Gjevik et al. 1990, Flather 1976). The results from these models are the sea elevation and the depth mean current with no information about the tidal current profiles i.e. how the tidal current varies with depth.

To study in detail the vertical structure of the tidal currents, several three-dimensional tidal models (Davies and Furnes 1980, Davies and Jones 1990, etc.) have been developed. They give in addition to the sea elevation the tidal current depth distributions as results, and enables a comparison with current observations from arbitrary depth in the water column. The three-dimensional numerical models require significantly greater computational resources (computer time and memory) than their two-dimensional equivalents.

An alternative approach is to use the method for extracting current profiles from depth integrated models. This method makes it possible to study the vertical structure of the currents with less computational resources than required in the full three-dimensional models. This method for extracting current profiles is developed by A.M. Davies and are presented for wind driven currents in Davies (1986) and for tidal driven motion in Davies (1990), the former with full time dependency and in the latter the time dependency is removed due to the periodic nature of the tidal motion. The method may incorporate a prescribed arbitrary depth distribution of the eddy viscosity.

In this paper we shall extend Davies method to incorporate more general boundary conditions, including the effect of an ice covered ocean surface. Tidal current profiles will be studied in view of variations of water depth, geographical latitude, surface boundary condition and different vertical variations of the eddy viscosity.
The latitudes where the Coriolis frequency equals the tidal frequency are called the critical latitude for the considered tidal constituent. For the semi-diurnal M_2 tide the critical latitudes are 75°2.8' North and South, and for the diurnal K_1 tide they are 30°5.4' North and South. Further more we have applied the method to data from stations located near the critical latitude for the largest semi-diurnal constituents and to data under an ice covered surface.

In section 2. the basic equations are given. Firstly, in 2.1., the equations of motion are presented. These are the linearized shallow water equations for homogeneous sea and are suitable when studying the tidal dynamics in an ocean region. The total current can be written as a depth mean part and a deviation from this. The equations of motion can then be divided in a similar manner, and we obtain two sets of equations which are coupled together through the boundary conditions i.e. the shear stresses at the boundaries. The set of equations for the depth mean part of the total current is the starting point for the two dimensional vertically integrated model, and the equations for the deviation current is the starting point for the current profile calculations. When turbulence is included the equations of motion are unfortunately not closed, and closure assumptions must be made. Various boundary conditions and turbulence closure approximations devised for the tidal boundary layer are presented in section 2.2. and 2.3. respectively.
In section 3. the numerical methods are described, where we in 3.1. give a overview description

of the total computation procedure for the method of extracting current profiles from two dimensional vertically integrated models. The starting point for the computation procedure is the splitting of the equations of motion in a depth mean part and a deviation from this. A detailed description of numerical methods used for the depth averaged equations i.e. the first step in the computation procedure, will not be given in this work. Here we will concentrate on describing the numerical method for the the solution in the vertical i.e. the solution of the deviation part of the equations of motion. A full time dependent description using a Galerkin expansion in the vertical are given in section 3.2. This description includes various bed and surface boundary conditions for currents under a free ocean surface and under an ice covered ocean surface.
In section 4. a special version of the method for the periodic tidal flow is presented. The time dependency is removed and instead the equation for the rotary components of the periodic flow is solved. This form of the method cannot incorporate a time varying eddy viscosity. In this section the consistency requirements of the method is presented in detail and a parameter study of the influence of water depth, geographical latitude, eddy viscosity magnitude upon the tidal current are given. A similar parameter dependency study is done by Davies (1985) for oscillatory flow except for the influence of geographical latitude upon the tidal current profiles. For the current profile calculations with a constant eddy viscosity there exists an analytical solution and hence the accuracy of the method are investigated.

In section 5. we have applied the method for extracting current profiles from a depth integrated model to compute tidal currents in the Barents Sea. This area includes the critical latitude of the largest semi-diurnal constituents and is partly covered with ice several months of the year. The tidal current profile calculations are carried out at positions in the Barents sea where we have current measurements in up to six different depths which the computed profiles are compared with and four of these stations have under-ice measurements. The profile calculations are carried out with suitable boundary conditions and with different eddy viscosity profiles.

2. Basic equations

2.1. Equations of motion

We shall apply a f-plane approximation for the Coriolis force and introduce a Cartesian coordinate system x, y, z with the z- axis in the vertical direction and the x and y axis in the horizontal undisturbed sea surface. The linearized shallow water equations for a homogeneous sea reads

$$\frac{\partial u}{\partial t} - f\, v = -g\frac{\partial}{\partial x}(\eta - \tilde{\eta}) + l_x + \frac{\partial}{\partial z}(\nu\frac{\partial u}{\partial z}) \tag{1a}$$

$$\frac{\partial v}{\partial t} + f\, u = -g\frac{\partial}{\partial y}(\eta - \tilde{\eta}) + l_y + \frac{\partial}{\partial z}(\nu\frac{\partial v}{\partial z}) \tag{1b}$$

The continuity equation is

$$\frac{\partial \eta}{\partial t} + \frac{\partial}{\partial x}(\int_{-h}^{0} u\, dz) + \frac{\partial}{\partial y}(\int_{-h}^{0} v\, dz) = 0 \tag{2}$$

where $u = u(x,y,z,t)$ and $v = v(x,y,z,t)$ are the horizontal velocity components, $\eta = \eta(x,y,t)$ is the sea surface displacement from its undisturbed position and $\tilde{\eta}$ is the equilibrium tide or the astronomic tide-generating potential. ν is the vertical eddy viscosity, (l_x, l_y) is the lateral friction and $f = 2\,\Omega \sin\phi$ is the Coriolis parameter where Ω is the angular velocity of the earth and ϕ the latitude. $z = -h(x,y)$ denotes the sea bottom and g is the acceleration due to gravity.
By integrating eqs (1) through the depth and introducing the depth-averaged velocity components $(\overline{u}, \overline{v})$

$$\overline{u}(x,y,t) = \frac{1}{h}\int_{-h}^{0} u\, dz, \qquad \overline{v}(x,y,t) = \frac{1}{h}\int_{-h}^{0} v\, dz \tag{3}$$

and the depth averaged lateral friction the depth-averaged $(\overline{l}_x, \overline{l}_y)$, equations of motion are obtained

$$\frac{\partial \overline{u}}{\partial t} - f\,\overline{v} = -g\frac{\partial}{\partial x}(\eta - \tilde{\eta}) + \overline{l}_x + \frac{1}{\rho h}(\tau_x^o - \tau_x^h) \tag{4a}$$

$$\frac{\partial \overline{v}}{\partial t} + f\,\overline{u} = -g\frac{\partial}{\partial y}(\eta - \tilde{\eta}) + \overline{l}_y + \frac{1}{\rho h}(\tau_y^o - \tau_y^h) \tag{4b}$$

where (τ_x^o, τ_y^o) are the shear stresses at the sea surface $(z = 0)$ and (τ_x^h, τ_y^h) are the shear stresses at the sea bottom $(z = -h)$ given by

$$\tau_x^o = \rho\,\nu\,\frac{\partial u}{\partial z}|_{z=0}, \qquad \tau_y^o = \rho\,\nu\,\frac{\partial v}{\partial z}|_{z=0}, \tag{5a}$$

$$\tau_x^h = \rho\,\nu\,\frac{\partial u}{\partial z}|_{z=-h}, \qquad \tau_y^h = \rho\,\nu\,\frac{\partial v}{\partial z}|_{z=-h}. \tag{5b}$$

ρ is the mean density of sea water. Invoking (3) the continuity equation (2) can be rewritten as

$$\frac{\partial \eta}{\partial t} + \frac{\partial}{\partial x}(h\overline{u}) + \frac{\partial}{\partial y}(h\overline{v}) = 0 \tag{6}$$

Following Davies (1986b) we will now split the total current in two; a depth mean current $(\overline{u}, \overline{v})$ and a deviation from the mean (u', v'). Hence we write for the components of the total current

$$u = \overline{u} + u', \qquad v = \overline{v} + v'. \tag{7}$$

Inserting (7) into the equations (1) and subtracting the depth averaged equations (4), the current deviations (u', v') are determined by

$$\frac{\partial u'}{\partial t} - f\, v' = \frac{\partial}{\partial z}(\nu \frac{\partial u'}{\partial z}) - \frac{1}{\rho\, h}(\tau_x^o - \tau_x^h) + l_x', \tag{8a}$$

$$\frac{\partial v'}{\partial t} + f\, u' = \frac{\partial}{\partial z}(\nu \frac{\partial v'}{\partial z}) - \frac{1}{\rho\, h}(\tau_y^o - \tau_y^h) + l_y'. \tag{8b}$$

where $l'_{x,y} = l_{x,y} - \overline{l}_{x,y}$. The depth integrated equations (4) for the mean current and the set of equations (8) for the current deviation are coupled together through the boundary conditions (5). It follows from the definition of the depth-averaged velocity (3) and the splitting of the total current (7) that

$$\int_{-h}^{0} u'\, dz = 0, \qquad \int_{-h}^{0} v'\, dz = 0 \tag{9}$$

With a complex notation the momentum equations in x- and y-directions can be written as one complex equation. Defining a complex velocity by

$$w \equiv u + i\, v \tag{10}$$

where i is the imaginary unit, multiplying equation (1b) by i and adding (1a) gives

$$\frac{\partial w}{\partial t} + i\, f\, w = -g(S + \tilde{S}) + \frac{1}{h^2}\frac{\partial}{\partial s}(\nu \frac{\partial w}{\partial s}) + L \tag{11}$$

where S is the complex surface gradient and $\tilde{S}$ is the complex equilibrium-tide are defined respectively by

$$S \equiv \frac{\partial \eta}{\partial x} + i\frac{\partial \eta}{\partial y}, \qquad \tilde{S} \equiv \frac{\partial \tilde{\eta}}{\partial x} + i\frac{\partial \tilde{\eta}}{\partial y}. \tag{12}$$

and $L \equiv l_x + i\, l_y$ is the complex lateral friction. In equation (11) we have also introduced a dimension-less vertical coordinate $s = \frac{z}{h}$, and the vertical domain is then transformed from $z \in [-h, 0]$ to $s \in [-1, 0]$. This coordinate transformation is applicable even though h is a function of x and y.

By defining a complex mean current $(\overline{w} \equiv \overline{u} + i\,\overline{v})$ and a complex deviation current $(w' \equiv u' + i\, v')$ and using the same procedure as above for (8) and (4) we obtain

$$\frac{\partial \overline{w}}{\partial t} + i\, f\, \overline{w} = -g(S + \tilde{S}) + \frac{1}{\rho h}(T_o - T_h) + \overline{L} \tag{13}$$

$$\frac{\partial w'}{\partial t} + i\, f\, w' = \frac{1}{h^2}\frac{\partial}{\partial s}(\nu \frac{\partial w'}{\partial s}) - \frac{1}{\rho h}(T_o - T_h) + L' \tag{14}$$

where we have introduced the complex shear stresses

$$T_o \equiv \tau_x^o + i\,\tau_y^o \qquad T_h \equiv \tau_x^h + i\,\tau_y^h \tag{15}$$

2.2. Boundary conditions

The motion in the bottom boundary layer is mainly dominated by the friction from the sea bottom. In tidal flow the Reynolds number exceeds its critical value when the velocity exceeds 0.2 m/s, and the characteristic minimal value of the tidal depth mean velocity is 1.0−2.0 m/s in the worlds oceans (Marchuk and Kagan, 1984), and the tidal flow is practically always turbulent and then also the bottom boundary layer. The effect of the bottom friction on the flow structure depends on the thickness of the boundary layer compared to the water depth. In shallow water for example the bottom boundary layer may extend to the surface and be determining for the entire flow structure. In this case the boundary layer thickness is equal to the water depth. In deep water the bottom boundary layer will only affect the flow in a very thin layer near the bottom, and the boundary layer thickness is defined such that the velocity at the edge of the boundary layer equals the free stream velocity (Soulsby, 1983). As we shall see later the tidal boundary layer thickness in addition to the water depth and the sea bed roughness also depends upon the geographical position, and the boundary layer may occupy the entire flow region near the critical latitude in shallow and deep water.
Unfortunately, the system of equations of motion is not closed when turbulence is included, so assumptions must be made and various models for the bottom friction may apply. T he complex bottom stress vector defined in (15) is often parameterized by

$$T_h = k\rho\overline{w} \tag{16}$$

where the k is the friction coefficient. By choosing

$$k = c_f|\overline{w}| \tag{17}$$

where c_f is the drag coefficient, (16) corresponds to a quadratic bottom friction law. This form is widely used in depth integrated numerical models of the tidal dynamics. The drag coefficient c_f is in this case usually taken as a constant, either specified or used as a free parameter to tune the model to observations. The measured value of c_f will vary with water depth, sea bed roughness, the phase of the tide and the direction of the depth averaged current due to veering of the total current with depth (Soulsby, 1983). Observations in the Irish Sea (Wolf, 1980) shows that the c_f tends to vary with frequency, and that the quadratic bottom friction lags the observed one with about one hour.
A linear bottom friction law may be modeled by choosing

$$k = c_f u_s \tag{18}$$

where u_s is a typical velocity scale. A similar parameterization applies for the shear stresses due to the deviation current since

$$T_h = \frac{\rho}{h}[\nu \frac{\partial w}{\partial s}]_{s=-1} = \frac{\rho}{h}[\nu \frac{\partial w'}{\partial s}]_{s=-1} \tag{19}$$

when $\overline{w}$ is independent of the depth coordinate. Another form of the bottom boundary condition is obtained by requiring a slip condition i.e.

$$w|_{s=-1} = r\overline{w} \tag{20}$$

where $r = 0$ corresponds to a no-slip condition and $r \to \infty$ to a free-slip condition at the sea bed. This implies that the deviation current must satisfy the condition

$$w'|_{-1} = -a_b\overline{w} \tag{21}$$

where $a_b = 1 - r$ and is used as a calibration parameter to assure consistency of the computation method (section 6.4.2.). The surface stress vector (τ_x^o, τ_y^o) are defined in (5a) and for a purely tidal motion the surface stresses are usually zero i.e..

$$T_o = 0 \quad \Rightarrow \quad \frac{\partial w'}{\partial s}|_{s=0} = 0 \tag{22}$$

except in Arctic regions where the ocean is ice-covered. Since the ice is floating there is no interaction in terms of the hydrostatic pressure between the ice and the water, so the interaction between the ice and the water goes through the interfacial drag. In a thin boundary layer near the surface the motion is then dominated by the friction between the water and the ice, and we can no longer assume zero surface stresses. As for the bottom friction various models for the surface friction may apply and the complex surface stress (15) may be parameterized by

$$T_o = k_{ice}\rho\overline{w} \tag{23}$$

where the k_{ice} is the surface friction coefficient. (23) corresponds to a quadratic friction law when choosing

$$k_{ice} = c_{fi}|\overline{w}| \tag{24}$$

where c_{fi} is the drag coefficient characteristic for the water-ice interface. A linear bottom friction law may be modeled by choosing

$$k_{ice} = c_{fi}u_s \tag{25}$$

For ice drifting with a velocity $\vec{v}_{ice}$, the boundary condition at the surface must be

$$\vec{v} = a_s\vec{v}_{ice} + (1 - a_s)\vec{\overline{v}} \quad \text{at } s = 0 \tag{26}$$

where $a_s = 1$ corresponds to a no-slip condition between the ice and the water i.e. $\vec{v} = \vec{v}_{ice}$. $\vec{v}$ is the current vector with components u and v in the x- and y- directions respectively. By introducing a complex ice velocity ($w_{ice} \equiv u_{ice} + i\,v_{ice}$) the boundary condition at the sea surface can be written

$$w'|_{s=0} = -a_s(\overline{w} - w_{ice}) \tag{27}$$

which leads to $w'|_{s=0} = -a_s\overline{w}$ for ice at rest $\vec{v}_{ice} = 0$.

2.3. Turbulent closure approximations

Various turbulent closure approximations have been devised for the tidal boundary layer. The Boussinesq's eddy viscosity concept, which assumes that the Reynolds stresses are proportional to the mean velocity gradient, has been widely used.
Prandtl's mixing length hypothesis from 1925 relates the eddy viscosity to the velocity gradient and the mixing length l

$$\nu = l^2|[(\frac{\partial u}{\partial z})^2 + (\frac{\partial v}{\partial z})^2]^{\frac{1}{2}}| = l^2|\frac{\partial w}{\partial z}| \tag{28}$$

where w is the complex current defined in (10). Fang and Ichiye (1982) applied the mixing length theory for numerical calculations of the vertical structure of tidal currents with a finite difference scheme, and obtained a fair agreement with the observations of Bowden et al. (1959).
Another approach is to assume that the eddy viscosity has the simple form

$$\nu(x,y,z,t) = \nu_o(x,y,t) \cdot \phi(z) \tag{29}$$

where the function $\phi(z)$ describes a fixed form of the eddy viscosity in the vertical. The horizontal and time variation of the eddy viscosity is described by the function $\nu_o(x,y,t)$. This form of the viscosity has the major advantage of permitting a spectral solution of the equations, as we shall see later. ν given by (29) is a function of the flow field when ν_o is proportional with the depth mean current, and this way of presenting the eddy viscosity is used in various three-dimensional tidal models (Davies and Furnes 1980, Davies 1986). A number of different vertical eddy viscosity profiles for tidal currents have been given in the literature. The simplest, for which there exists an analytical solution (presented in sec.6.2.), is to assume a constant eddy viscosity through the vertical (figure 1a). A solution for the tidal current with a constant eddy viscosity in space and time was given by Sverdrup (1926) and discussed further by Prandle (1982). For tidal waves on the North Siberian Shelf Sverdrup (1926) noted that the eddy viscosity is far from being constant because of the density stratification.
An eddy viscosity which increases linear with height above sea bed (figure 1c), for which there also exists an analytical solution (Soulsby, 1983), reproduces the near bed velocity profile much more accurately than the constant (Soulsby, 1983). Soulsby used an eddy viscosity of the form

$$\nu(z) = \kappa u_{*,m} z \tag{30}$$

where $u_{*,m}$ is the maximum frictional velocity over a tidal cycle and $\kappa = 0.4$ von Karmans constant.
Based on observations in the Irish Sea Bowden et al. (1959) suggested a simple theoretical eddy viscosity model of the form in figure 1b, which have a friction layer near the bottom with thickness (d_o) of the order one-tenth of the water depth, where the eddy viscosity increases linear with height above sea bed. In the remainder of the water column Bowden et al. kept the eddy viscosity independent of depth. The sea bed value of the eddy viscosity may be given by

$$\nu(-h) = \kappa u_* z_o \tag{31}$$

where u_* is the frictional velocity and z_o is the roughness height. This leads to eddy viscosity values at the sea bed ranging from approximately 2.0 cm^2/s to 0.02 cm^2/s (Davies, 1985). These values are based on observational evidence summarized in Soulsby (1983) Above d_o the eddy viscosity was assumed constant at a value given by

$$\nu_o = 0.0025\, h\, \overline{u} \tag{32}$$

for shallow water, and in deeper water where the water depth is thicker than the bottom boundary layer, by

$$\nu_o = k_o \frac{u^2}{\omega_o} \tag{33}$$

(Davies and Furnes 1980) with a constant $k_o = 2 \cdot 10^{-5}$ and $\omega_o = 10^{-4}\text{s}^{-1}$ a typical frequency. The equations (32) and (33) give ν_o values between 500 cm^2/s to 2000 cm^2/s (Davies, 1985)

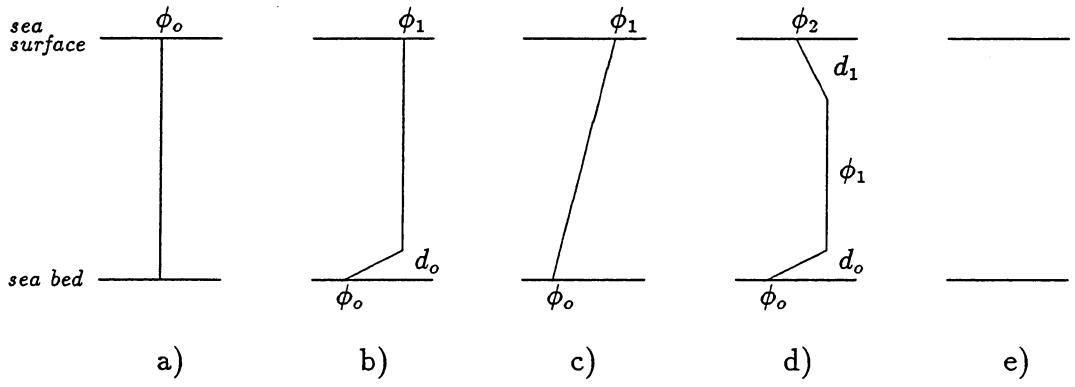

Figure 1: *Various eddy viscosity depth distributions $\phi(s)$, values of the parameters d_o, d_1, ϕ_o, ϕ_1 and ϕ_2 are summarized in the text.*

for typical tidal current velocities in the North Sea 40-100 cm/s with a mean depth of 50 m. Observations in the Irish Sea (Wolf, 1980 and Bowden et al. 1959) suggest that the eddy viscosity increase in a parabolic way, reaching a maximum below mid-depth and reducing to a small value at sea surface. (figure 1e). These observations also show that the eddy viscosity varies over the tidal cycle, tending to reach maximum values when the current was maximum, and to be larger during the flood than during the ebb. Marchuk and Kagan (1984) presents also an eddy viscosity coefficient in the tidal boundary layer with similar characteristics. The eddy viscosity typically increases almost linearly in the lower layer, then its growth slows down and in the rest of the boundary layer it decreases monotonically with height above sea bed. A simple vertical variation of the viscosity having these characteristics (Davies, 1985) is shown in figure 1e. The values of ϕ_2 and d_1 are not decisive for the calculations of tidal profile calculations under a free ocean surface, and even increasing d_1 from 0.1 h to 0.25 h had little effect upon the computed tidal profiles (Davies, 1990).
By analogy with the sea bed friction layer, there should exist a surface friction layer when the ocean is ice covered. The eddy viscosity should then also diminish close to the surface to a value $\nu = \phi_2 \nu_o$ over a distance d_1 in figure 1d. The surface value may be given by a similar relation as (31) with a frictional velocity and a roughness length related to an ice surface. We shall see later that ϕ_2 and d_1 have a larger effect on the tidal current profiles calculations under a ice covered surface than the tidal current profile calculations under a free ocean surface.
In $k, \varepsilon-$models the eddy viscosity is expressed by the kinetic energy of the turbulent motion k and the dissipation ε

$$\nu = const. \cdot \frac{k^2}{\varepsilon} \tag{34}$$

and the complete formulation of this model and the equations for k and ε are given in Rodi (1980). The eddy viscosity are given by $\nu = const.l\sqrt{k}$ when the energy dissipation are proportional to $k^{3/2}/l$ where l is the mixing length. Davies and Jones (1990) has applied a three-dimensional turbulence energy model i.e. a $k, \varepsilon-$model to determine the tidal flow on the Northwest European Shelf. Resulting eddy viscosity profiles from this model support a vertical distribution of the form in figure 1e i.e. a rapid increase in the near bed region, with a maximum below mid-water depth. A detailed examination of the computed profiles at

different points showed that this type of profile was common in the shelf (Davies and Jones, 1990).

3. Numerical methods

3.1. Computation procedure

The method of extracting current profiles from two dimensional vertically integrated models (Davies, 1986) may be described in three steps.
Firstly the continuity equation (6) and the depth-averaged equations (4) (or (13)) together with the shear stresses (5) expressed with the mean current as in (16) and (23) defines a set of two-dimensional depth integrated equations. Most of the tide and storm-surge models existing today are based on these depth integrated equations approximated by a set of finite difference equations. The forward centered scheme developed by Anita Sielecki (1968) in a staggered C-grid (Mesinger and Arakawa, 1976) is widely used for such numerical models. Further details for these models will not be discussed here. From this the computed time series of depth mean current, sea bed and surface stress (at each grid point where a current profile is required) are saved as the two dimensional model is integrated forward in time. In the case of a tide model only the amplitudes and phases of the depth mean current for the different tidal constituents are needed, because the motion is periodic in time. These two-dimensional models do not give any information about the vertical variation of the current from sea bed to sea surface, so in the next step the current deviations (u', v') are determined i.e. the equations (8) (or (14)) with boundary conditions at sea bed (21) and at sea surface (22) or (27) with a turbulent closure approximation must be solved. Now the sea bed and surface shear stresses are known from the depth integrated model in the grid point where a current profile will be computed. The vertical distribution of the current may be computed for different turbulence closure approximations and the numerical methods are described subsequently. In the last step the total current (7) may be determined, where we must have (3) fulfilled to assure consistency.
In addition to this we have that the method is consistent when the shear stresses computed from the current profiles directly from the definition (5) equals the shear stresses from the depth integrated model parametrizied by a linear or quadratic friction law. Or if the total current is computed in every grid point in the depth integrated model, a new estimate of the stresses can be determined from (5) which can be given as input in a new run of the depth integrated model, and the procedure may be continued until convergence hopefully is obtained.

3.2. The Galerkin method

We will now use the Galerkin method to find a solution of equation (14) with a zero lateral friction i.e. $L' = 0$. The solution is expanded in a set of trial functions, i.e. known functions in the vertical; w_N. The choice of the trial functions w_N depends upon the boundary conditions. It is not necessary that the trial functions satisfy all the boundary conditions. In variational methods the trial functions need not satisfy the natural boundary conditions, since the variational principle forces them to be satisfied, but they must satisfy the essential boundary conditions. The same approach can be used in methods of weighted residuals (Finlayson 1972), in which the Galerkin method is classified.

In the case where the surface is ice covered, the slip condition at the bottom (21) and at the surface (27) are the essential boundary conditions. In order to satisfy the essential boundary conditions a trial solution is taken to be of the form

$$w' = w_N = w_o(s,t) + \sum_{r=1}^{N} c_r(t)\, w_r(s) \tag{35}$$

where $w' = w_o$ at the boundaries i.e.

$$w_o = \begin{cases} -a_s(\overline{w} - w_{ice}), & \text{for } s = 0 \\ -a_b\overline{w}, & \text{for } s = -1 \end{cases} \tag{36}$$

and w_r are specified to satisfy the homogeneous boundary conditions i.e.

$$w_r = 0 \quad \text{for } s = 0 \quad \text{and} \quad s = -1 \tag{37}$$

for all $r = 1, 2, \ldots, N$.
For a purely tidal motion we have a free-slip condition at the surface (22) and a no-slip condition at the sea bed (21). A trial solution is again taken in the form as in (35), but now we have

$$w_o = -a_b\overline{w} \quad \text{for} \quad s = -1 \tag{38}$$

and w_r are specified to satisfy the boundary conditions

$$\begin{aligned} \frac{\partial w_r}{\partial s} &= 0 \quad \text{for} \quad s = 0 \\ w_r &= 0 \quad \text{for} \quad s = -1 \end{aligned} \tag{39}$$

for all $r = 1, 2, \ldots, N$. The expansion coefficients c_r are functions of time only.
The choice of $w_o(s,t)$ will affect the coefficients c_r and should preferably be chosen to assure a fast convergence of the series expansion (35). In the example treated below w_o is chosen to be a function of the depth mean current.
When applying the Galerkin method we transform (14) to the dimension-less vertical coordinate s and substitute the expansion (35) for w'. This leads to

$$\begin{aligned} \sum_{r=1}^{N}\left(\frac{\partial c_r}{\partial t} + if\, c_r\right)w_r - \sum_{r=1}^{N}\frac{c_r}{h^2}\frac{\partial}{\partial s}\nu\frac{\partial w_r}{\partial s} + \frac{1}{\rho h}(T_o - T_h) \\ = -\frac{\partial w_o}{\partial t} - if\, w_o + \frac{1}{h^2}\frac{\partial}{\partial s}\nu\frac{\partial w_o}{\partial s} \end{aligned} \tag{40}$$

Equation (40) is then multiplied by the weighted functions, which in the Galerkin method is the trial functions i.e. w_k, $k = 1, 2, \ldots N$, and then integrated over the interval $[-1, 0]$. The terms involving the eddy viscosity can be integrated by parts and after applying the boundary conditions on w_r we obtain

$$\begin{aligned} \left(\frac{\partial c_r}{\partial t} + if\, c_r\right)\int_{-1}^{0} w_r w_k ds + \frac{c_r}{h^2}\int_{-1}^{0}\nu\frac{\partial w_r}{\partial s}\frac{\partial w_k}{\partial s}ds + \frac{1}{\rho h}(T_o - T_h)\int_{-1}^{0} w_k ds \\ = -\int_{-1}^{0}\left[\frac{\partial w_o}{\partial t} + if\, w_o\right]w_k ds - \frac{1}{h^2}\int_{-1}^{0}\nu\frac{\partial w_o}{\partial s}\frac{\partial w_k}{\partial s}ds \end{aligned} \tag{41}$$

for $k = 1, 2, \ldots, N$ and where summation over r is understood. This set of coupled equations (41) determine the expansion coefficients c_r.
Choosing for example trigonometric functions, Chebyshevs polinominals or other known expantionfunctions together with a vertical distribution of ν, the integrals in (41) can be evaluated.
In the case where we have approximated the eddy viscosity by the Prandlts mixing length by equation (28) we have

$$\nu = l \sum_{r=1}^{N} \frac{c_r}{h} \left| \frac{\partial w_r}{\partial s} \right|$$

when the trial solution of the form (35) is inserted. The integral in the second term in eq (41) may then be computed when the expansion functions w_r are chosen. And then the coefficients c_r are determined by solving the non linear set of equations

$$\begin{aligned} \left(\frac{\partial c_r}{\partial t} + if\, c_r\right) \int_{-1}^{0} w_r w_k ds + l \frac{c_r^2}{h^3} \int_{-1}^{0} \left(\frac{\partial w_r}{\partial s}\right)^2 \frac{\partial w_k}{\partial s} ds + \frac{1}{\rho h}(T_o - T_h) \int_{-1}^{0} w_k ds \\ = -\int_{-1}^{0} \left[\frac{\partial w_o}{\partial t} + if\, w_o\right] w_k ds - l \frac{c_r}{h^3} \int_{-1}^{0} \left|\frac{\partial w_r}{\partial s}\right| \frac{\partial w_o}{\partial s} \frac{\partial w_k}{\partial s} ds \end{aligned} \tag{42}$$

Another way of choosing the expansion functions is by imposing the eddy viscosity (ν) of the form (29) and choosing the trial functions as an orthogonal set of eigenfunctions defined by

$$\frac{\partial}{\partial s}\left(\phi \frac{\partial w_r}{\partial s}\right) = -\varepsilon_r\, w_r \quad \text{for} \quad r = 1, 2, \ldots, N. \tag{43}$$

where ε_r are the corresponding eigenvalues (Davies,1983a). With this choice of trial functions the equations (41) are uncoupled. $\phi(s)$ is the vertical variation of the eddy viscosity. This way of representing the vertical eddy viscosity eliminates for example the use of Prandtl's mixing length theory where the eddy viscosity is a function of the motion and not only of a function of the position. (43) is the well known Sturm-Liouville problem, and applying the Galerkin method i.e. multiplying (43) by w_k and integrating from -1 to 0 gives

$$\left[\phi \frac{\partial w_r}{\partial s} w_k\right]_{-1}^{0} - \int_{-1}^{0} \phi \frac{\partial w_r}{\partial s} \frac{\partial w_k}{\partial s} ds = -e_r \int_{-1}^{0} w_r w_k ds \tag{44}$$

The eigenfunctions are orthogonal, that means that they satisfy the condition

$$\int_{-1}^{0} w_r w_k ds = 0 \quad (r \neq k) \tag{45}$$

provided that the boundary conditions satisfy the relation (Butkov,1968)

$$\phi \frac{\partial w_r}{\partial s} w_k \Big|_{0} - \phi \frac{\partial w_r}{\partial s} w_k \Big|_{-1} = 0 \tag{46}$$

Inserting (44) into the equation (41) with orthogonal eigenfunctions (45) gives

$$\frac{\partial c_r}{\partial t} + (i f + \frac{\nu_o \varepsilon_r}{h^2}) c_r = F_r E_r(t) \tag{47}$$

for r=1,2, ... ,N, and where

$$E_r(t) = -\frac{1}{\rho h}(T_o - T_h) \int_{-1}^{0} w_r ds - \int_{-1}^{0} (\frac{\partial w_o}{\partial t} + if\, w_o) w_r ds - \frac{\nu_o}{h^2} \int_{-1}^{0} \phi \frac{\partial w_o}{\partial s} \frac{\partial w_r}{\partial s} ds \tag{48}$$

and

$$F_r = \frac{1}{\int_{-1}^{0} {w_r}^2 ds} \tag{49}$$

This set of N uncoupled equations determine the expansion coefficients c_r This may be done by using Laplace transforms, and are given by the convolution integral (Butkov,1968), (Davies,1986)

$$c_r(t) = F_r \int_0^t E_r(t-\tau) \mathrm{e}^{(i f - \nu_o \varepsilon_r)\tau}\, d\tau \tag{50}$$

and then the expansion (35) may be rewritten in the form

$$w' = w_o(s,t) + \sum_{r=1}^{N} C_r(t)\, F_r\, w_r(s) \tag{51}$$

where $c_r(t) = C_r(t)\, F_r$.

3.2.1. Ice covered ocean surface

Specially for an ice covered sea surface with ice at rest i.e. $w_{ice} = 0$ we have $w_o(0,t) = -a_s \overline{w}$ and $w_o(-1,t) = -a_b \overline{w}$. Choosing $w_o(s,t)$ to be a linear function of s we obtain

$$w_o(s,t) = -(a_s - a_b)\overline{w}\, s - a_s \overline{w} \tag{52}$$

and $E_r(t)$ in (48) is

$$E_r(t) = -\frac{1}{\rho h}(T_o - T_h) \int_{-1}^{0} w_r ds + (\frac{\partial \overline{w}}{\partial t} + if\, \overline{w}) \int_{-1}^{0} [(a_s - a_b)s + a_s] w_r ds + \frac{\nu_o}{h} \overline{w} (a_s - a_b) \int_{-1}^{0} \phi(s) \frac{\partial w_r}{\partial s} ds \tag{53}$$

depending upon the time variation of the boundary shear stresses and the depth mean current. The total current can now be written

$$w = \overline{w} + w' = -[(a_s - a_b)s + a_s - 1]\overline{w} + \sum_{r=1}^{N} C_r(t)\, F_r\, w_r(s) \tag{54}$$

In the case where we have a no-slip boundary condition at sea surface and sea bed i.e. $a_s = a_b = 1$ in eq.(21) and (27), $E_r(t)$ in (53) is reduced to

$$E_r(t) = [-\frac{1}{\rho h}(T_o - T_h) + (\frac{\partial \overline{w}}{\partial t} + if\,\overline{w})] \int_{-1}^{0} w_r ds \tag{55}$$

Since we now have by (52) that $w_o = -\overline{w}$ the total current (54) is now given by

$$w = \sum_{r=1}^{N} C_r(t)\, F_r\, w_r(s) \tag{56}$$

Invoking equation (13) when neglecting the direct influence of the tide-generating potential ($\tilde{S}$) and the lateral friction ($\overline{L}$), $E_r(t)$ may be written

$$E_r(t) = -g\, S \int_{-1}^{0} w_r ds \tag{57}$$

depending upon the surface gradient.

3.2.2. Free ocean surface

Specially for a free ocean surface we have $w_o(-1,t) = -a_b\overline{w}$ and we choose

$$w_o(s,t) = -a_b\overline{w} \tag{58}$$

and $E_r(t)$ in (48) are given by

$$E(t) = [-\frac{1}{\rho h}(T_o - T_h) + a_b(\frac{\partial \overline{w}}{\partial t} + if\,\overline{w})] \int_{-1}^{0} w_r ds \tag{59}$$

The total current can now be written

$$w = \overline{w} + w' = (1 - a_b)\overline{w} + \sum_{r=1}^{N} C_r(t)\, F_r\, w_r(s) \tag{60}$$

In the case where we have a no-slip boundary condition at sea bed (21) with $a_b = 1$, $E_r(t)$ is given by (55) and the total current by (56).

3.3. Numerical solution of the eigenvalue problem

A numerical solution of the eigenvalue problem is found by approximating eq.(43) by a finite difference equation where we have used centered differences with constant depth discretization $\triangle s$. We write $s \approx s_j = -(j-1)\triangle s$ where $s_1 = 0$ and $s_m = -1$ and we have

$$-\phi_{j-\frac{1}{2}} w_{j-1} + (\phi_{j+\frac{1}{2}} + \phi_{j-\frac{1}{2}}) w_j - \phi_{j+\frac{1}{2}} w_{j+1} = \varepsilon \triangle s^2 w_j \tag{61}$$

for $j = 2, 3, \ldots, m-1$ and where $\phi_{j+\frac{1}{2}} = \phi(s_j + \frac{1}{2}\triangle s)$ and $w_j = w(s_j)$. The no-slip bed boundary condition gives

$$w_m = 0 \tag{62}$$

No-slip surface bc:

	Analytical solution	Numerical solution $\triangle s = \frac{1}{25}$	$\triangle s = \frac{1}{50}$	$\triangle s = \frac{1}{100}$	$\triangle s = \frac{1}{200}$	$\triangle s = \frac{1}{500}$
ε_1	9.870	9.857	9.866	9.869	9.869	9.870
ε_2	39.478	39.271	39.426	39.465	39.475	39.478
ε_3	88.826	87.779	88.564	88.761	88.810	88.824
ε_4	157.914	154.617	157.084	157.706	157.862	157.905
ε_5	246.740	238.729	244.717	246.233	246.613	246.720
ε_6	355.306	338.789	351.118	354.255	355.043	355.264
ε_7	483.611	453.220	475.865	481.665	483.124	483.533
ε_8	631.655	580.216	618.467	628.337	630.824	631.522
ε_9	799.438	717.776	778.360	794.126	798.107	799.225

Free-slip surface bc:

	Analytical solution	Numerical solution $\triangle s = \frac{1}{25}$	$\triangle s = \frac{1}{50}$	$\triangle s = \frac{1}{100}$	$\triangle s = \frac{1}{200}$	$\triangle s = \frac{1}{500}$
ε_1	2.467	2.568	2.517	2.492	2.480	2.472
ε_2	22.207	23.051	22.640	22.426	22.317	22.251
ε_3	61.685	63.680	62.806	62.274	61.987	61.807
ε_4	120.903	123.789	122.851	121.997	121.479	121.140
ε_5	199.859	202.390	202.535	201.534	200.779	200.246
ε_6	298.556	298.192	301.537	300.806	299.866	299.124
ε_7	416.991	409.624	419.458	419.716	418.718	417.768
ε_8	555.165	534.854	555.823	558.143	557.303	556.174
ε_9	713.079	671.827	710.083	715.951	715.588	714.337

Table 1: *The first nine Eigenvalues.*

The numerical representation of the surface boundary conditions is

$$w_1 = \begin{cases} 0 & \text{for a no-slip surface condition} \\ w_2 & \text{for 1.order free-slip s.c.; } O(\triangle s) \\ \frac{1}{3}(4w_2 - w_3) & \text{for 2.order free-slip s.c.; } O(\triangle s^2) \end{cases} \tag{63}$$

The eigenvectors and -values of (61) are found by using an Eispack subroutine which finds the eigenvectors and -values of a symmetric tridiagonal matrix by the implicit Ql method (Wilkinson and Reinsch,1971). When the total water depth region are represented by m points in the vertical then the depth discretization is $\triangle s = 1/(m-1)$ and the total number of numerical eigenvalues are $n = m - 2$. The eigenvalues ε_r are sorted such that $\varepsilon_1 < \varepsilon_2 < \ldots < \varepsilon_r < \ldots < \varepsilon_n$ and w_r are the corresponding eigenvectors.

Davies (1985) has used another numerical approach where the eigenvalue problem is solved using the Galerkin method with piecewise B-spline polynominals as expansion functions. By this method it is possible to have finer resolution in the near bed boundary layer.

As we shall see later the tidal current boundary layer in the Barents sea may occupy the entire sea depth and because of the ice covered surfaces far north in the Barents sea, there also exist a surface boundary layer. Therefore a fine resolution may be needed in the whole sea depth region, and the depth discretization is therefore kept constant.

The eigenvalues are computed for a constant eddy viscosity (i.e.when $\phi(z) = 1$) are shown in figure 2 for depth discretization $\triangle s = \frac{1}{25}, \frac{1}{50}, \frac{1}{100}, \frac{1}{200}$ and $\frac{1}{500}$ for the free-slip (fig.2a) and no-slip (fig.2b) boundary conditions respectively. For comparison the eigenvalues of the analytical solution is shown. The analytical solution of the eigenvalue problem for a constant

eddy viscosity is

$$F_r\, w_r(s) = \begin{cases} \frac{2}{r\pi}(1-\cos(r\pi))sin(-r\pi s) & \text{for a no-slip sc.} \\ \frac{2}{\alpha_r}\sin(\alpha_r)cos(\alpha_r s) & \text{for a free-slip s.c.} \end{cases} \tag{64}$$

for $r = 1, 2, \ldots$, with corresponding eigenvalues $e_r = (r\pi)^2$ and $e_r = (\alpha_r)^2 = ((r-\frac{1}{2})\pi)^2$ for the no-slip (37) and free-slip surface boundary conditions (39) respectively. The first nine eigenvalues are given in table 1.
There are found no significant difference using a first or second order approximation of the free-slip surface boundary condition (63) and the 1.order approximation therefore are used.
The relative error i.e. the deviation of the numerical solutions from the analytical, in % is defined by

$$\triangle\varepsilon_r = \frac{|\varepsilon_{r,ana} - \varepsilon_{r,num}|}{\varepsilon_{r,ana}} \cdot 100\,\% \tag{65}$$

where the subscripts *ana* and *num* refer to the analytical and numerical solution respectively. From figure 3 we see that $\triangle\varepsilon_r < 2\%$ with $\triangle s = \frac{1}{100}$ for the 20 first eigenvalues for both the free-slip (fig.3a) and no-slip (fig.3b) boundary conditions. If a deviation of 2% is tolerable, the Galerkin series (35) may be truncated after $N \sim 15 - 20$ terms for $\triangle s = \frac{1}{100}$, after $N \sim 30 - 40$ terms for $\triangle s = \frac{1}{200}$ and after $N \sim 80$ terms for $\triangle s = \frac{1}{500}$. So, in order to choose depth discretization in the numerical solution, one must know for how many terms N the Galerkin series may be truncated to obtain a tolerable deviation. This will be analyzed in examples later.

The nine first eigenfunctions for $\triangle s = \frac{1}{100}$ are shown in figure 4 and 5 for a free- and no-slip surface boundary conditions respectively.

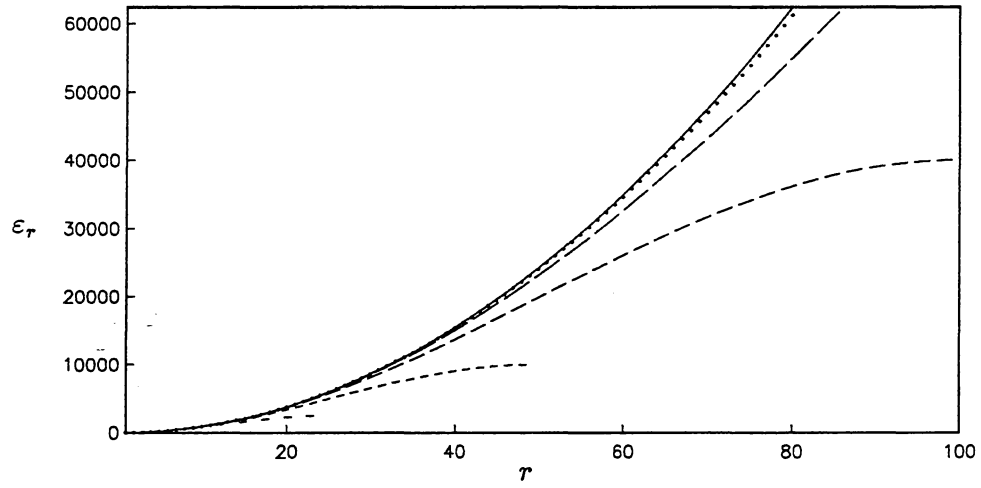

a)

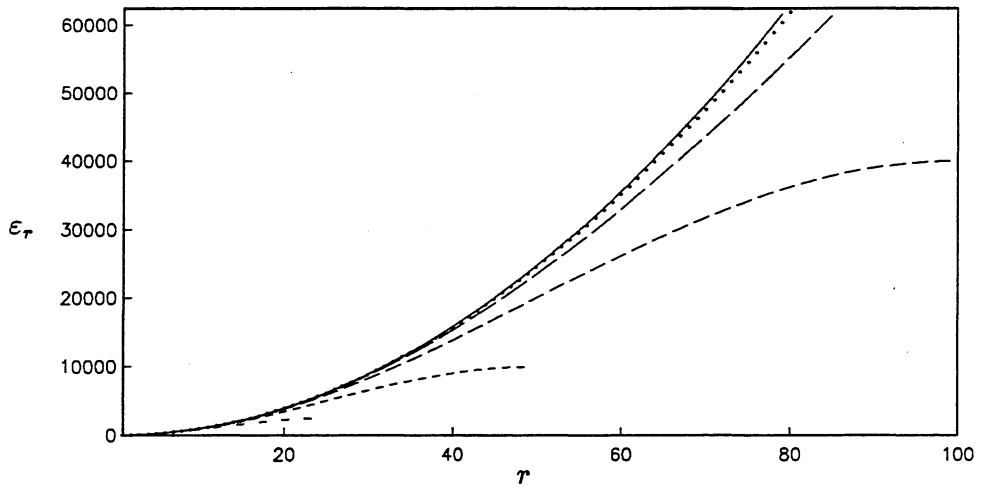

b)

Figure 2: *The r'th eigenvalue ε_r as a function of r for (a) the free-slip and (b) the no-slip surface boundary conditions. Analytical solution (———). Numerical solution for $\triangle s = \frac{1}{25}$ (- - - -), $\triangle s = \frac{1}{50}$ (– – –), $\triangle s = \frac{1}{100}$ (— —), $\triangle s = \frac{1}{200}$ (—· —·) and $\triangle s = \frac{1}{500}$ (.....).*

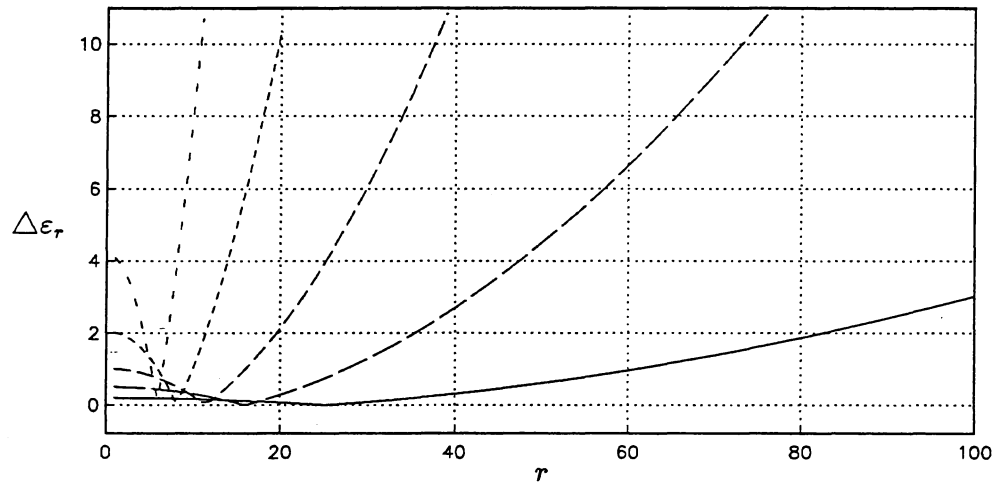

a)

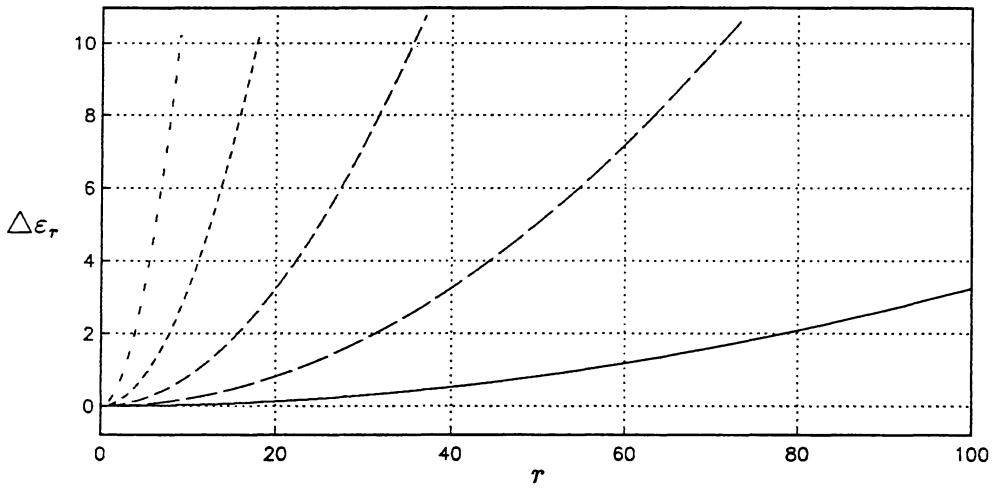

b)

Figure 3: *The r'th relative error $\triangle\varepsilon_r$ in % as a function of r for (a) the free-slip and (b) the no-slip surface boundary conditions with $\triangle s = \frac{1}{25}$ (- - -), $\triangle s = \frac{1}{50}$(– – – – – –), $\triangle s = \frac{1}{100}$ (— —), $\triangle s = \frac{1}{200}$ (— —) and $\triangle s = \frac{1}{500}$ (———).*

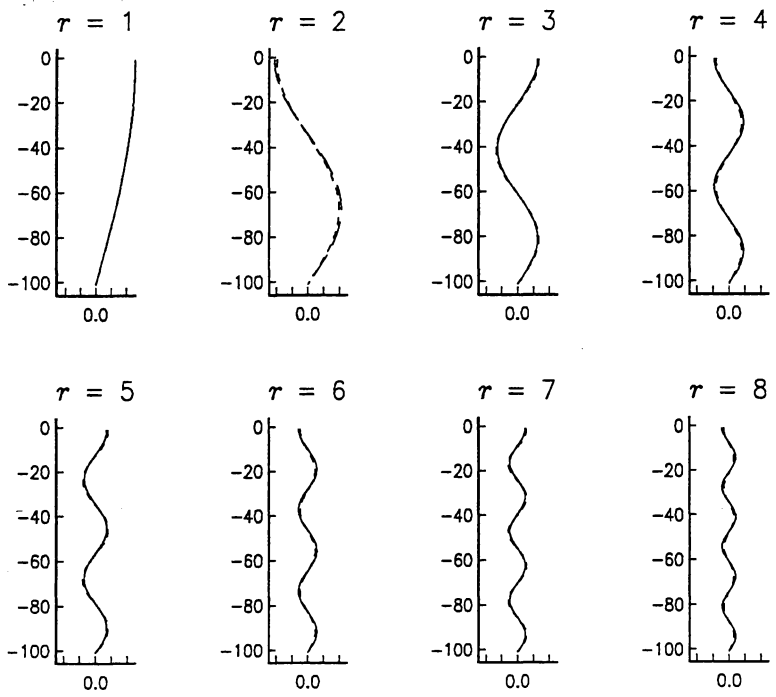

Figure 4: *The 8 first eigenfunctions for the free-slip surface boundary conditions. - numerical solution with* $\triangle s = \frac{1}{100}$ *(dotted line). - analytical solution (full line).*

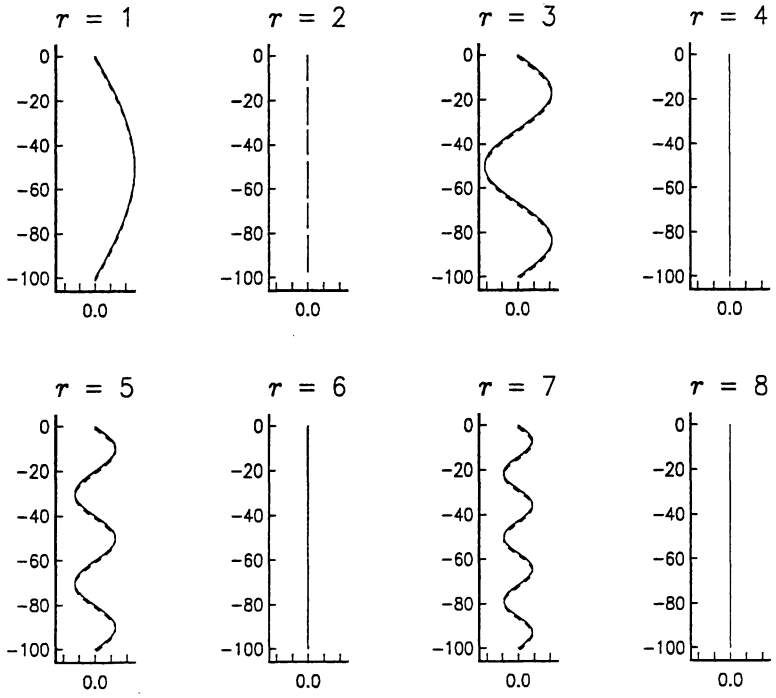

Figure 5: *The 8 first eigenfunctions for the no-slip surface boundary conditions. - numerical solution with* $\triangle s = \frac{1}{100}$ *(dotted line). - analytical solution (full line).*

4. Tidal flow

4.1. Equations of motion in rotary form

The tidal motion is almost periodic and therefore the time-dependency in the equation of motion can be removed by first expressing the velocity in rotary components (Prandle 1982, Soulsby 1983, Davies 1985) and then we will introduce the tidal current ellipse.
Considering one tidal constituent, the corresponding velocity components can be written

$$u(x,y,z,t) = u_0 \cos(\omega t - \delta_u), \qquad v(x,y,z,t) = v_0 \cos(\omega t - \delta_v) \tag{66}$$

where $u_0 = u_0(x,y,z), v_0 = v_0(x,y,z)$ represent current amplitudes and $\delta_u = \delta_u(x,y,z)$, $\delta_v = \delta_v(x,y,z)$ current phases. ω is the frequency of the tidal constituent, and t is the time variable. By substitution for u and v from (66) we obtain for the complex velocity defined in (10)

$$w = R_+ \, e^{i\omega t} + R_- \, e^{-i\omega t} \tag{67}$$

where

$$R_\pm = \frac{1}{2}(u_0 \cos\delta_u \pm v_0 \sin\delta_v) + \frac{i}{2}(v_0 \cos\delta_v \mp u_0 \sin\delta_u) \tag{68}$$

$R_+ \, e^{i\omega t}$ represents a velocity vector with constant value which is rotating in the complex u,v plane in counter clockwise or cyclonic direction in time with a frequency ω. In a similar way $R_- \, e^{-i\omega t}$ is a velocity vector rotating in clockwise or anticyclonic direction when viewed from above. By adding these two rotary motions via (67) the total current vector will describe the ellipse shown in figure 6.
The major semi axis (A) of the ellipse corresponds to the maximum current velocity which occur when $R_+ e^{i\omega t}$ and $R_- e^{-i\omega t}$ has the same direction i.e.

$$A = |R_+| + |R_-| \tag{69a}$$

The minor semi axis (B) corresponds to the minimum velocity which occurs when $R_+ e^{i\omega t}$ and $R_- e^{-i\omega t}$ has opposite directions. Hence the minor semi-axis is

$$B = |R_+| - |R_-| \tag{69b}$$

The angle between the direction of the major axis and the x-axis is given by

$$\alpha = \frac{1}{2}(g_1 + g_2) \tag{69c}$$

where $g_1 = \arctan(\frac{Im(R_+)}{Re(R_+)})$ and $g_2 = \arctan(\frac{Im(R_-)}{Re(R_-)})$ and $Im(R_\pm)$ is the imaginary part of $R_\pm$ and $Re(R_\pm)$ the real part. When referring to the azimuth orientation of the tidal current ellipse, it is meant the angle between the major semi-axis and North (0.degree = North and 90.degrees = East).
The direction of rotation is determined by

$$\begin{aligned} \text{cyclonic rotation: } & |R_+| > |R_-| \text{ i.e. } B > 0 \\ \text{anticyclonic rotation: } & |R_+| < |R_-| \text{ i.e. } B < 0 \\ \text{no rotation: } & |R_+| = |R_-| \text{ i.e. } B = 0 \end{aligned} \tag{69d}$$

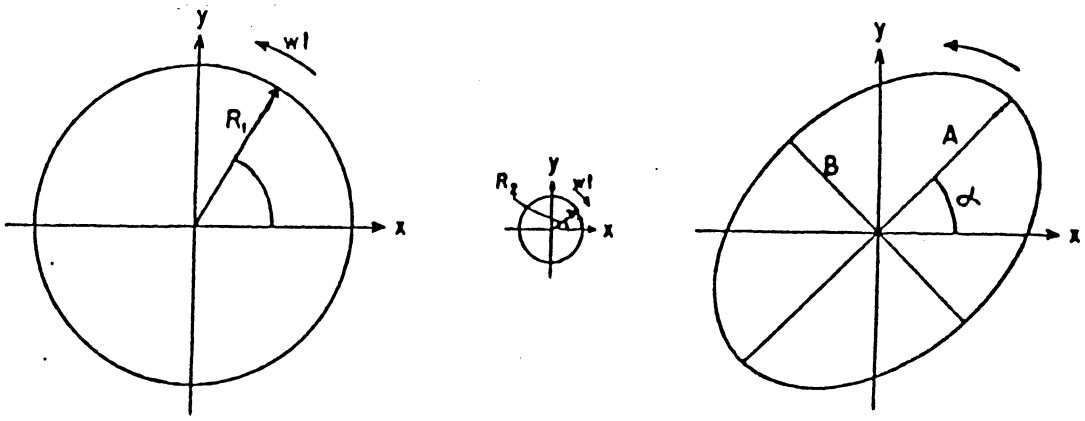

a) b) c)

Figure 6: *The tidal current ellipse (Prandle, 1982) (a) cyclonic rotation (b) anticyclonic rotation (c) the total current.*

The eccentricity ϵ is here defined as the ratio of the minor and major semi axis i.e.

$$\epsilon = \frac{B}{A} \tag{69e}$$

and where $\epsilon > 0$ indicates cyclonic rotation and $\epsilon < 0$ indicates anticyclonic rotation. In the case of rectilinear motion $\epsilon = 0$ which means that $|A| \gg |B|$. For circular motion $\epsilon = 1, -1$ where $|A| \sim |B|$.
When the total velocity is expressed in rotary components, the equation of motion (11) can also be split into rotary components leading to an equation for each component R_+ and R_-. When assuming that the eddy viscosity is constant in time and substituting (67) in (11) we obtain

$$i(f+\omega)R_+ = \frac{1}{h^2}\frac{\partial}{\partial s}(\nu\frac{\partial R_+}{\partial s}) - g(S_+ + \tilde{S}_+) + \nu_H \bigtriangledown_H^2 R_+ \tag{70a}$$

$$i(f-\omega)R_- = \frac{1}{h^2}\frac{\partial}{\partial s}(\nu\frac{\partial R_-}{\partial s}) - g(S_- + \tilde{S}_-) + \nu_H \bigtriangledown_H^2 R_- \tag{70b}$$

where we for the considered tidal constituent can write the surface elevation in the form

$$\eta(x,y,s,t) = \eta_0 \cos(\omega t - \delta_\eta) \tag{71}$$

and S defined in (12) can be written

$$S = S_+ e^{i\omega t} + S_- e^{-i\omega t} \tag{72}$$

and $S_\pm$ are given by

$$S_\pm = \frac{1}{2}([\eta_0 \cos\delta_\eta]_x \pm [\eta_0 \sin\delta_\eta]_y) + \frac{i}{2}([\eta_0 \cos\delta_\eta]_y \mp [\eta_0 \sin\delta_\eta]_x) \tag{73}$$

where $[\ ]_x$ is $\frac{\partial}{\partial x}$ and $[\ ]_y$ is $\frac{\partial}{\partial y}$. And similarly for the tidal potential $\tilde{\eta}$.

The inviscid ($\nu = \nu_H = 0$) solution of (70) is

$$R_{\pm,inviscid} = -\frac{g\, S_{\pm,inviscid}}{i(f \pm \omega)} \tag{74}$$

where the free stream value $R_{\pm,inviscid}$ is independent of depth, but varies with the Coriolis parameter. Since the Coriolis parameter changes magnitude with geographical latitude, ϕ i.e. $f(\phi) = 2\Omega \sin\pi$, $R_{\pm,inviscid}$ is a function of ϕ. When $f \to \omega$ i.e. near the critical latitude, $R_{\pm,inviscid}$ goes to infinity.

As for the total current (w) we may also split the deviation current (w') in rotary components

$$w' = R'_+\, e^{i\omega t} + R'_-\, e^{-i\omega t} \tag{75}$$

And from (14) we obtain the rotary form of the deviation current equations

$$i(f+\omega)R'_+ = \frac{1}{h^2}\frac{\partial}{\partial s}(\nu\frac{\partial R'_+}{\partial s}) - \frac{1}{\rho h}(T^o_+ - T^h_+) + \nu_H \bigtriangledown^2_h\, R'_+ \tag{76a}$$

$$i(f-\omega)R'_- = \frac{1}{h^2}\frac{\partial}{\partial s}(\nu\frac{\partial R'_-}{\partial s}) - \frac{1}{\rho h}(T^o_- - T^h_-) + \nu_H \bigtriangledown^2_h\, R'_- \tag{76b}$$

This is possible only if the shear stresses are linear, i.e. can be written

$$\tau_x = \tau_{xo}\cos(\omega t - \delta_{\tau x}), \qquad \tau_y = \tau_{yo}\cos(\omega t - \delta_{\tau y}) \tag{77}$$

and

$$T \equiv \tau_x + i\,\tau_y = T_+\, e^{i\omega t} + T_-\, e^{-i\omega t} \tag{78}$$

In analogy with the tidal current , the periodic shear stresses may be described by a shear stress ellipse, defined in (69) where $R_\pm$ is replaced by $T_\pm$. The complex shear stresses at sea surface and sea bed T_o and T_h can then be written in rotary components such as

$$T_o = T|_{s=0} = T^o_+\, e^{i\omega t} + T^o_-\, e^{-i\omega t}, \qquad T_h = T|_{s=-1} = T^h_+\, e^{i\omega t} + T^h_-\, e^{-i\omega t}. \tag{79}$$

With a linear friction law(16) and (23) for sea bed and sea bed respectively we have

$$T^h_\pm = k\rho\overline{R}_\pm, \qquad T^o_\pm = k_i\rho\overline{R}_\pm. \tag{80}$$

where k and k_i is given by (18) and (25) respectively, and where

$$\overline{R}_\pm(x,y,t) = \int_{-1}^{0} R_\pm\, ds \tag{81}$$

are the rotary components of the depth mean current.

The boundary conditions for the deviation current described in section 3 can easily be transformed and applied for the rotary components. The slip condition at the sea bed (21) gives

$$R'_\pm|_{-1} = -a_b\overline{R}_\pm \tag{82}$$

and at the surface boundary condition for the ice-covered ocean (27) we have

$$R'_{\pm}|_0 = -a_s(\overline{R}_{\pm} - R^{ice}_{\pm}) \tag{83}$$

The ice velocity w_{ice} are generally not periodic and can then not be divided in rotary components such as $w_{ice} = R^{ice}_{+}e^{i\omega t} + R^{ice}_{-}e^{-i\omega t}$. We have no such problems when the ice is at rest. For the free ocean surface we have the surface condition (39) which is transformed to

$$\frac{\partial R_{\pm}}{\partial s}|_0 = \frac{\partial R'_{\pm}}{\partial s}|_0 = 0 \tag{84}$$

4.2. Analytical solution

The equation (70) describing the tidal motion has an analytical solution for a no-slip bottom boundary condition with a constant eddy viscosity when neglecting the lateral friction and the influence of the tidal potential.
For a constant eddy viscosity $\nu = \nu_o$, (70) can be written

$$\frac{\nu_o}{h^2}\frac{\partial^2 R_+}{\partial s^2} - i(f+\omega)R_+ + E_+ = 0 \tag{85a}$$

$$\frac{\nu_o}{h^2}\frac{\partial^2 R_-}{\partial s^2} - i(f-\omega)R_- + E_- = 0 \tag{85b}$$

where

$$E_{\pm} = -gS_{\pm} = -\frac{1}{\rho h}(T^o_{\pm} - T^h_{\pm}) + i(f \pm \omega)\overline{R}_{\pm} \tag{86}$$

For a free-slip surface boundary condition (84) and a no-slip bed boundary condition (82) with $a_b = 1$ (i.e. $R_{\pm}|_{-1} = 0$) the analytical solution is (Fang and Ichiye, 1980 and Nøst, 1988)

$$R_+(s) = \frac{i\,E_+}{f+\omega}\left(\frac{\cosh(k_+ s)}{\cosh(k_+)} - 1\right), \tag{87}$$

$$R_-(s) = \begin{cases} \frac{i\,E_-}{f-\omega}\left(\frac{\cosh(k_- s)}{\cosh(k_-)} - 1\right) & \text{for } f > \omega, \\ -\frac{i\,E_-}{\omega-f}\left(\frac{\cos(k_- s)}{\cos(k_-)} - 1\right) & \text{for } f < \omega, \\ -\frac{h^2 E_-}{2\nu_o}(s^2 - 1) & \text{for } f = \omega. \end{cases} \tag{88}$$

For a no-slip surface boundary condition (83) with $a_s = 1$ and with $R^{ice}_{\pm} = 0$ and a no-slip bed boundary condition (82) with $a_b = 1$ the analytical solution is

$$R_+(s) = \frac{i\,E_+}{f+\omega}\left(\frac{\cosh(k_+) - 1}{\sinh(k_+)}\sinh(k_+ s) + \cosh(k_+ s) - 1\right), \tag{89}$$

$$R_-(s) = \begin{cases} \frac{i\,E_-}{f-\omega}\left(\frac{\cosh(k_-)-1}{\sinh(k_-)}\sinh(k_- s) + \cosh(k_- s) - 1\right) & \text{for } f > \omega, \\ -\frac{i\,E_-}{\omega-f}\left(\frac{\cos(k_-)-1}{\sin(k_-)}\sin(k_- s) + \cos(k_- s) - 1\right) & \text{for } f < \omega, \\ -\frac{h^2 E_-}{2\nu_o}(s^2 + s) & \text{for } f = \omega. \end{cases} \tag{90}$$

where $k_+^2 = i\,h^2\frac{f+\omega}{\nu_o}$ and $k_-^2 = i\,h^2\frac{|f-\omega|}{\nu_o}$

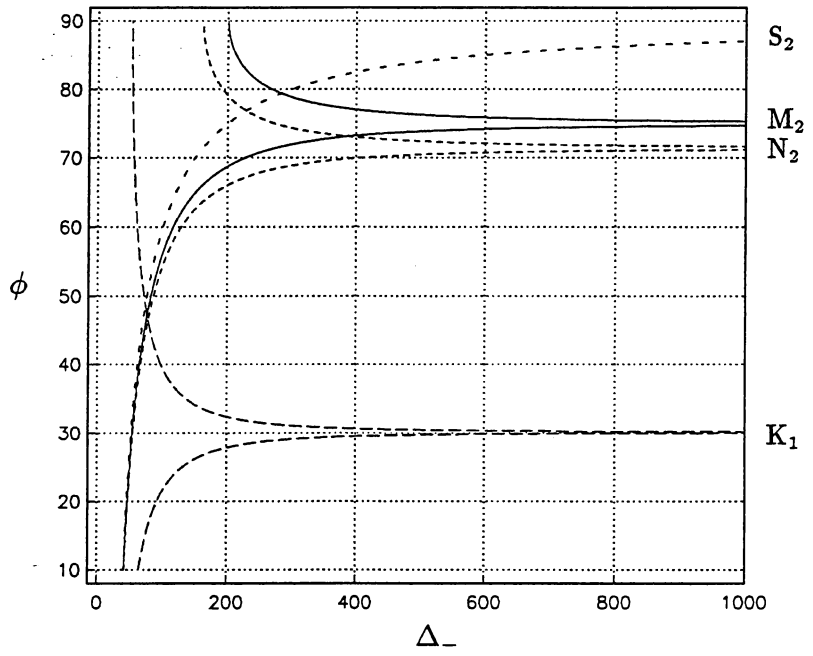

Figure 7: *The boundary layer thickness of the anticyclonic component (Δ_-) as a function of latitude (ϕ, ^oN), ν_o=100 cm^2/s*

4.3. Turbulent boundary layer thickness

In analogy with Ekman's theory (referanse) for wind driven currents, two boundary layer thickness can be defined for constant eddy viscosity ν_o (Davies,1985)

$$\Delta_+ = \pi\sqrt{\frac{2\nu_o}{|f+\omega|}} \qquad \Delta_- = \pi\sqrt{\frac{2\nu_o}{|f-\omega|}} \tag{91}$$

Soulsby (1983) also defines two boundary layer thickness which are proportional to $1/(\omega+f)$ and $1/(\omega-f)$ for the cyclonic and anticyclonic components respectively.
The cyclonic component is much thinner than that for the anticyclonic component ($\Delta_- > \Delta_+$) when $f > 0$ i.e. at the northern hemisphere, and Δ_+ is contained within Δ_-. All the other features of the velocity structure will also have smaller vertical extent for the cyclonic than for the anticyclonic component (Soulsby, 1983), and this effect will be even more pronounced when f approaches ω. Δ_- as a function of the latitude ϕ is shown in figure 7. In the case where the ocean is ice-covered there will exist a boundary layer of the cyclonic and the anticyclonic components at the sea surface as well as at the sea bed.
The boundary layer thickness Δ_- goes to infinity when the frequency of inertia (Coriolis frequency, $f = 2\Omega\sin\phi$) approaches the frequency of the tidal constituent (ω). So, in tidal flow the viscous effects will to be a dominating factor at latitudes where the tidal frequency equals the Coriolis frequency ($\omega = f = 2\Omega\sin\phi_{crit.}$, 'critical' latitude). The critical latitudes for the tidal constituents M_2, S_2 ,N_2 and K_1 at the northern hemisphere are

$$\phi_{M_2} = 75^o2.8'N \qquad \phi_{S_2} = 89^o55.8'N$$

$$\phi_{N_2} = 71^o26.4'N \qquad \phi_{K_1} = 30^o5.4'N$$

as shown by the plots in figure 7. The Barents sea includes the critical latitudes for semi-diurnal tides.

The same situation arises in the southern hemisphere, where f is negative. Here the boundary layer of the cyclonic component (Δ_+) becomes larger for latitudes where $|f| \to \omega$.

4.4. Numerical solution

The entire computational procedure for extracting current profiles from two-dimensional depth integrated models is described in section 3.1. In this section this computation procedure will be applied to solve the set of equations (70) for tidal flow. In the following the solution of the depth integrated equations i.e. the surface gradient $S_\pm$ and the depth mean current $\overline{R}_\pm$, will not be discussed in detail, but will be further specified in the applications in section 5.
In section 4.4.1. we will concentrate on finding the solution of (76) i.e. $R'_\pm$, and then present the rotary components of the total current $(R_\pm = \overline{R}_\pm + R'_\pm)$ as the solution of (70). Furthermore we will discuss the consistency of the entire computation procedure in section 4.4.2.

4.4.1. Solution using the Galerkin method

In order to find the solution of (76) by using the Galerkin method as described in section 3.2 the trial functions w_N is expressed in rotary components. (35) and (75) gives

$$w' = (w_{o+} + \sum_{r=1}^{N} c_{r+} w_r)\, e^{i\omega t} + (w_{o-} + \sum_{r=1}^{N} c_{r-} w_r)\, e^{-i\omega t} \tag{92}$$

where $c_{r\pm}$ and $w_{o\pm}$ are constants independent of time defined respectively

$$c_r = c_{r+}\, e^{i\omega t} + c_{r-}\, e^{-i\omega t}, \tag{93}$$

$$w_o = w_{o+}\, e^{i\omega t} + w_{o-}\, e^{-i\omega t} \tag{94}$$

With orthogonal trial functions defined by the eigenvalue-problem (43) the coefficients c_r are given by equation (47). For periodic functions we have $\frac{\partial c_r}{\partial t} = i\omega(c_{r+}e^{i\omega t} - c_{r-}e^{-i\omega t})$ and eq (47) leads to

$$c_{r\pm} = \frac{E_{r,\pm}\, F_r}{i(f \pm \omega) + \nu_o \frac{\varepsilon_r}{h^2}} \tag{95}$$

provided that $E_r(t)$ defined in (48) can be expressed in rotary components i.e. $E_r(t) = E_{r,+}\, e^{i\omega t} + E_{r,-}\, e^{-i\omega t}$. F_r is given in (49).
By (75) and (92) the rotary components of the deviation current, $R'_\pm$ are then given by

$$R'_\pm = w_{o\pm} + \sum_{r=1}^{N} \frac{E_{r,\pm}}{i(f \pm \omega) + \nu_o \frac{\varepsilon_r}{h^2}} F_r w_r(s) \tag{96}$$

and the rotary components of the total current are then

$$R_\pm = \overline{R}_\pm + w_{o\pm} + \sum_{r=1}^{N} \frac{E_{r,\pm}}{i(f \pm \omega) + \nu_o \frac{\varepsilon_r}{h^2}} F_r w_r(s) \tag{97}$$

In the case where we have an ice covered sea surface at rest (section 3.2.1.) as in (52) we have

$$w_{o\pm} = -[(a_s - a_b)\, s + a_b]\overline{R}_\pm \tag{98}$$

and by (53) that

$$E_{r,\pm} = -\frac{1}{\rho h}(T^o_\pm - T^h_\pm)\int_{-1}^{0} w_r ds + i(f \pm \omega)\overline{R}_\pm)\int_{-1}^{0}[(a_s - a_b)s + a_s]w_r ds +$$

$$\frac{\nu_o}{h}\overline{R}_\pm(a_s - a_b)\int_{-1}^{0}\phi(s)\frac{\partial w_r}{\partial s}ds \qquad (99)$$

And in the case where we have a free ocean surface (section 3.2.2.) as in (58) we have

$$w_{o\pm} = -a_b\overline{R}_\pm \qquad (100)$$

and (59) gives for $E_{r,\pm}$

$$E_{r,\pm} = [-\frac{1}{\rho h}(T^o_\pm - T^h_\pm) + a_b i(f \pm \omega)\overline{R}_\pm]\int_{-1}^{0} w_r ds \qquad (101)$$

Specially for a no-slip condition at sea bed and surface i.e. $a_s = a_b = 1$, or a free ocean surface (58) and a no slip bed condition i.e. $a_b = 1$ we have

$$w_{o\pm} = -\overline{R}_\pm \qquad (102)$$

and

$$E_{r,\pm} = [-\frac{1}{\rho h}(T^o_\pm - T^h_\pm) + i(f \pm \omega)\overline{R}_\pm]\int_{-1}^{0} w_r ds \qquad (103)$$

And the rotary components of the total current may be written

$$R_\pm = \sum_{r=1}^{N} \frac{-\frac{1}{\rho h}(T^o_\pm - T^h_\pm) + i(f \pm \omega)\overline{R}_\pm}{i(f \pm \omega) + \nu_o\frac{\varepsilon_r}{h^2}} \frac{\int_{-1}^{0} w_r ds}{\int_{-1}^{0} w_r^2 ds} w_r(s) \qquad (104)$$

By (57) $E_{r,\pm}$ in (103) may be determined by the surface gradient when neglecting the direct influence of the tide generating potential and the lateral friction. When applying (73) we obtain

$$E_{r,\pm} = -g\, S_\pm \int_{-1}^{0} w_r ds \qquad (105)$$

And the rotary components of the total current may be written

$$R_\pm = \sum_{r=1}^{N} \frac{g\, S_\pm}{i(f \pm \omega) + \nu_o\frac{\varepsilon_r}{h^2}} \frac{\int_{-1}^{0} w_r ds}{\int_{-1}^{0} w_r^2 ds} w_r(s) \qquad (106)$$

Which is how Davies (1985) has expressed the rotary components.

4.4.2. Consistency of the method

The computation procedure for extracting current profiles from two-dimensional depth integrated models used for finding a solution of (70), is based on the two sets of equations for the depth mean current (13) and for the deviation current (14). These two sets of equations are coupled together through the boundary conditions (5) i.e. the sea surface and sea bed shear stresses and the definition of the depth-averaged current (3).

Firstly, when using this method for extracting current profiles from two dimensional depth integrated models, it is important to test that the shear stresses from the depth integrated model are equal to the shear stresses derived from the current profile calculations. The shear stresses from the depth integrated model is given by the friction law (16) and (23) for the sea bed and surface respectively, and the shear stresses derived from the current profile calculations is given by (5). The bed shear stresses depends upon the value of the eddy viscosity and the velocity gradient at sea bed which may be changed by applying different viscosity profiles (fig.1) and different degrees of a slip bed condition given by the value of the parameter a_b introduced in (21). The bed shear stresses computed from the current profile calculations is made to fit the stresses from the depth integrated model by a suitable choice of the eddy viscosity profile and the slip condition with (107) as a constraint. The same procedure must be applied to test the consistency for the shear stress at the sea surface.

The second requirement for consistency of the method is that relation (9) derived from eq. (3), is maintained. One way of fulfilling this requirement may be to use the magnitude of the eddy viscosity (ν_o) as a tuning parameter such that the computed current profile has the same depth mean value as the mean current from the depth integrated model. In this work this is done in the numerical procedure by demanding that the square root of the current amplitudes from the depth integrated model is equal to the depth mean of the computed current amplitudes i.e.

$$\sqrt{\overline{u}_o^2 + \overline{v}_o^2} = \frac{1}{j_{max}} \sum_{j}^{j_{max}} \sqrt{u_{oj}^2 + v_{oj}^2} \tag{107}$$

where j is a counter in the vertical.

Davies who first introduced the method of extracting current profiles from depth integrated models, formulated it first for wind driven currents (Davies 1986 and 1987). A special version of this for tidal motion is presented in Davies (1990). Here Davies focus on comparing the results with a fully three dimensional tidal model, and concludes with an acceptable accuracy. Davies says that the bed stresses is not guaranteed to match that in the integrated model unlike in his enhanced bed stress method (Davies 1987, 1988), but can be made to match it in an iterative manner by a suitable choice of the eddy viscosity profile. Davies (1990) does not inquire whether the depth mean current from the integrated model equals the depth mean current from the profile calculations, and he gives the value of ν_o which is related to the flow field, by

$$\nu_o = \frac{1}{P} \int_0^P \mu(t) dt, \qquad \mu(t) = \begin{cases} const.\ (\overline{u}^2 + \overline{v}^2) \\ const.\ (\overline{u}^2 + \overline{v}^2)^{\frac{1}{2}} \end{cases} \tag{108}$$

(where P is the tidal period) representing a tidally averaged eddy viscosity.

Zitman (1990) has also used Davies method as a starting point to formulate a method to analyze the vertical structure of the horizontal current velocity components. He ends up with an overcomplete set of equations ($m+4$ equations and $m+2$ unknowns) and leaves out the two equations of 'highest-frequency' (i.e. the Galerkin equations $m+3$ and $m+4$), and claims that this allows for an exact representation of the depth-averaged current velocity and the applied wind surface stress, whereas the Galerkin optimization only is partly realized. Zitman in his progress report (1990) presents no results on the testing of the consistency of his method.

4.5. Current profile calculations

In order to examine the influence of the eddy viscosity (constant), water depth and geographical latitude upon tidal current profiles, we will study the case where the inviscid solution defined in (74) is determined such that we have rectilinear flow in the x-direction with amplitude 1.0 m/s ($\Rightarrow R_{\pm} = 0.5$). In all the examples considered below we then will have

$$\lim_{\nu_o \to 0} R_{\pm}(z) = R_{\pm,inviscid} = 0.5 \tag{109}$$

when computing the current profiles by the numerical solution (106). This gives

$$E_{r,\pm} = E_{\pm} \int_{-1}^{0} w_r ds \tag{110}$$

where

$$E_{\pm} = -gS_{\pm,inviscid} = i(f \pm \omega)R_{\pm,inviscid} = i(f \pm \omega)0.5 \tag{111}$$

The results from this analysis is given in section 4.5.1.
In the various current profile calculations the consistency requirements described in section 4.4.2 are not considered, it is the relation (109) which connects the current profiles together. A complete application of the method where the consistency of the method is discussed and various eddy viscosity profiles applied, is done in section 5.
In the examples given below we have applied a no-slip bed boundary condition and a constant eddy viscosity, and for these cases there exists an analytical solution (87)–(90) to which the numerical solution (106) can be compared. This is done in section 4.5.2.

4.5.1. Parameter dependence

The figures 8–17 shows the vertical distribution of the normalized major semi axis $\tilde{A}$ (normalized by the free stream value) of the tidal current ellipse computed from the rotary components by (69a), the eccentricity ε defined in (69e) and the x-component of the stress amplitude divided by the density (τ_{xo}/ρ) for three different values of the constant eddy viscosity.
The current profiles are computed for $f = 1.2 \cdot 10^{-4} s^{-1}$ which corresponds to a position in the North Sea at 55.6 degree North, a position which Davies (1985) has used in his test examples. The other position where the current profiles will be computed is at 74.3 degrees North where $f = 1.4 \cdot 10^{-4} s^{-1}$ and which is close to the 'critical' latitude for the M_2 constituent and where

we expect large viscous effects for the semi-diurnal tides.

Figure 8 shows the M_2 current ellipse components at 55.6°N in water depth of 100 meters and where a free-slip surface boundary condition is applied. For relatively small values of the constant eddy viscosity ($\nu_o = 10$ cm^2/s) the normalized major semi axis $\tilde{A}$ increases rapidly in the near bed region, exceeds the free stream value and falls back to its free stream value at about 40 meters above sea bed i.e. below sea surface. The eccentricity and the stress component are nonzero only in the near bed region. It is evident from figure 8 that the bottom boundary layer is less than the water depth and occupy a region near the sea bed. This is confirmed by realizing that in this particular case the boundary thickness Δ_- defined in (91) is 31 meter. For larger values of $\nu_o = 1000$ and 100 cm^2/s we have a uniform increase of $\tilde{A}$ with distance above sea bed. $\tilde{A}$ exceeds the free stream value at about mid-depth and are slightly larger than the free stream value at sea surface for $\nu_o = 100$ cm^2/s. The eccentricity is negative in the same depth region. For $\nu_o = 1000$ cm^2/s the free stream value is not attained before sea surface is reached. The eccentricity decreases with distance above sea bed and does not either reach the free stream value at sea surface, and are positive at all depths. The boundary layer thickness Δ_- is 98 meters ($\sim$ water depth) for $\nu_o = 100$ and 310 meters ($\gg$ water depth) for $\nu_o = 1000$ cm^2/s.

Figure 9 the depth variation of the the K_1 current ellipse parameters. There are no significant difference in the depth variation compared to the results in figure 8. The bottom boundary layer may be slightly smaller i.e. the major semi-axis increases more rapidly with distance from sea bed and the region near sea bed where ϵ and τ_{xo} are nonzero is smaller than for the M_2 tide. The boundary layer thickness $\Delta_- = 20$, 65 and 205 meters for $\nu_o = 10$, 100 and 1000 cm^2/s respectively i.e. larger than the water depth only for the highest value of the constant eddy viscosity.

Figure 10 and 11 for the M_2 and K_1 constituents respectively show profiles of ellipse parameters at 74.3°N i.e. close to the M_2-critical latitude but further away from the K_1-critical latitude.
The K_1 profiles are practically similar at 55.6°N (fig.9) and at 74.3°N (fig.11). And the boundary layer thickness Δ_- are slightly smaller at 74.3°N (fig.7) than at 55.6°N this is because we are further away from the K_1-critical latitude.
The changes for the M_2 profiles are more dramatic. For ν_o =100 cm^2/s and 1000 cm^2/s the vertical variations of $\tilde{A}$ seems similar, but the surface value at 74.3°N (fig.10a) is about half of what it is at 55.6°N (fig.8a) i.e. about half the free stream value. The eccentricity is very different, at 74.3°N (fig.10b) ϵ is almost constant equal to one for ν_o =1000 cm^2/s while at 55.6°N (fig.8b) ϵ starts at 0.5 at sea bed and decreases with distance above sea bed. The motion at 74.3°N is practically circular at all depth while at 55.6°N it becomes more and more rectilinear with distance above sea bed. At both latitudes the direction of rotation is cyclonic ($\epsilon > 0$). For ν_o =100 cm^2/s ϵ decreases uniformly with distance above sea bed at both latitudes; at 74.3°N ϵ starts at about 1. at sea bed and are > 0.5 in all depths while at 55.6°N ϵ starts at 0.5 and becomes negative at sea surface i.e. the direction of rotation changes at 55.6 °N but are cyclonic in all depths at 74.3°N. For ν_o =10 cm^2/s $\tilde{A}$ does not exceed the free stream value before about 25 meters below sea surface at 74.3°N and ϵ is negative where $\tilde{A}$ is larger than the one. The boundary layer thickness is larger than the sea depth. The boundary layer thickness Δ_- is 1950, 617 and 195 meters for $\nu_o = 1000$, 100 and

10 cm^2/s respectively i.e. $\gg$ water depth.
In figure 12 the M_2-profiles at 55.6°N (from fig.8) and at 74.3°N (from fig.10) are plotted for comparison. Figure 13 shows the same for the K_1-profiles. As said earlier the K_1-tidal current profile does not change much during the latitude change from the North Sea to the Barents sea, while the M_2-tidal current profile is a lot more affected by the change in latitude. The main effect is that the motion tends to be more circular and that the current value varies more in the same eddy viscosity range.

As far north as 74.3 degrees the ice cover may influence the current profile near the sea surface. In order to model the effect a solid ice cover has upon the current profiles, the no-slip surface boundary condition is applied. The figures 14 and 15 show the profiles of the M_2 and K_1 tidal ellipse parameters. We now have two boundary layers, one at sea surface and one at sea bed. As seen in figure 14 and 15 these two boundary layers seems similar and has the same character as the bed boundary layer in the free surface case i.e. the vertical variation with distance from the boundary are similar. The stress amplitude has the same boundary value at the two boundaries and are zero at mid-depth. The profiles are symmetric around mid-depth for a constant eddy viscosity.
In a more realistic situation one would assume that the ice-water friction interaction are different from the friction between the sea bed and the water. And that the eddy viscosity are different in these two boundaries which results in two different boundary layers. A further investigation of the effect of an ice-covered ocean upon the tidal currents will be done later when a depth varying eddy viscosity is considered (section 5.2).

Davies (1985) discusses the influence of sea depth variation upon the vertical variations of the tidal current at 55.6°N, and concludes that there exists two physically different situations, one where the near bed stress layer are less than the water depth and the tidal current profile is characterized by a profile within this stress layer which is determined by the variation of viscosity. Above this stress layer the tidal current is essentially constant and attain the free stream value. The second situation where the stress layer exceeds the water depth, the tidal current profile in the entire water column is influenced by water depth and the viscosity distribution.
In order to investigate the same problem at 74.3°N, near the critical latitude for the M_2 constituent, we also have computed tidal current profiles in sea depth of 300 meters (fig.16), and in sea depth of 30 meters (fig.17) for a free-slip surface boundary condition. For both depths the boundary layer thickness (Δ_-) is larger than the water depth
For water depth of 30 m the current ($\tilde{A}$) never attain the free stream value and are less than the half of the free stream value for all the three eddy viscosity values. The motion is about circular for ν_o=1000 and 100 cm^2/s ($\varepsilon \sim 1$) and for ν_o=10 cm^2/s the motion is closer to be circular than rectilinear ($0.5 < \varepsilon < 1$).
The vertical distribution of $\tilde{A}$ and ε are similar for $h = 30, \nu_o = 0.001$ and $h = 300, \nu_o = 0.1$. In these two examples the factor ν_0/h^2 in front of ε_r in (96) are identical. The τ_{xo}/ρ-profile are however different in these two situations.
The K_1 profiles are also calculated in the water depth of 30 m and 300 m in figures 18 and 19 respectively. Here we still have the two physically different situation which Davies describes (1985) because for the K_1-tide we still are far from the critical latitude in the Barents sea (74.3°N).

Latitude (°N)	Depth (m)	Tidal const.	Eddy viscosity: ν_o						Fig. nr.
			1000 (cm^2/s)		100 (cm^2/s)		10 (cm^2/s)		
			N	$\triangle s$	N	$\triangle s$	N	$\triangle s$	
55.6	100	M_2	10	$\frac{1}{100}$	10	$\frac{1}{100}$	35	$\frac{1}{200}$	8
		K_1	10	$\frac{1}{100}$	10	$\frac{1}{100}$	30	$\frac{1}{200}$	9
74.3	30	M_2	10	$\frac{1}{100}$	10	$\frac{1}{100}$	10	$\frac{1}{100}$	16
		K_1	10	$\frac{1}{100}$	10	$\frac{1}{100}$	20	$\frac{1}{200}$	18
	100	M_2	10	$\frac{1}{100}$	10	$\frac{1}{100}$	30	$\frac{1}{200}$	10
		K_1	10	$\frac{1}{100}$	10	$\frac{1}{100}$	35	$\frac{1}{200}$	11
	300	M_2	30	$\frac{1}{200}$	30	$\frac{1}{200}$	90	$\frac{1}{500}$	17
		K_1	10	$\frac{1}{100}$	35	$\frac{1}{200}$	80	$\frac{1}{500}$	19

Table 2: *N – is the number of terms in the Galerkin expansion and $\triangle s$ – is the grid resolution required for keeping the error of the N first eigenvalues less than 2 %.*

4.5.2. Accuracy of the numerical solution

By comparing the analytical solution (87)-(90) and the corresponding Galerkin solution (106) where F_r, w_r and ε_r are determined from the analytical solution (64) of the eigenvalue problem, the number of terms N needed to obtain an acceptable accuracy of 2% as defined in section 3.3., may by found. For the tidal profile test examples presented in the previous section (4.5.1) N is given in table 2.

When F_r, w_r and ε_r in the Galerkin solution are determined from the numerical solution (61) of the eigenvalue problem, N determines the depth resolution $\triangle s$ for a specified relative error $\triangle \varepsilon$ defined in (65) and shown in figure 3. The $\triangle s$ that is needed for the numerical eigenvalues to be within 2% of the analytical eigenvalues are also given in table 2 for the tidal profile test examples. There are no significant changes in N when a no- or free-slip surface boundary condition is applied, therefore only the profile examples with a free-slip surface boundary condition are presented in table 2.

N (and then $\triangle s$) is found to be dependent mainly upon the water depth and the value of the eddy viscosity. The tidal current profiles characterized by a high shear region near the boundaries i.e. situations where we have deep water and where we have small values of the eddy viscosity, need more terms N in the Galerkin solution. And from this it follows that in these cases a high grid resolution in the vertical direction in the numerical calculation is required.

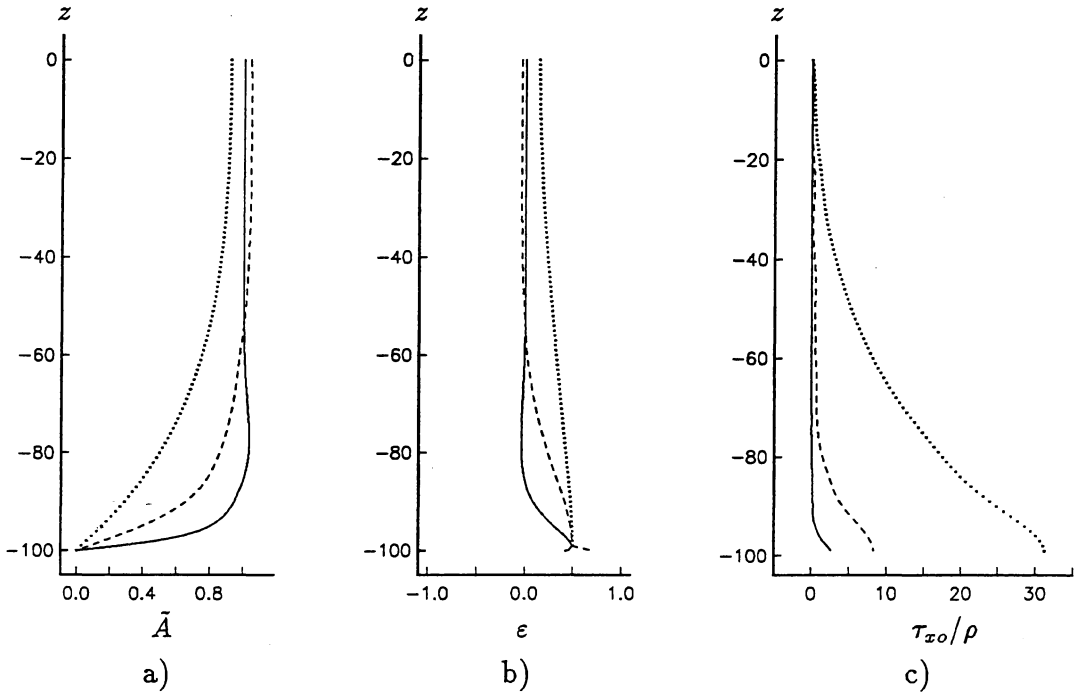

Figure 8: *Profiles for M_2-tidal ellipse parameters at 55.6°N in water depth of 100 m for different values of constant eddy viscosity ν_o =1000 cm^2/s (.....), 100 cm^2/s (- - -) and 10 cm^2/s (——), for a free-slip surface boundary condition. (a) $\tilde{A}$, normalized major semi-axis, (b) $\varepsilon = B/A$, eccentricity, (c) τ_{xo}/ρ (cm^2/s^2), shear stress amplitude in x-direction.*

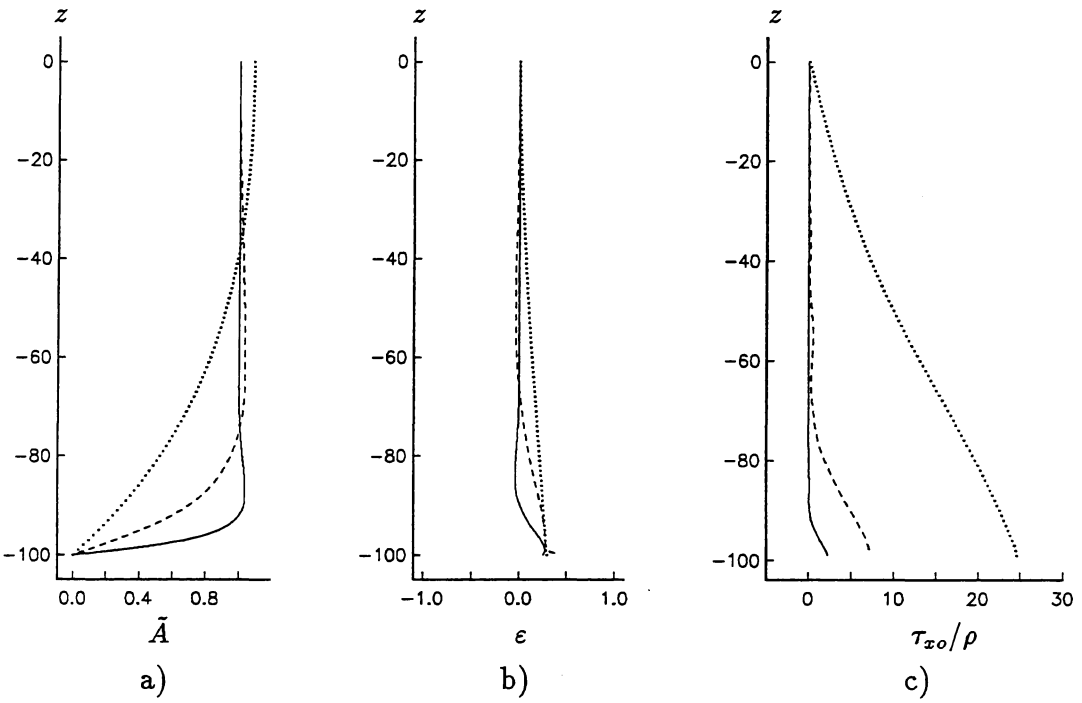

Figure 9: *As figure 8, but for K_1-tidal ellipse parameters.*

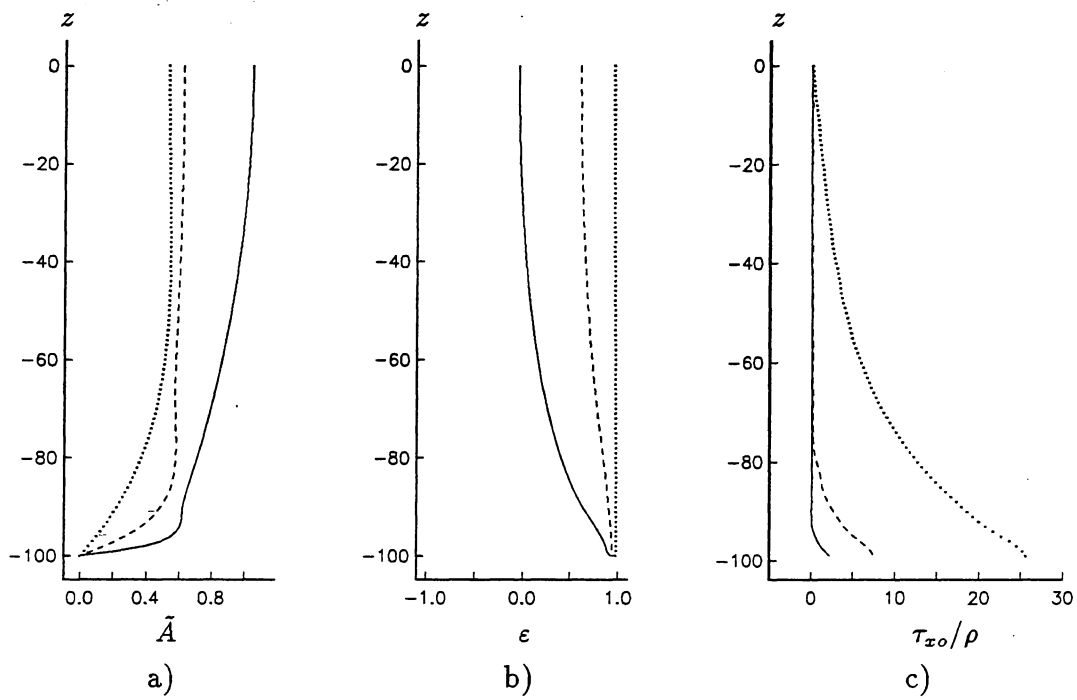

Figure 10: *Profiles for M_2-tidal ellipse parameters at 74.3°N in water depth of 100 m for different values of constant eddy viscosity ν_o =1000 cm^2/s (.....), 100 cm^2/s (- - -) and 10 cm^2/s (——), for a free-slip surface boundary condition. (a) $\tilde{A}$, normalized major semi-axis, (b) $\varepsilon = B/A$, eccentricity, (c) τ_{xo}/ρ (cm^2/s^2), shear stress amplitude in x-direction.*

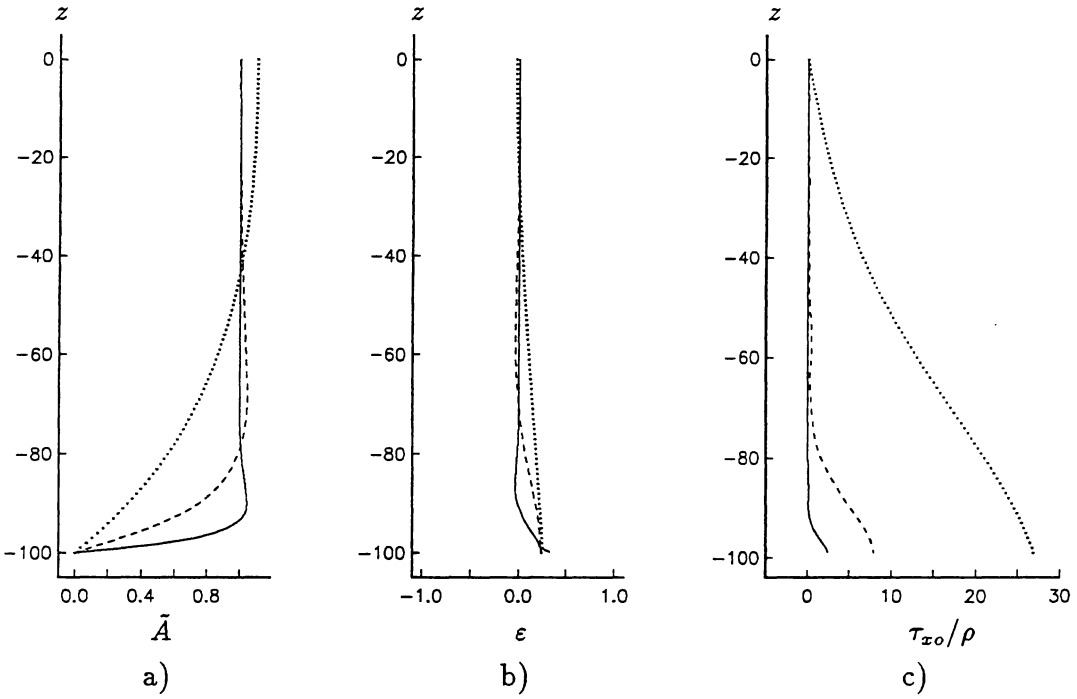

Figure 11: *As figure 10, but for K_1-tidal ellipse parameters.*

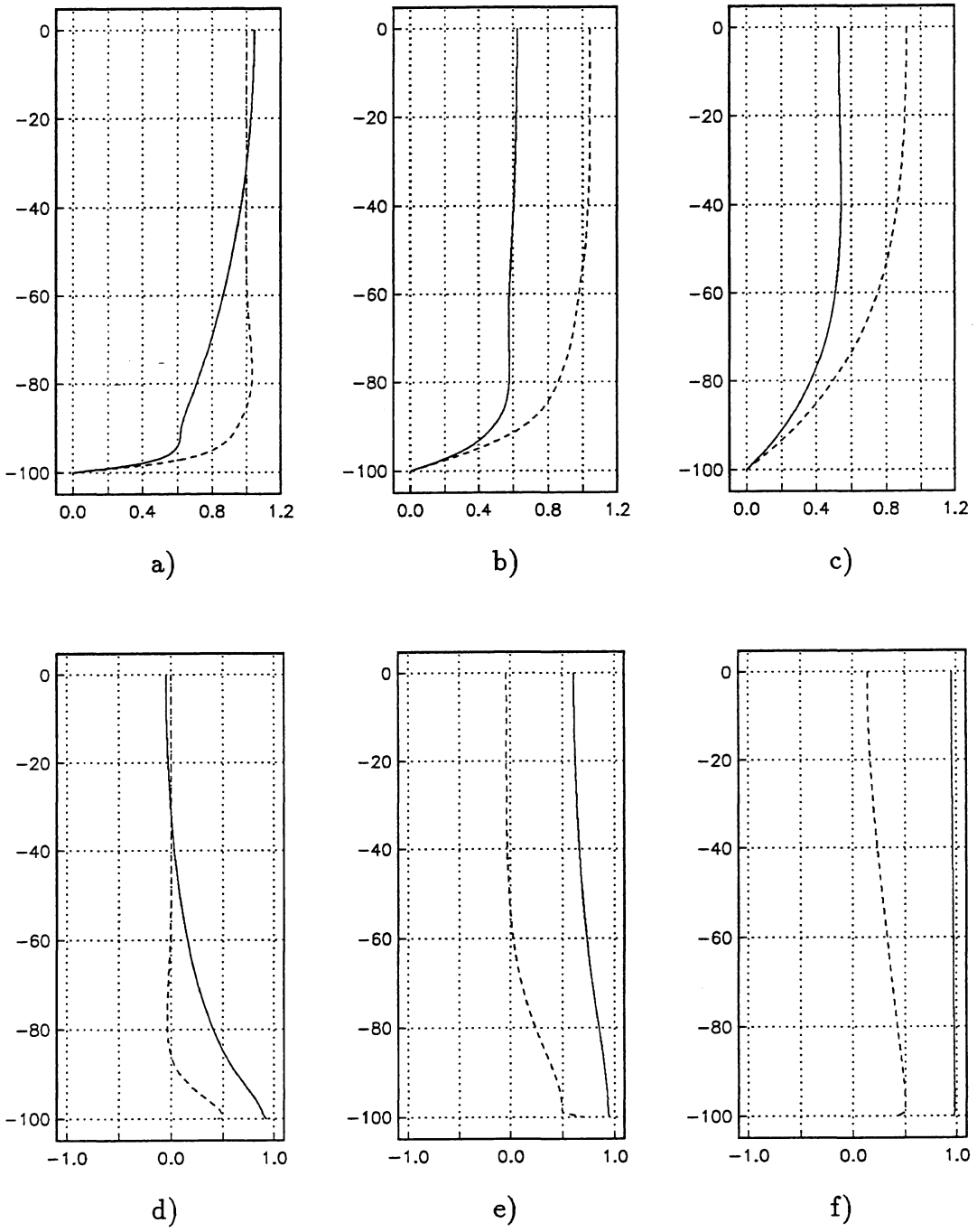

Figure 12: *Comparing M_2 profiles at 55.6°N from figure 8 (- - -) and at 74.3°N from figure 10 (——). a), b) and c) shows the normalized semi-major axis $\tilde{A}$ and d), e) and f) shows the eccentricities ε for ν_o = 10, 100 and 1000 cm^2/s respectively.*

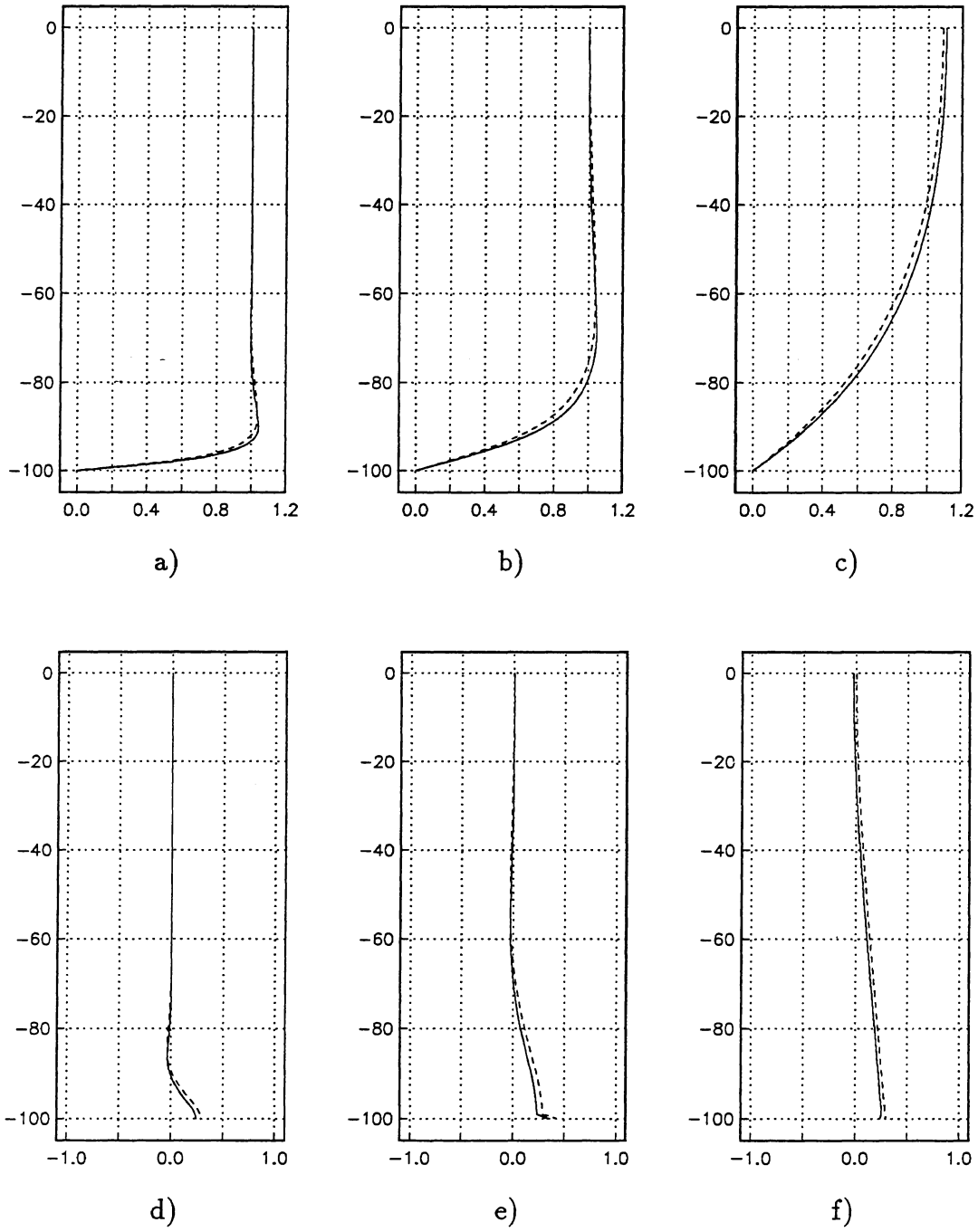

Figure 13: *Comparing K_1 profiles at 55.6°N from figure 9 (- - -) and at 74.3°N from figure 11 (——). a), b) and c) shows the normalized semi-major axis $\tilde{A}$ and d), e) and f) shows the eccentricities ϵ for ν_o = 10, 100 and 1000 cm^2/s respectively.*

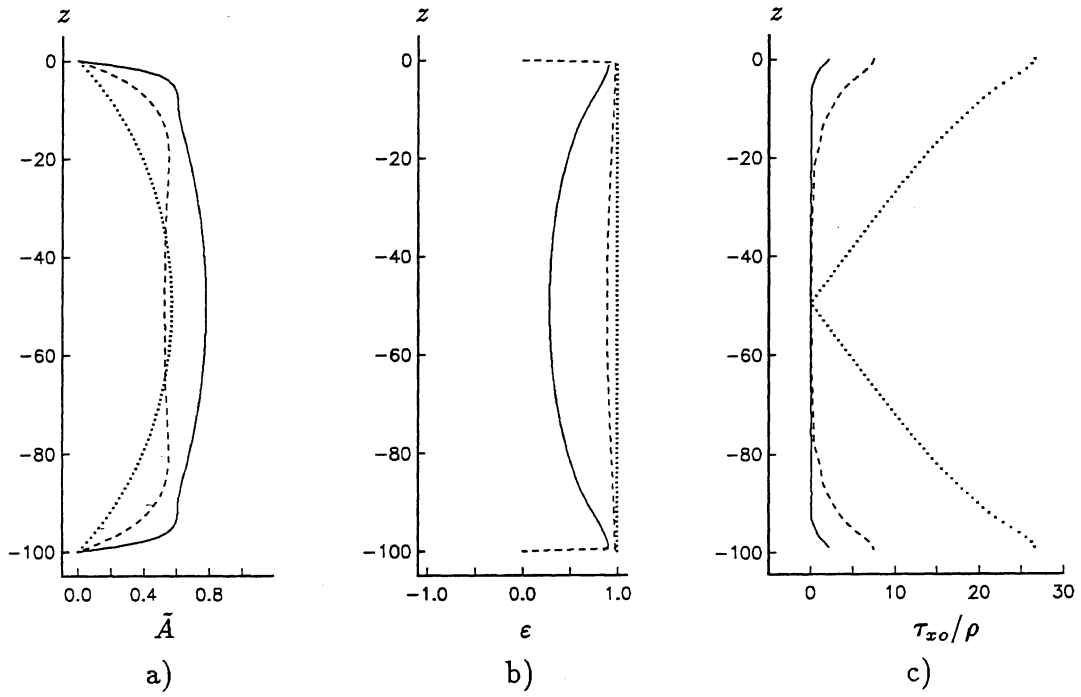

Figure 14: *Profiles for M_2-tidal ellipse parameters at 74.3°N in water depth of 100 m for different values of constant eddy viscosity ν_o =1000 cm^2/s (.....), 100 cm^2/s (- - -) and 10 cm^2/s (——), for a no-slip surface boundary condition. (a) $\tilde{A}$, normalized major semi-axis, (b) $\varepsilon = B/A$, eccentricity, (c) τ_{xo}/ρ (cm^2/s^2), shear stress amplitude in x-direction.*

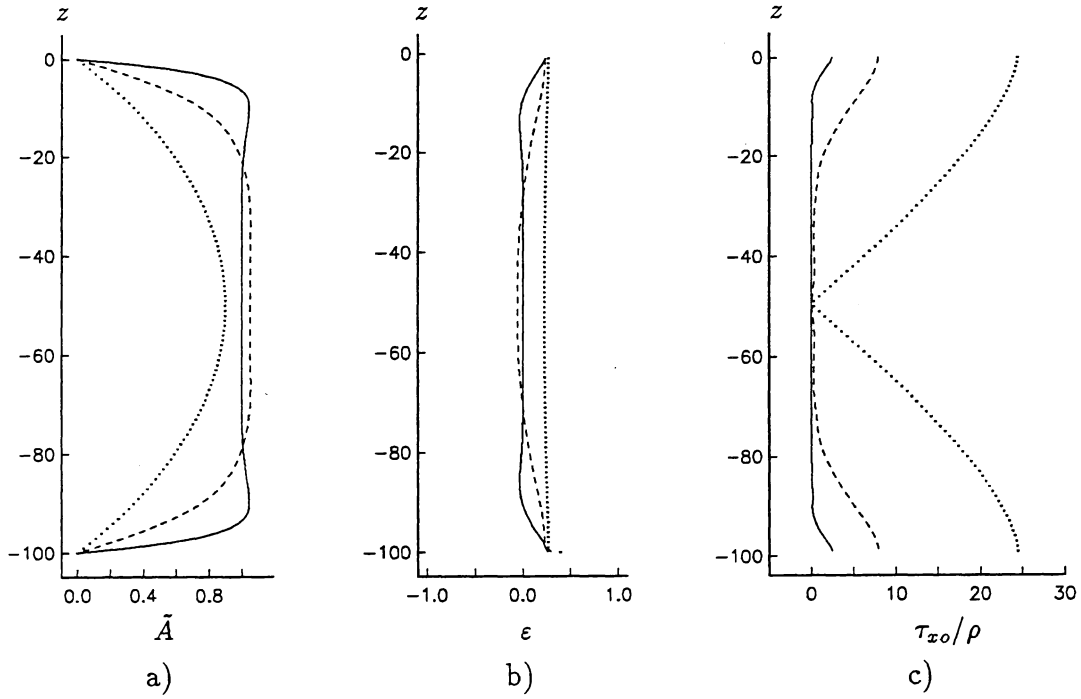

Figure 15: *As figure 14, but for K_1-tidal ellipse parameters.*

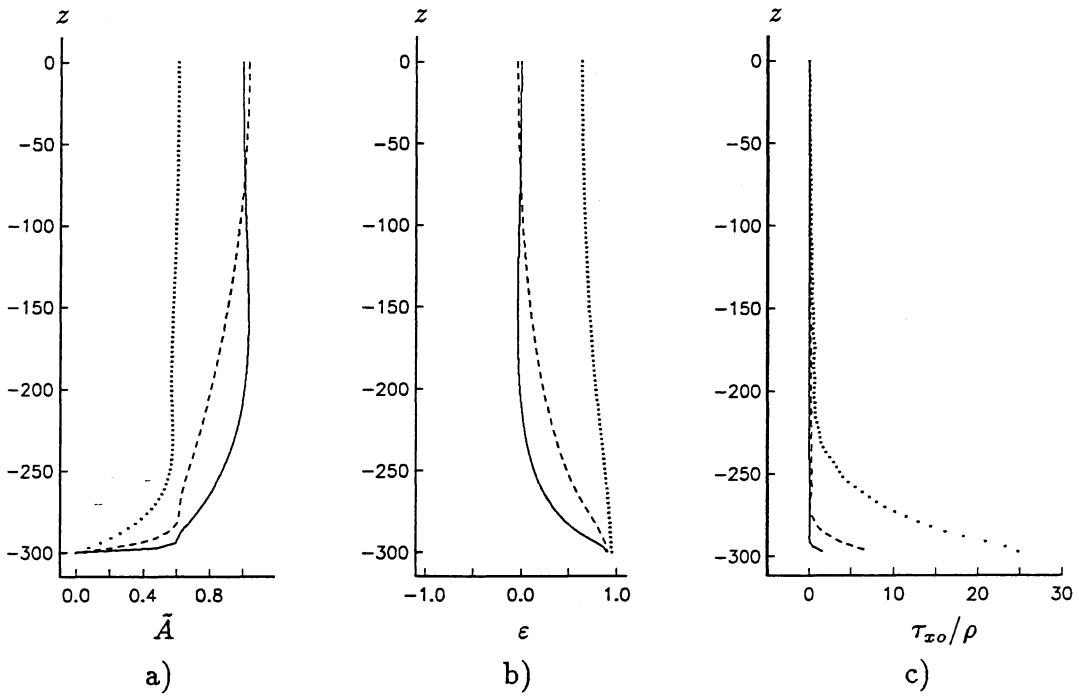

Figure 16: *As figure 10, but in water depth of 300 m.*

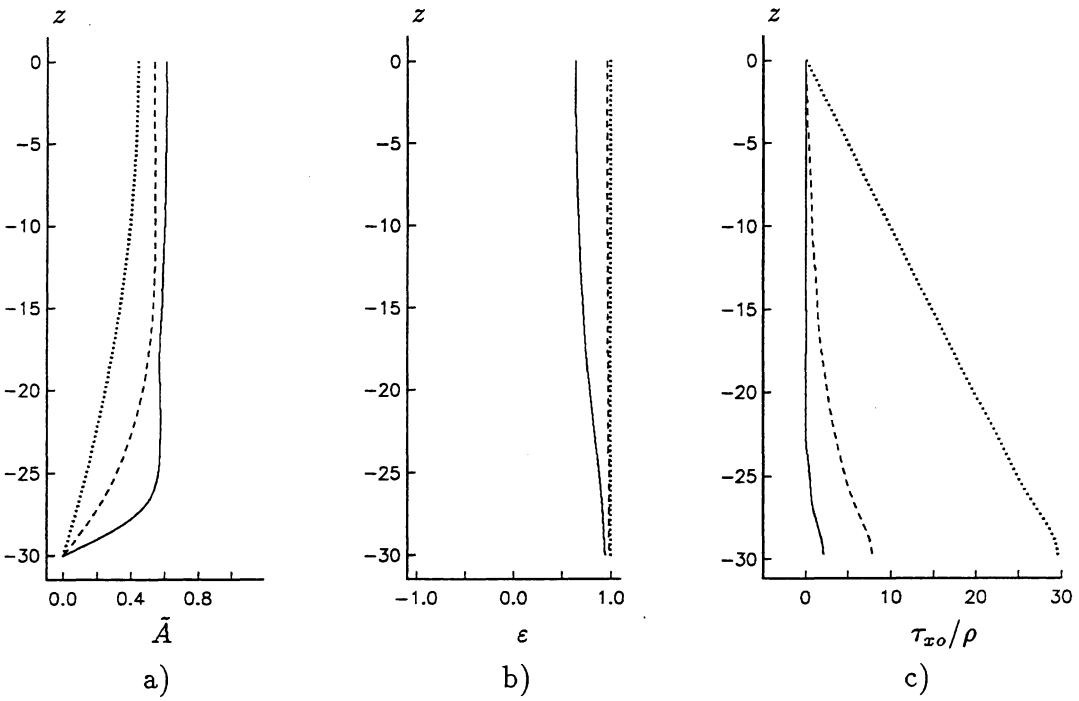

Figure 17: *As figure 10, but in water depth of 30 m.*

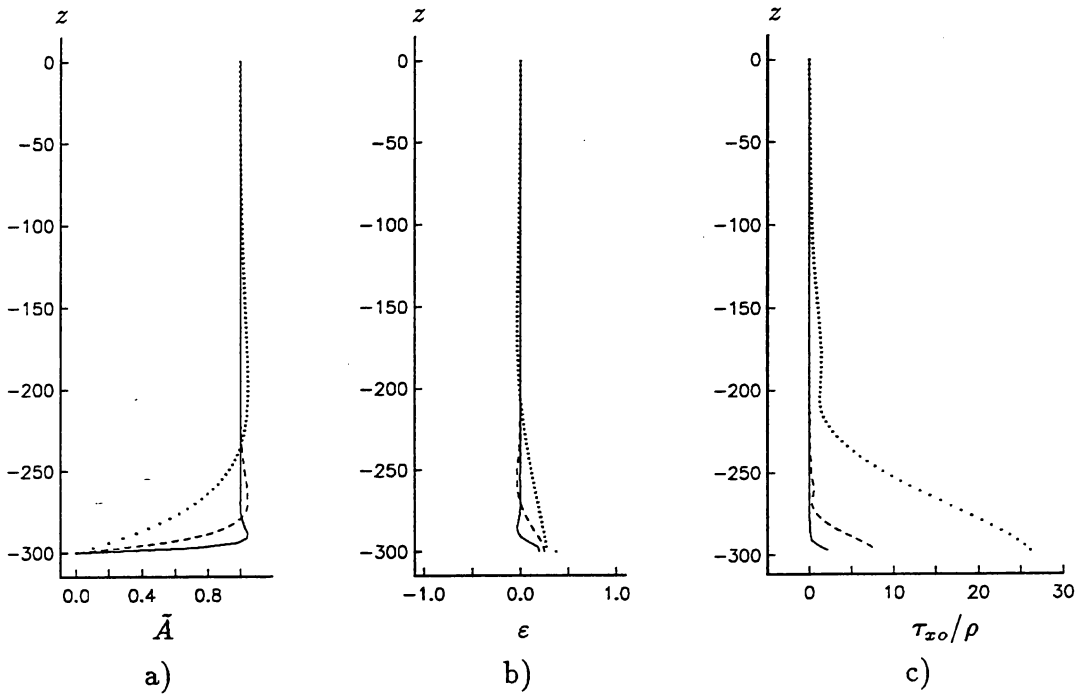

Figure 18: *As figure 11, but in water depth of 300 m.*

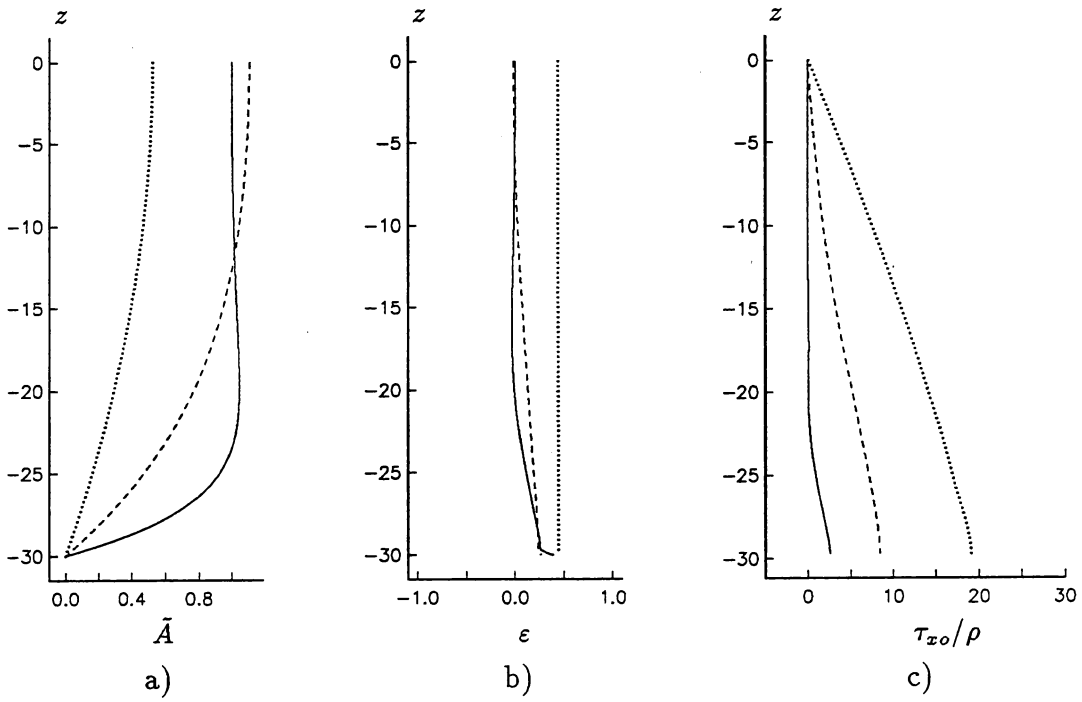

Figure 19: *As figure 11, but in water depth of 30 m.*

5. Tidal current profiles in the Barents sea

The tides in the Barents sea area are strongly influenced by the following; the area includes the critical latitude for the largest semi-diurnal constituents, the steep shelf slope at the west of the Bear Island has a profound effect on the dynamics, and the shallow water depth particularly in the Svalbard bank area introduce strong frictional effects. The tidal current velocity in this region between Svalbard and the Bear Island is to 1 m/s for the M_2 constituent (Gjevik et al. 1990), and this region ice-covered large parts of the year.
Of existing current observations in the Barents sea we have chosen a set of measurements under ice (S2, S3, S4 and S5) and a set of measurements obtained under a free ocean surface (N, A, B9 and B1). The geographical location for these stations are given in figure 20 and they are all located near the critical latitude for the M_2-tide i.e. near 75°2.8'N. These current measurements exists in up to six different depths which the computed current profiles may be compared with. So in this section we will compute the tidal current profiles with different vertical distributions of the eddy viscosity.
Gjevik et al.(1990) presents results from model simulation of the tidal constituents M_2,S_2,N_2 and K_1 in the Barents sea. These results are obtained with a depth integrated two-dimensional model and the harmonic constants for the depth mean current and for the sea elevation for the M_2 and the K_1 tides are given in the tables 3 and 4 for the chosen observations stations. The observed water depth and the model water depth at the different stations are also given in the tables 3 and 4 and are slightly different due to grid resolution effects. The current amplitudes presented in the tables are the 'corrected' currents data obtained by

$$\text{corrected model current} = \text{model current} \times \frac{\text{model water depth}}{\text{observed water depth}} \tag{112}$$

This correction may be an important effect for stations in shallow water but the correction normally does not have any significant effect in deep water.
To achieve a reasonable good agreement between the observed and the computed current profiles, the results from the depth integrated model i.e. the depth mean current, must be in reasonable good agreement with the depth mean of the observed current. This is the case for results from the depth integrated tidal model of Gjevik et al. (1990) at these observation stations, and in the presentation of the results the depth mean values from the depth integrated model are presented by a straight line in the figures 21–32.
The tidal current profiles of the current ellipse parameters presented in the figures 21–32a-d are computed from the rotary components of the total current ($R_\pm = \overline{R}_\pm + R'_\pm$). The ellipse parameters are obtained from the relations (69). The rotary components of the deviation current are computed from (96) with boundary conditions. The depth mean rotary components $\overline{R}_\pm$ are computed from a similar relation as (68) but from the depth mean harmonic constants ($\overline{u}_o$,$\delta_{\overline{u}}$,$\overline{v}_o$ and $\delta_{\overline{v}}$) which are given in the tables 3 and 4 for the different observation stations.
The figures 21–32e and f shows the modulus of the shear stress rotary components ($|T_+|, |T_-|$) in (78) divided by the density. These will be discussed in view of the consistency requirements of the method. A complete representation of the shear stresses would require the arguments also to be shown.
In the computation method used here the eddy viscosity is taken to be of the form (29). The prescribed vertical variation of the eddy viscosity ($\phi(s)$) determine the expansion functions (w_r) and the eigenvalues (ε_r) in the eigenvalue problem (43). The numerical solution of the

station	position	Depth (m) obs.	mod.	Tidal const	Model Harmonic constants $\overline{u}_o(cm/s)$	$\delta_{\overline{u}}(deg.)$	$\overline{v}_o(cm/s)$	$\delta_{\overline{v}}(deg.)$
N	72°00.0'N	328	308	M_2	12.2	61.0	6.1	243.1
	31°00.0'E			K_1	2.0	212.4	0.9	15.5
A	73°50.0'N	300	312	M_2	13.2	40.6	6.8	312.1
	20°00.0'E			K_1	4.5	228.7	2.0	80.0
B9	75°00.2'N	193	200	M_2	9.6	56.6	5.2	310.7
	34°57.4'E			K_1	1.0	95.0	1.5	198.0
B1	74°58.8'N	44	70	M_2	53.9	48.0	45.0	313.8
	20°03.8'E			K_1	17.8	128.6	19.3	37.6

Table 3: *Model data from the depth integrated model for the stations which have current measurements under a free ocean surface.*

station	position	Depth (m) obs.	mod.	Tidal const	Model Harmonic constants $\overline{u}_o(cm/s)$	$\delta_{\overline{u}}(deg.)$	$\overline{v}_o(cm/s)$	$\delta_{\overline{v}}(deg.)$
S2	75°34.0'N	87	96	M_2	26.5	49.3	17.0	319.4
	23°26.4'E			K_1	6.5	143.7	6.5	70.0
S3	75°20.0'N	157	155	M_2	16.2	51.8	7.0	330.2
	24°59.4'E			K_1	3.2	160.3	1.3	68.5
S4	75°02.0'N	281	290	M_2	10.1	57.8	2.2	10.9
	27°06.9'E			K_1	1.8	194.2	0.6	253.2
S5	74°51.2'N	366	368	M_2	8.4	61.0	1.4	35.8
	28°43.3'E			K_1	1.5	211.3	0.8	257.3

Table 4: *Model data from the depth integrated model for the stations which have current measurements under an ice covered ocean surface.*

eigenvalue problem (43) is described in section 3.3. The different eddy viscosity profiles ($\phi(s)$) used in the following calculations are shown in figure 1, and the value of ν_o is determined such that (107) is fulfilled. The tidal current profile examples presented here do not include a time varying eddy viscosity, which would be an important mechanism in generating higher harmonics in shallow tidal seas (Davies, 1990b).
In the section 5.1 we will discuss some examples where we have computed the tidal current profiles for the M_2 and K_1 constituents at positions where we have observations under a free ocean surface. The current profile obtained under an ice covered ocean surface will be presented in section 5.2.

5.1. Tidal current profiles under a free ocean surface

Figure 21 shows the computed current profiles for the M_2 tide at station N (Nordkappbanken) for various eddy viscosity profiles. The boundary conditions used are a free slip sea surface by eq. (84) and a no-slip at sea bed by eq. (82) with $a_b = 1$. The input mean current harmonic constants are given in table 3 and the corresponding ellipse parameters are presented by a straight line in the figures. The $\times$ indicate observed data. For the constant eddy viscosity profile (fig.1a) we have $\phi(s) = \phi_o = 1$ and by (107) ν_o is 93 cm^2/s. In the linear eddy viscosity profile (fig1c) $\phi_o = 0.001$ and $\phi_1 = 1$. In this case ν_o was found to be 6220 cm^2/s in order to maintain the depth mean current set by the requirement (107). The current profiles computed

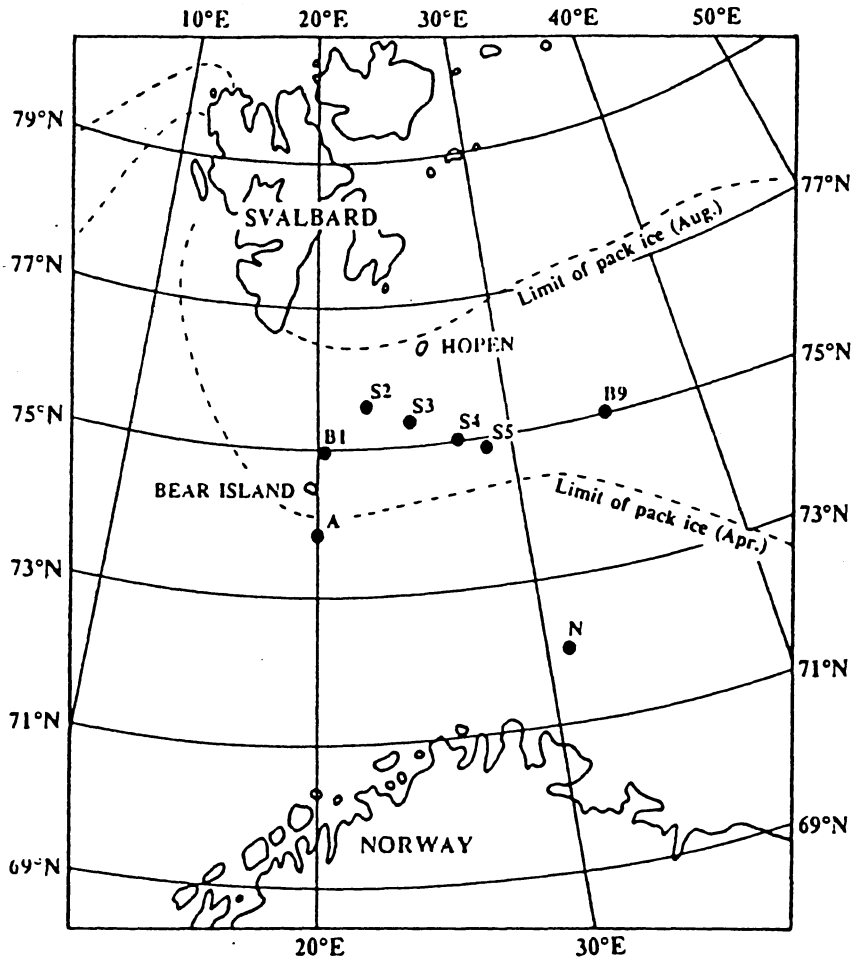

Figure 20: *The location of the stations where we have current observation data.* ***N***, ***A***, ***B9*** *and* ***B1*** *have current observations under a free ocean surface.* ***S2***, ***S3***, ***S4*** *and* ***S5*** *have current observations under an ice covered ocean surface.*

with a bottom layer eddy viscosity profile (fig1 b) we have chosen $\phi_o = 0.001$ and $\phi_o = 1$ and the thickness of the friction layer is $d_o \cdot h = 0.1 \cdot 328$m. The friction layer being about a tenth of the total water depth which is chosen to be in accordance with what Bowden et al. (1959) suggested for a water depth of about 30 m in the Irish sea. Here ν_o is 760 cm^2/s. The linear eddy viscosity profile (fig.1c) may be considered as a special case of this bottom layer eddy viscosity profile with $d_o = 1.0$ equal the total water depth.

In all these three profile examples at Nordkappbanken the M_2 tidal current ellipse changes direction of rotation when approaching the near bed region. This is also the case for the observed current ellipse. A similar change of direction of rotation of the current ellipse is obtained by Davies (1986) in a model covering the North Sea and are confirmed with observations at three different stations.
Even though the computed major and minor semi axis and the azimuth orientation of the current ellipse (fig.21 a, b and c) do not fit to the observed ones, the eccentricity i.e. the ratio minor to major semi axis (fig.21d), agree very well with the observations. We also note that the eccentricity is not sensitive to variations of eddy viscosity profiles.

Figure 22 shows the K_1 current ellipse profiles at the same station, Nordkappbanken, computed with the constant and linear eddy viscosity profiles. As a consequence of the constraint (107) the magnitude of ν_o is 12 and 1450 m^2/s for the constant and linear eddy viscosity profiles respectively. The current profiles differ only in the near bed region i.e. inside the bottom boundary layer, and above this region the profiles are equal and constant with depth. The current profiles are sensitive to the different eddy viscosity models inside the boundary layer and outside the current are independent of depth equal to the depth mean current from the depth integrated model. Again we see that the eccentricity (fig.22d) are about constant and match the observed one very well, even though the major and minor semi axis (fig.22a,b) do not. As distinct from the M_2 current ellipses, the K_1 ellipses do not change direction of rotation when approaching the near bed region, even for the computed nor for the observed current ellipses.
Comparing the profiles for the M_2 and the K_1 constituents it is clearly seen that the M_2 current ellipses depend more strongly on the changes of the eddy profiles. In other words, we see that the vertical distribution of the M_2 current ellipse parameters are more sensitive to variations in the eddy profile than the K_1 ellipse parameters. Nordkappbanken is located in the Barents sea where we are close to the M_2 critical latitude and far from the K_1 critical latitude. In view of the results of the parameters dependency study in section 6.5.1. this may explain why the current profiles are more sensitive to viscous effects and varies more with depth. Similar results are obtained by Foldvik et al. (1990) who have investigated the tides of the southern Weddel Sea, which includes the M_2 critical latitude in the southern hemisphere and the M_2 velocity profile becomes strongly depth dependent at this latitude.
The boundary layer thickness Δ_-, defined in (91) are 260 m and 20 m for the M_2 and the K_1 current profiles respectively computed with a constant eddy viscosity ($\nu = \nu_o$). Δ_- are less than the total water depth for both constituents, but for the K_1 tide Δ_- is a thin layer near the bottom and for the M_2 tide Δ_- occupy $\frac{4}{5}$ of the water depth.

At Nordkappbanken (station N) the water depth are 328 m. We shall now compute current profiles at other stations with shallower water and and which are located even closer to the M_2 critical latitude and see if we can call attention to the same properties of the current

ellipses as pointed out at Nordkappbanken.

At station A with a water depth of 300 m and located closer to the M_2 critical latitude, the M_2 and K_1 current profiles are shown in figure 23 and 24 respectively. The current profiles are computed with the same eddy viscosity profiles as used in the profiles calculation at Nordkappbanken. For the constant eddy viscosity ν_o is 414 cm^2/s and 13 cm^2/s for the M_2 and K_1 constituents respectively, which gives the boundary layer thickness, Δ_- to be equal to 993 m and 11 m. Here we see that Δ_- exceeds the water depth for M_2, while for K_1 Δ_- is only $\frac{4}{100}$ of the total water depth. For the linear eddy viscosity profile ν_o is 6680 cm^2/s and 2600 cm^2/s for the M_2 and K_1 respectively. Even though the water depth and the M_2 current velocity have approximately the same value at station A and N, the current ellipse parameters depends more on the choice of eddy profiles than at station N. The observed M_2 current ellipse changes direction of rotation at point of measurement near sea bed. The current ellipses computed with a constant eddy viscosity reproduce this, but not the current ellipses computed with a linear or a layered eddy profile. In order to match the computed parameters to the observed, one should apply a layered eddy profile (fig.1b) with a smaller d_o.

As we can see, the observed current has a more complex vertical structure near the sea surface than the computed. Wind may have caused larger mixing in the surface layer and influenced the observations, while wind effects are neglected in the model where the motion is purely tidal driven. Density stratification effects may also have influenced the observations.

We have also chosen to present current profiles at the stations B9 and B1, both located close to the M_2 - critical latitude. The water depth at B9 and B1 is 44 m and 193 m respectively. The current profiles at these two stations are computed with a constant and linear eddy viscosity profile. The M_2 and K_1 current profiles at station B9 are shown in figure 25 and 26 respectively. There are only three depths where there exists observation data and none close to the sea bed. For the constant eddy viscosity ν_o is 210 cm^2/s and 18 cm^2/s for the M_2 and K_1 constituents respectively, which gives the analogous Ekman boundary layer, Δ_- to be equal to 9500 m and 23 m. This is about the same situation at station A where Δ_- exceeds the water depth for M_2, while for K_1 Δ_- is a thin region near the sea bed . For the linear eddy viscosity profile ν_o is 3180 cm^2/s and 5000 cm^2/s for the M_2 and K_1 respectively. The M_2 and K_1 current profiles at station B1 are shown in figure 27 and 28 respectively. Here there are only two depths where we have observation data and none close to the sea bed. At this station we have very strong tidal current and very shallow water. For the constant eddy viscosity ν_o is 310 cm^2/s and 170 cm^2/s for the M_2 and K_1 constituents respectively, which gives the analogous Ekman boundary layer, Δ_- to be equal to 3700 m and 70 m. For the linear eddy viscosity profile ν_o is 4670 cm^2/s and 4800 cm^2/s for the M_2 and K_1 respectively. Here at B1 the Δ_- exceeds the water depth for the M_2 and for the K_1 constituent. And we observe that the M_2 and the K_1 current ellipse parameters have a similar depth distribution. The eccentricity is about constant in depth.

The choice of eddy viscosity at sea surface and sea bed at the stations N, A, B9 and B1 are summarized in table 5. In section 2.3. the eddy viscosity values at sea bed is given in the range $0.02 - 2.0$ cm^2/s and above the friction layer to be $500 - 2000$ cm^2/s. This agrees very well with the sea bed and surface values obtained in the current profile examples with the layered eddy viscosity profile, and generally we conclude that the eddy viscosity values

Station	Tidal const.	Eddy viscosity profile $\nu(z)$ (cm^2/s)					
		fig.1a $\phi_o = 1$ *ie.* $\nu = \nu_o$		fig.1b $\phi_o = 1, \phi_1 = 0.001, d_o = 0.1$		fig.1c $\phi_o = 1, \phi_1 = 0.001$	
		ν_o	Δ_- / depth	$\nu(0)$	$\nu(-h)$	$\nu(0)$	$\nu(-h)$
N	M_2	93	260/328	760	0.76	6220	6.2
	K_1	12.2	20/328	–	–	1450	1.4
A	M_2	414	990/300	930	0.93	6680	6.7
	K_1	13	11/300	–	–	2600	2.6
B9	M_2	210	9500/193	–	–	3180	3.2
	K_1	180	23/193	–	–	5000	5.0
B1	M_2	310	3700/44	–	–	4665	4.7
	K_1	170	70/44	–	–	4800	4.8

Table 5: *The surface ($\nu(0)$) and the bed ($\nu(-h)$) eddy viscosity value which gives the input depth mean current for the different computed current profiles. For the constant eddy viscosity profile for which the boundary layer thickness (Δ_-) is defined (91), Δ_- relative to the total water depth is given in the table.*

obtained represent reasonable estimates.

The consistency requirements for the method is described in section 4.4.2. The current profiles represented in section 5.1 have the same depth mean current as the depth mean current from the depth integrated model because the value of ν_o determined by (107). The second consistency requirement concerns the shear stresses where we require coinciding surface and bed stresses from the depth integrated model and from the current profile calculations.
The current profile examples presented in section 5.1 are computed at stations where we have a free ocean surface, and the surface boundary condition is zero surface shear stress. In the figures 21–28e show the depth distribution of the shear stresses, we see that the surface value is zero i.e. coinciding surface shear stresses is fulfilled for the M_2 and K_1 constituents at all the stations N, A, B9 and B1.
Concerning the bed stress, a quadratic friction law (17) is used in the depth integrated model for the M_2 constituent. Since the system is not linear the current profiles should have been computed with use of the time dependent method described in section 3. A convolution integral (50) must then be evaluated for every time step. And to proceed one may calculate the current harmonic constants (or ellipse parameters) from the derived time series. In stead of implementing this procedure for the M_2 current profile calculation, we have used a linear friction law (18) with $u_s = \sqrt{\overline{u}_o^2 + \overline{v}_o^2}$. It is expected that this approximation have a minor influence on the current profile.
The rotary components of the complex bed shear stresses from the the depth integrated model are indicated by an asterix at sea bed in the figures 21–28e and f.
For the M_2 constituent at the various stations we have a fairly good agreement between the shear stresses from the depth integrated model and the bed stresses from the current profile calculation for the cyclonic components of the shear stresses ($|T_+|$, fig.21f, 23f, 25f, 27f). While the anticyclonic component ($|T_+|$, fig.21e, 23e, 25e, 27e) gives best consistency in the examples where the eddy viscosity profile decreases to a smaller value near the sea bed. The current profiles computed with a constant viscosity gives a too large value for the bed stress. For the K_1 tide in the depth integrated model it is used a linear friction law (18) with

$c_f = 3.0 \cdot 10^{-3}$ and $u_s = 0.75$ m/s and the rotary components of the shear stresses are easily evaluated. The K_1 current profile calculations give too small values for the bed stresses in comparison with the bed stresses from the depth integrated model for both the cyclonic and anticyclonic rotary stress components at all the stations (fig.22, 24, 26, 28 e and f). The high value of u_s used in the linear friction law may be a reason that the bed stresses from the depth integrated model is so high. The 'typical' velocity scale u_s for the K_1 tide at the stations we have considered have a maximum current in the range $0.02 - 0.2$ m/s which would have given a smaller value of the bed stress from the depth integrated model.
Applying other eddy viscosity profiles will also affect the bed conditions in the profile calculations, and also applying other boundary conditions at sea bed i.e. a slip condition $a_b < 1$ in eq. (21) will also have influence on the current characteristics at the sea bed, and hopefully better bed stress consistency.

5.2. Tidal current profiles under an ice covered ocean surface

When the ocean is ice covered, there will in addition to the bed boundary layer, also exist a boundary layer near the sea surface. The motion in this boundary layer is dominated by the friction between the ice and the water, and which further will depend upon the condition of ice we have and the velocity of the ice relative to the ocean water. In the calculations presented below we have assumed that the ice is at rest and that we have a no-slip boundary condition between the the sea water and the ice ($R_{\pm}^{ice} = 0$ and $a_s = 1$ in eq. (83)). The boundary condition at the sea bed is the same as in the profile calculations under a free ocean surface (sec 7.1.) i.e. $a_b = 1$ in (82).
The stations S2 - S5 where we have the current observations, are all located near the M_2 critical latitude (fig.20) and the influence of eddy viscosity upon the M_2 current profiles is expected to be large compared to what is the case for the K_1 tide. We have therefore chosen to present only the current profile calculations for the M_2 constituent in this section. We have computed the current profiles with a constant eddy viscosity at all the stations S2 - S5, which because of the symmetry on the boundary conditions (no-slip at sea bed and surface) gives current profiles that are symmetric around mid depth. With these boundary conditions the computed current profile will be symmetric around mid depth if a symmetric eddy viscosity profile is applied. Further, with the constant eddy viscosity as a starting point, we have constructed a simple eddy viscosity profile for each station which reproduce the main properties of the observed current profile.

Figure 29 shows the M_2 current profiles at station S2 where the water depth are 87 meters. The full drawn line in figure 29 gives the calculations with a constant eddy viscosity and by (107) $\nu_o = 87.8$ cm^2/s. In the profiles calculations in section 5.1. we had only one boundary layer near the sea bed and the eddy viscosity profile was constructed with a linear increase with distance above sea bed. Here we have a boundary layer at sea surface too and have therefore chosen an eddy viscosity profile with a bed and surface friction layer with a linear increase with distance from the boundary (fig1d) where of course the choice of the parameters ϕ_o, ϕ_1, ϕ_2, d_o and d_1 will influence final current profiles. The current profile calculations presented by a dotted line in figure 29 is computed with this two layer eddy viscosity profile (fig1d) with $\phi_o = \phi_2 = 0.001$, $\phi_o = 1$, $d_o = 0.05h$ and $d_1 = 0.2h$ and by (107) $\nu_o = 283.6$ cm^2/s. This eddy viscosity gives a computed depth distribution of the maximum (A, fig.29a) and the minimum (B, fig.29b) current velocity decreasing with depth, similar as for the ob-

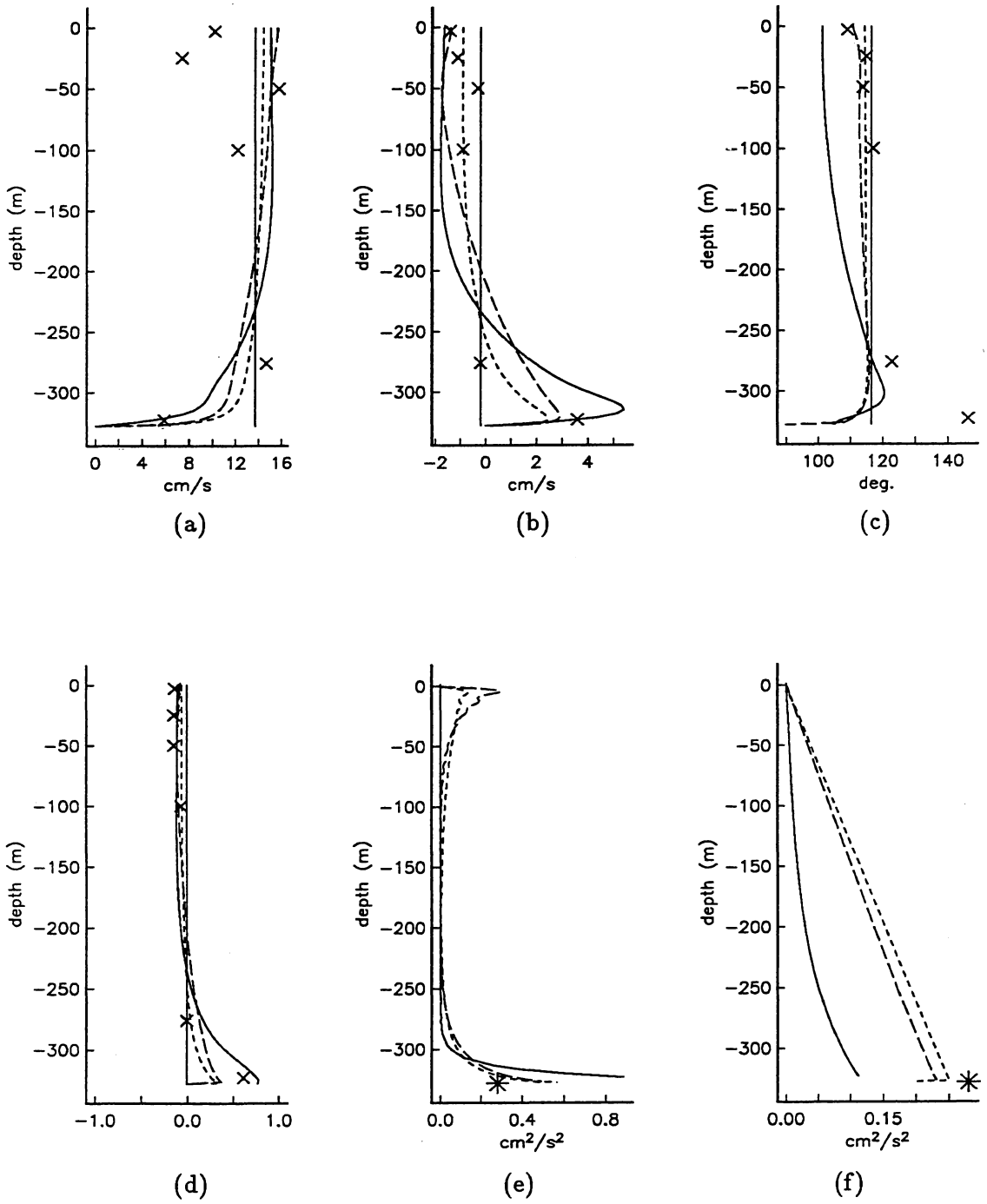

Figure 21: *Computed M_2 tidal current profiles at station N (Nordkappbanken 72°N 31°E), water depth 328 m, for various eddy viscosity profiles; (———), (— — —) and (- - - -) fig.1a, b and c respectively. (a) A major semi axis, (b) B minor semi axis, (c) θ azimuth orientation, (d) B/A eccentricity, (e) $|T_+|/\rho$ shear stress and (d) $|T_-|/\rho$ shear stress. × indicate the observed current data, the straight line represent the depth mean values and * is the stress from the depth integrated model.*

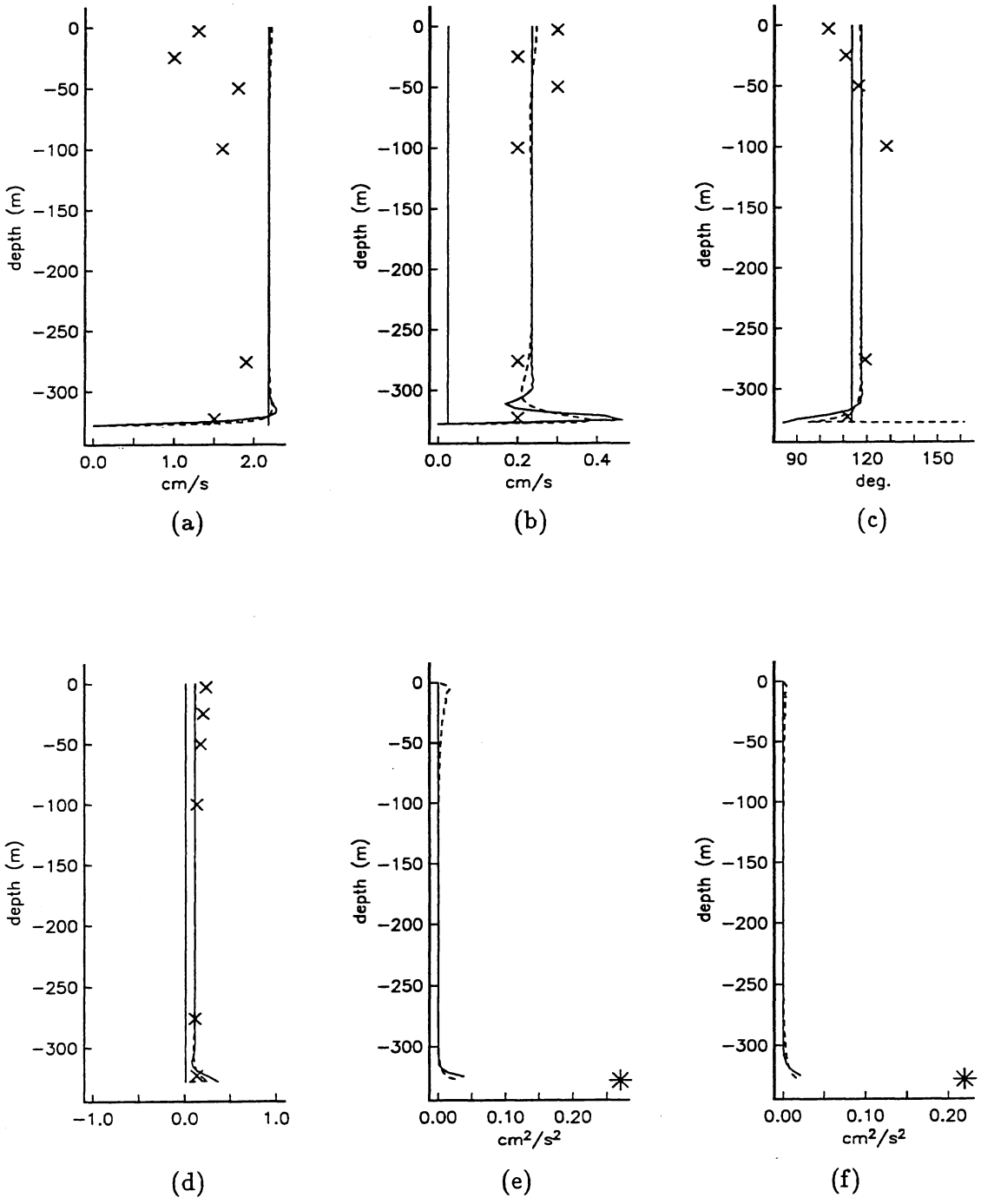

Figure 22: *Computed K_1 tidal current profiles at station N (Nordkappbanken 72°N 31°E), water depth 328 m, for various eddy viscosity profiles; (———) and (- - - -) fig.1a and c respectively. (a) A major semi axis, (b) B minor semi axis, (c) θ azimuth orientation, (d) B/A eccentricity, (e) $|T_+|/\rho$ shear stress and (d) $|T_-|/\rho$ shear stress. × indicate the observed current data, the straight line represent the depth mean values and * is the bed stress from the depth integrated model.*

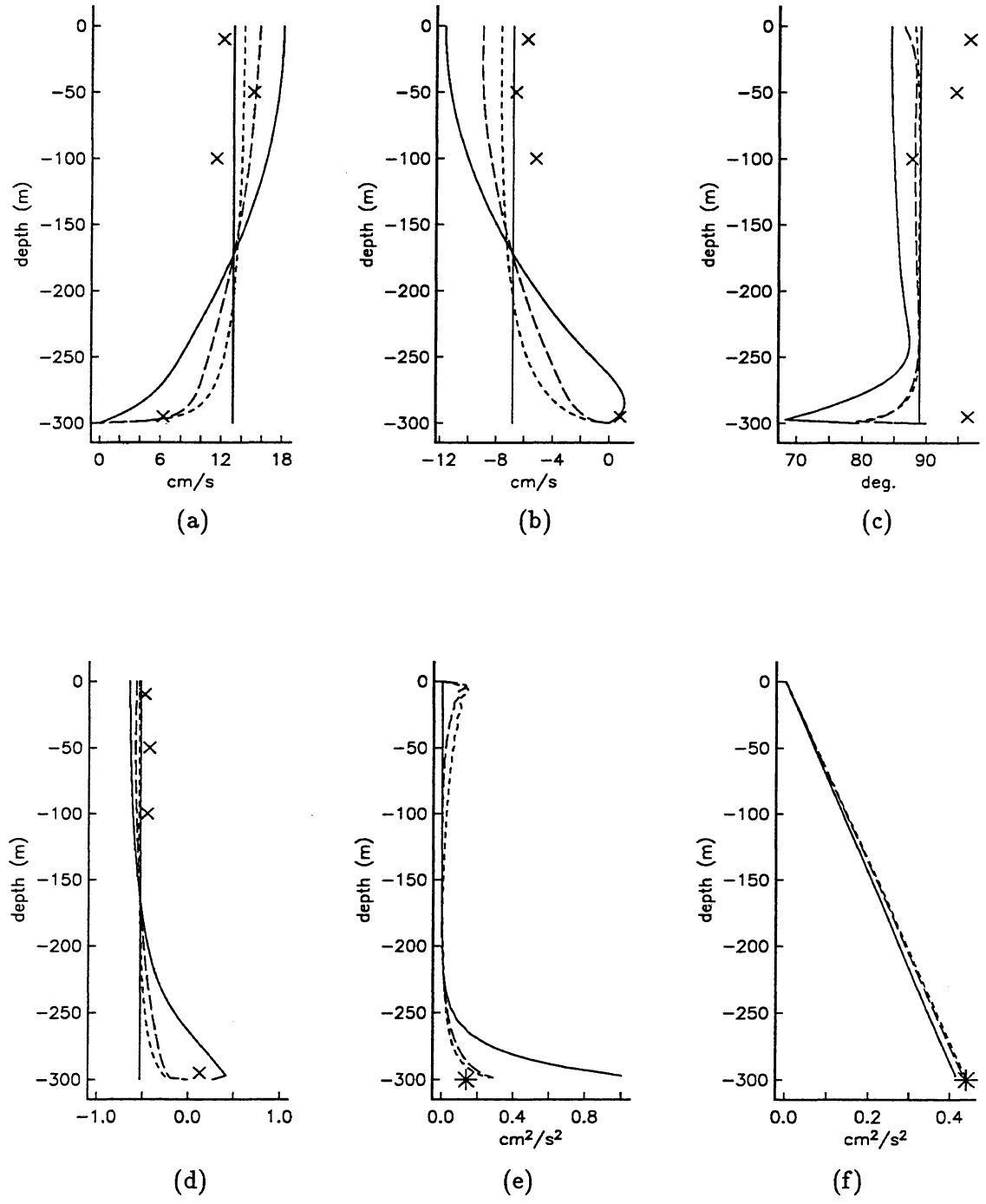

Figure 23: *Computed M_2 tidal current profiles at station A (73°50'N 20°E), water depth 300 m, for various eddy viscosity profiles; (———), (— — —) and (- - - -) fig.1a, b and c respectively. (a) A major semi axis, (b) B minor semi axis, (c) θ azimuth orientation, (d) B/A eccentricity, (e) $|T_+|/\rho$ shear stress and (d) $|T_-|/\rho$ shear stress. × indicate the observed current data, the straight line represent the depth mean values and * is the bed stress from the depth integrated model.*

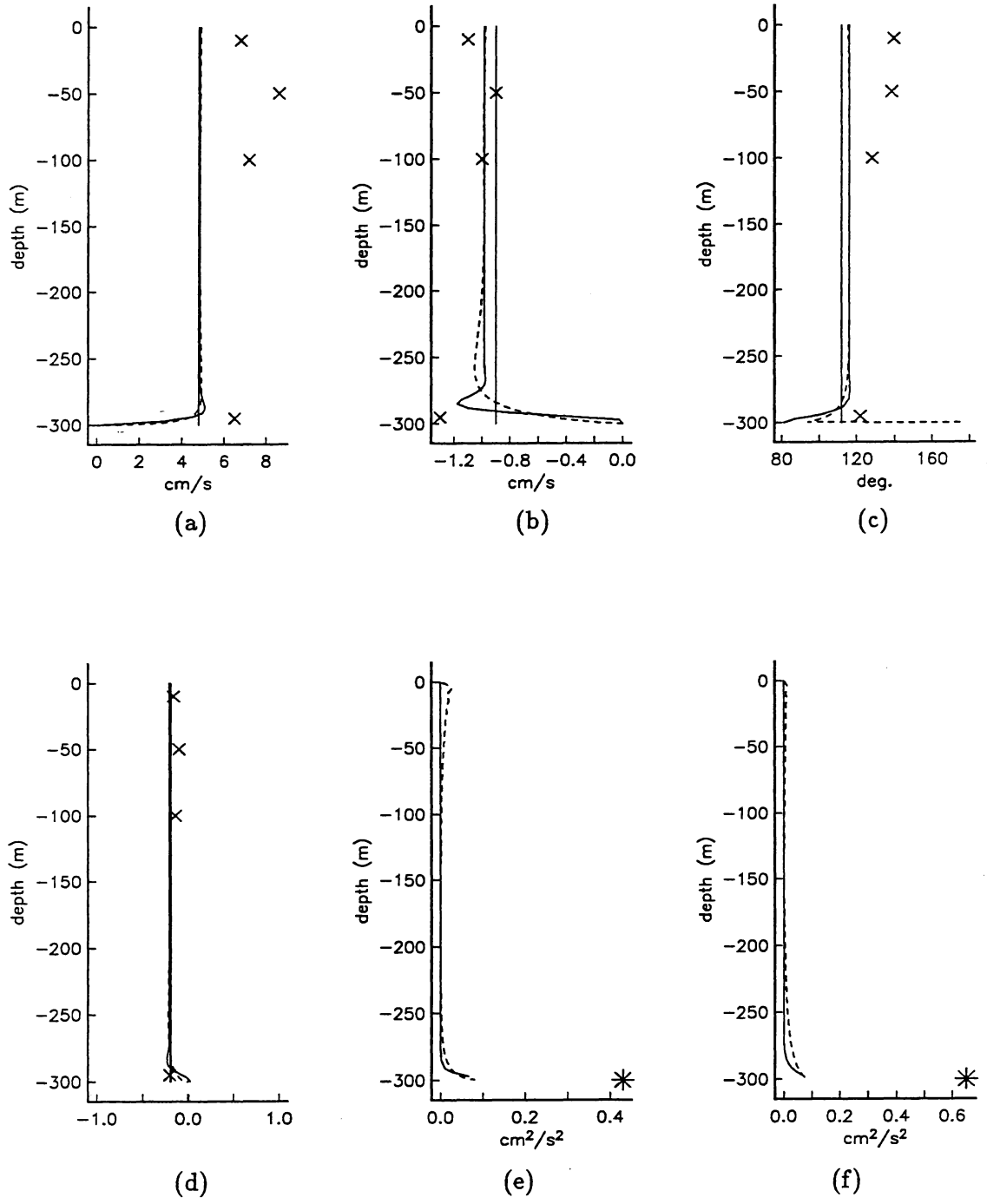

Figure 24: *Computed K_1 tidal current profiles at station A (73°50'N 20°E), water depth 300 m, for two eddy viscosity profiles; (———) and (- - - -) fig.1a and c respectively. (a) A major semi axis, (b) B minor semi axis, (c) θ azimuth orientation, (d) B/A eccentricity, (e) $|T_+|/\rho$ shear stress and (d) $|T_-|/\rho$ shear stress. × indicate the observed current data, the straight line represent the depth mean values and * is the bed stress from the depth integrated model.*

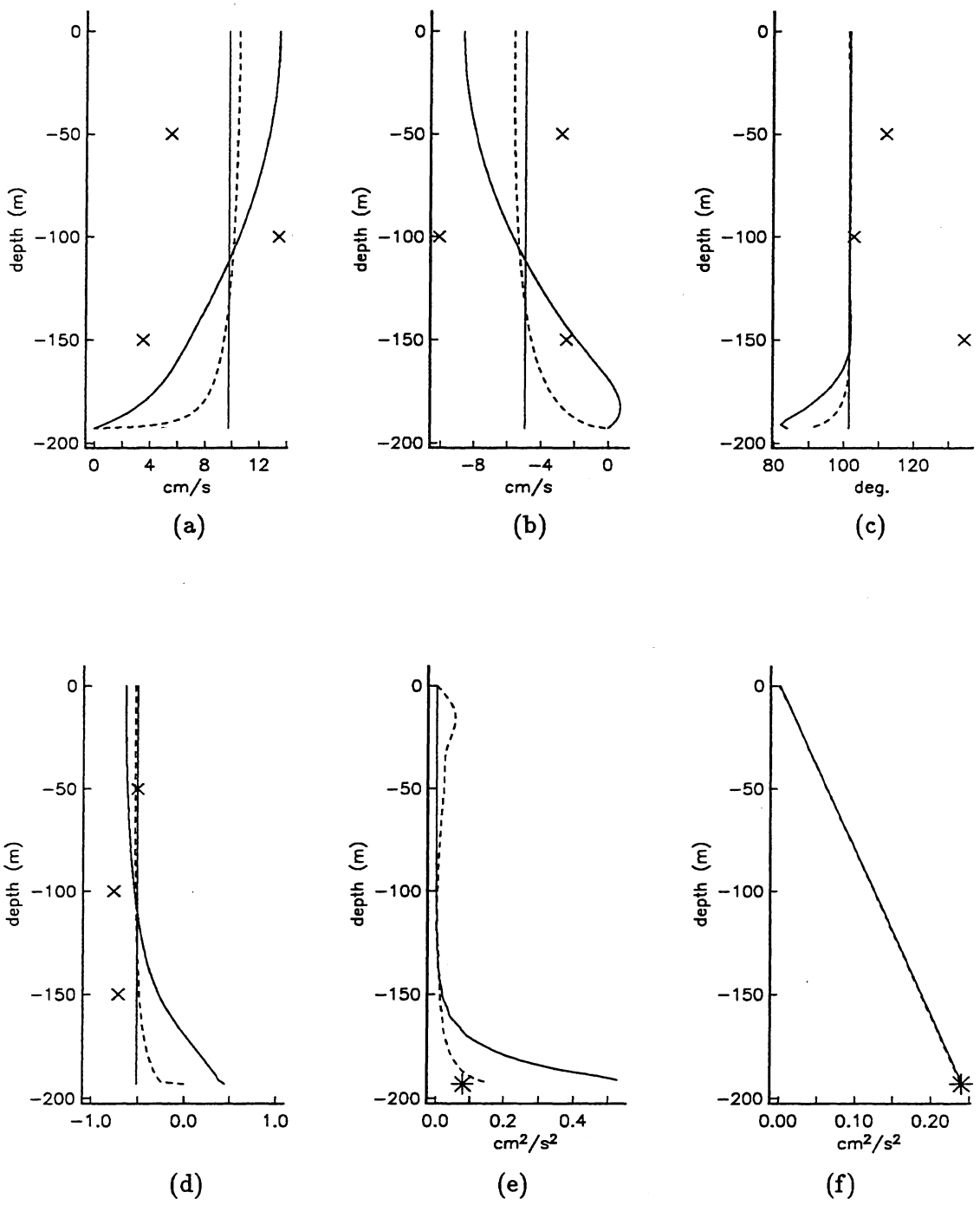

Figure 25: *Computed M_2 tidal current profiles at station B9 (75°0.2'N 34°57.4'E), water depth 193 m, for two eddy viscosity profiles; (———) and (- - - -) fig.1a and c respectively. (a) A major semi axis, (b) B minor semi axis, (c) θ azimuth orientation, (d) B/A eccentricity, (e) $|T_+|/\rho$ shear stress and (d) $|T_-|/\rho$ shear stress. × indicate the observed current data, the straight line represent the depth mean values and $*$ is the bed stress from the depth integrated model.*

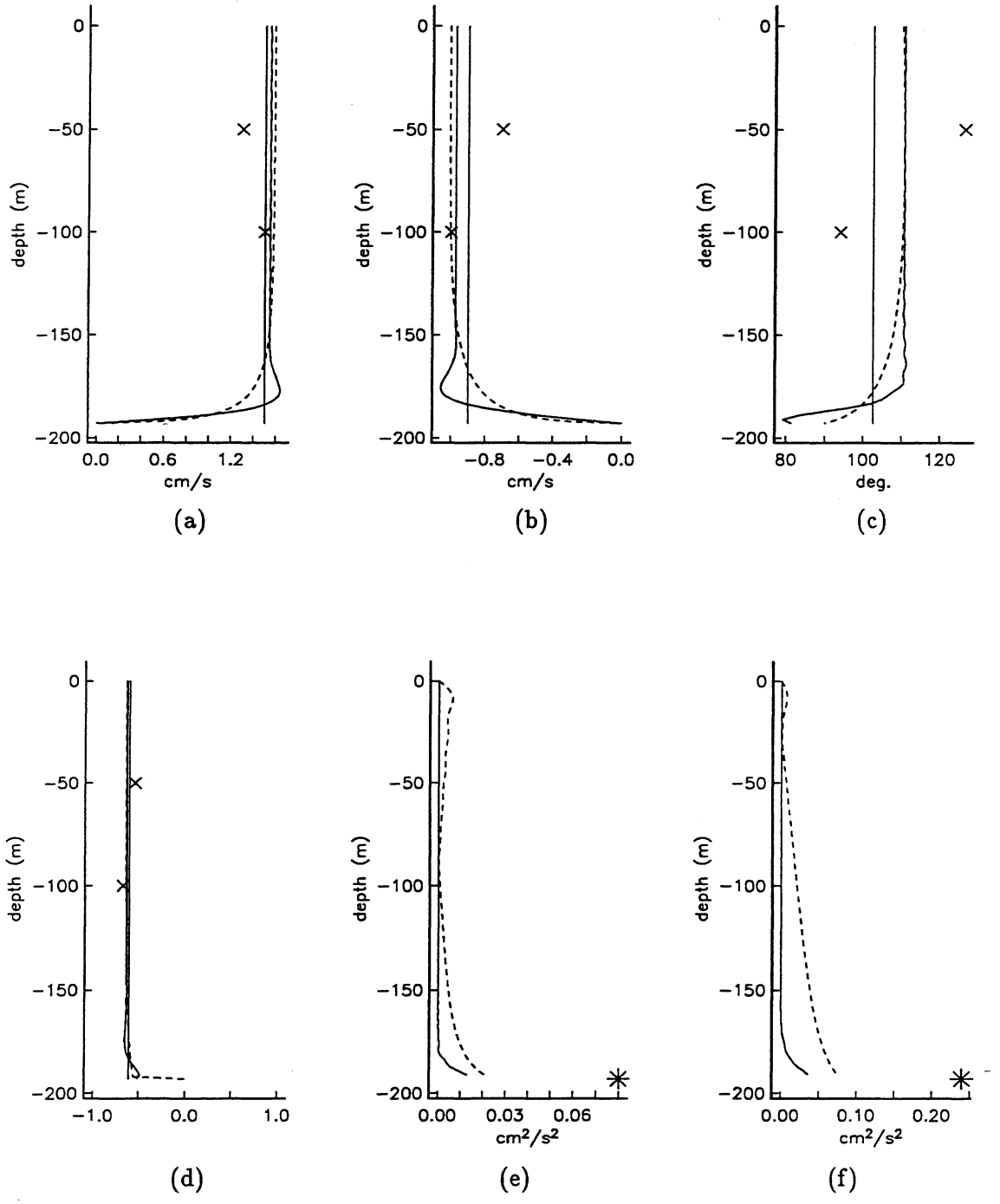

Figure 26: *Computed K_1 tidal current profiles at station B9 (75°0.2'N 34°57.4'E), water depth 193 m, for two eddy viscosity profiles; (———) and (- - - -) fig.1a and c respectively. (a) A major semi axis, (b) B minor semi axis, (c) θ azimuth orientation, (d) B/A eccentricity, (e) $|T_+|/\rho$ shear stress and (d) $|T_-|/\rho$ shear stress. × indicate the observed current data, the straight line represent the depth mean values and * is the bed stress from the depth integrated model.*

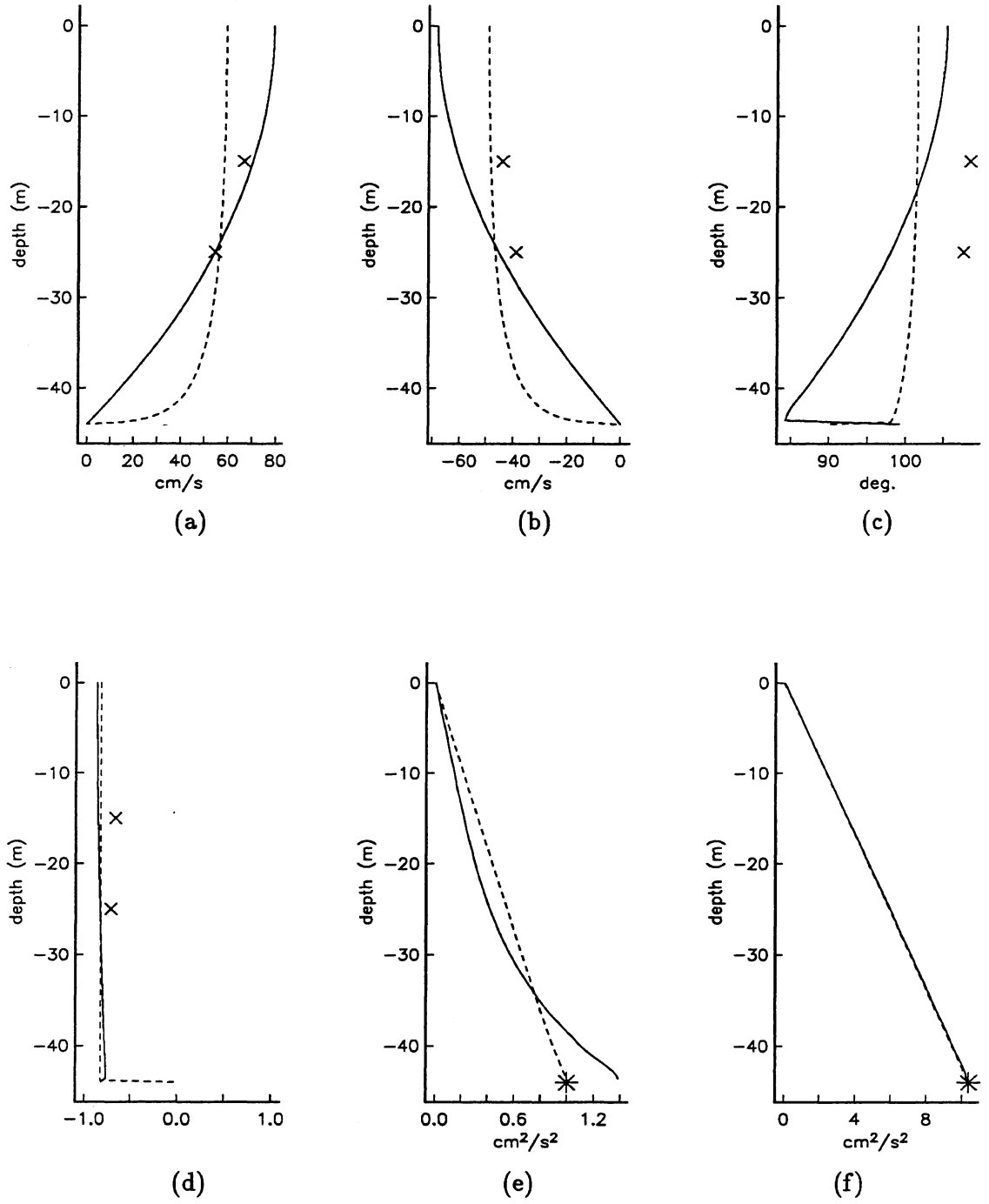

Figure 27: *Computed M_2 tidal current profiles at station B1 (74°58.8'N 20°3.8'E), water depth 44 m, for two eddy viscosity profiles; (———) and (- - - -) fig.1a and c respectively. (a) A major semi axis, (b) B minor semi axis, (c) θ azimuth orientation, (d) B/A eccentricity, (e) $|T_+|/\rho$ shear stress and (d) $|T_-|/\rho$ shear stress. × indicate the observed current data, the straight line represent the depth mean values and * is the bed stress from the depth integrated model.*

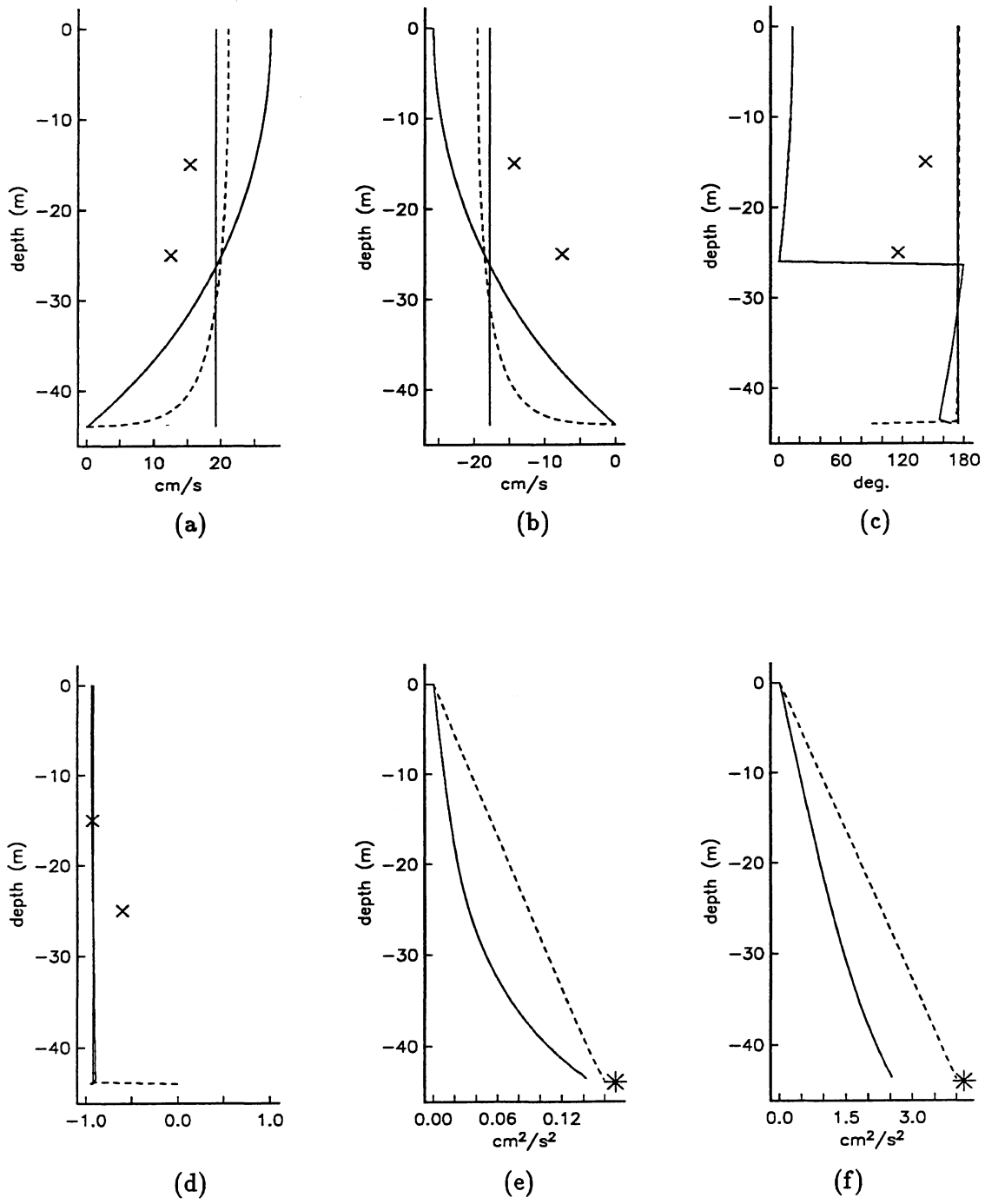

Figure 28: *Computed K_1 tidal current profiles at station B1 (74°58.8'N 20°3.8'E), water depth 44 m, for two eddy viscosity profiles; (———) and (- - - -) fig.1a and c respectively. (a) A major semi axis, (b) B minor semi axis, (c) θ azimuth orientation, (d) B/A eccentricity, (e) $|T_+|/\rho$ shear stress and (d) $|T_-|/\rho$ shear stress. × indicate the observed current data, the straight line represent the depth mean values and ∗ is the bed stress from the depth integrated model.*

served current. Especially for the eccentricity (ε, fig.29d) we have very good agreement with the observations. Figure 30 shows the M_2 current profiles at station S3 where the water depth are 157 meters. In the current profile calculations the same eddy viscosity profiles as used at station S2, is applied and by (107) $\nu_o = 87.3$ cm^2/s and $\nu_o = 283.0$ cm^2/s for the constant and the two layer eddy viscosity profile respectively. We have similar situations at these two stations, the water depth are relative shallow (compared with S4 and S5), the maximum current velocity is quite large (16-26cm/s), the observed currents decrease with depth and the values of ν_o for the different current profile calculations with equal eddy viscosity distribution at S2 and S3 differ only by some decimals of a cm^2/s.

At the next two stations S4 and S5, the water depth are 281 and 366 meters respectively, and the maximum current velocity is 8-10 cm/s. The observed current increases with depth and reaches a maximum below mid depth and the observed current ellipse changes direction of rotation in the near bed region. At S5 the observation point near the sea bed is missing, which may have documented the calculated change of direction of rotation of the current ellipse. Because the mooring for S5 was discovered at drift, all the current meters except for the one nearest the sea floor were recovered. But since station S5 as at the stations N, A and S4 have similar conditions i.e. deep water, relative weak current velocity and are located close to the critical latitude, it is probable that the observed current ellipse change direction of rotation at S5 too.
The M_2 current profiles at station S4 are shown in figure 31 and in the current calculations a constant eddy viscosity is applied and by (107) we obtain $\nu_o = 94.8$ cm^2/s and for the two layered eddy viscosity profile (fig.1d) with $\phi_o = \phi_2 = 0.001$, $\phi_o = 1$, $d_o = 0.2h$, $d_1 = 0.05h$ we have $\nu_o = 309.0$ cm^2/s by (107). Here we have chosen the viscosity layer thicker at the sea bed than at the surface ($d_o > d_1$). This gives a depth distribution of the maximum current velocity (A, fig.31a) which is increasing with depth and which is reaching a maximum below mid depth, in accordance with the observations at this station. Both eddy viscosity profiles reproduce the change of direction of rotation of the current ellipse near the sea bed, but we see from the eccentricity (ε, fig.31d) and the minimum current velocity (B, fig.31b) that the computed current ellipse changes direction of rotation at sea surface too, while this is not the case for the observed current. A way to obtain the observed result might be to choose different value of the eddy viscosity at sea bed and sea surface. We have a similar situation at S5 where the current profiles showed in figure 32 are computed with the same eddy viscosity profiles. This gives by (107) $\nu_o = 98.5$ cm^2/s and $\nu_o = 322.5$ cm^2/s for the constant and the two layered eddy viscosity profile respectively.

The current profile for the stations presented above may be classified in two groups S2, S3 and S4, S5.
Firstly, at S2 and S3 the current velocity are quite strong and the water depth are relative shallow. The observed current shows a decreasing effect with depth and the current ellipse is rotating cyclonic at all depth. At S3 where we have the deepest water of these two stations, the minimum current velocity (B, fig.30b) is very close to zero at the sea bed i.e. almost changing direction. The main properties of this current picture are reproduced with an eddy viscosity profile showed in fig.1d with $d_o < d_1$, as described above, which gives a higher velocity gradient at sea surface than at sea bed. Concerning the consistency of these computations, described in section 4.4.2. for the general case, the depth mean current from the depth integrated model is the same as for the current profiles since the value of ν_o is determined

such that (107) is fulfilled i.e. a constraint in the computation procedure. Furthermore, the bed and surface shear stresses from the resulting current profiles shall equal the stresses from the depth integrated model. The bed stresses from the depth integrated model are as described in section 5.1. and showed with an asterix (*) at sea bed in the figure 29 - 30 e and f. The shear stresses from the current profiles computed with an eddy viscosity of the form in figure 1d, give a bed value in quite good agreement with the bed stress from the depth integrated model, and this is the same as found in the current profile examples in section 5.1. The surface shear stresses due to the ice covered ocean surface are actually not taken into account in the depth integrated model. But here in these current profile calculations we have given the shear stresses from the depth integrated model a value by using a linear friction law with $u_s = \sqrt{\overline{u}_o^2 + \overline{v}_o^2}$ and $c_{fi} = 1.0\,10^{-3}$ i.e. one third of the drag coefficient at sea bed. The modulus of the resulting rotary components of the complex surface shear stress are marked with an asterix (*) at the sea surface in figure 29 - 30 e and f. The shear stresses in fig.29-30 e and f presented by a stippled line show that the modulus of the shear stresses is less at sea surface than at sea bed which is also the case for the shear stresses from the depth integrated model. And we see that for both the surface and bed stresses the computations with an eddy viscosity distribution near the boundaries which are increasing with distance from the boundary, seems to fulfill the consistency requirement best.

The second current profile group is the stations S4 and S5. Here the water depth is deeper and the current velocity weaker. The observed current shows an increasing effect with depth which reaches a maximum below mid depth and the current ellipse changes direction of rotation in the near bed region. These main properties of the current picture are reproduced with an eddy viscosity of the form given in fig.1d with $d_o > d_1$, as described earlier. The shear stresses (fig.31-32 e and f, stippled line) derived from the current profiles computed with this eddy viscosity profile give a higher surface value than the bed value. This is the opposite of the situation for the bed and surface stresses from the depth integrated model. So, the consistency requirements concerning the shear stresses are not very good maintained at these two stations. To improve this (and to improve the agreement with the observations in the near surface region) a more detailed testing of different eddy viscosity profiles for example with eddy viscosity surface value not equal to the bed value ($\phi_o \neq \phi_2$) and also different boundary conditions ($a_b, a_s < 1$, i.e. slip boundary conditions) are needed.

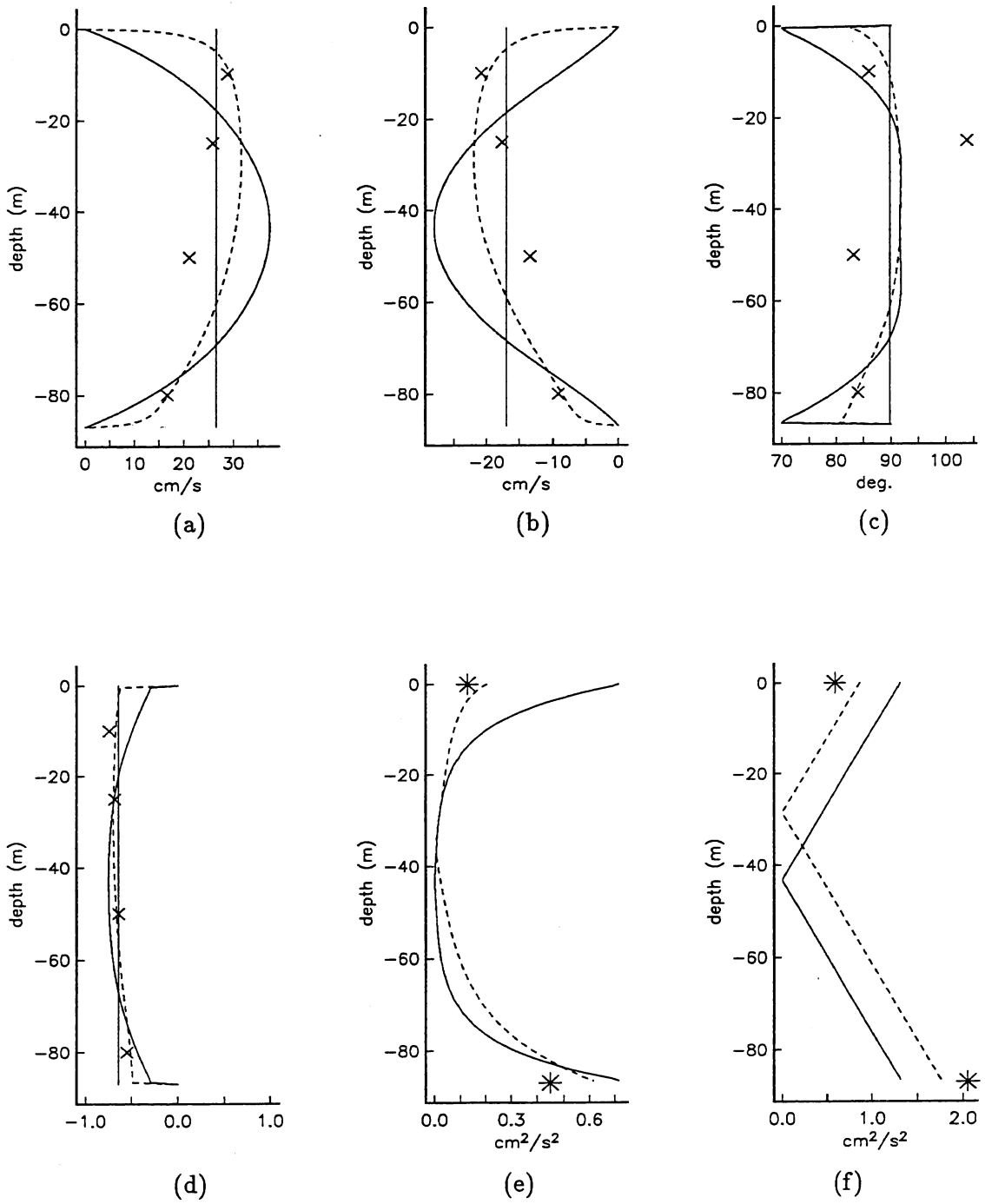

Figure 29: *Computed M_2 tidal current profiles at station S2 (75°34'N 23°26.4'E), water depth 87 m, for two eddy viscosity profiles; (———) and (- - - -) fig.1a and d respectively. (a) A major semi axis, (b) B minor semi axis, (c) θ azimuth orientation, (d) B/A eccentricity, (e) $|T_+|/\rho$ shear stress and (d) $|T_-|/\rho$ shear stress. × indicate the observed current data, the straight line represent the depth mean values and ∗ is the bed and surface stresses from the depth integrated model.*

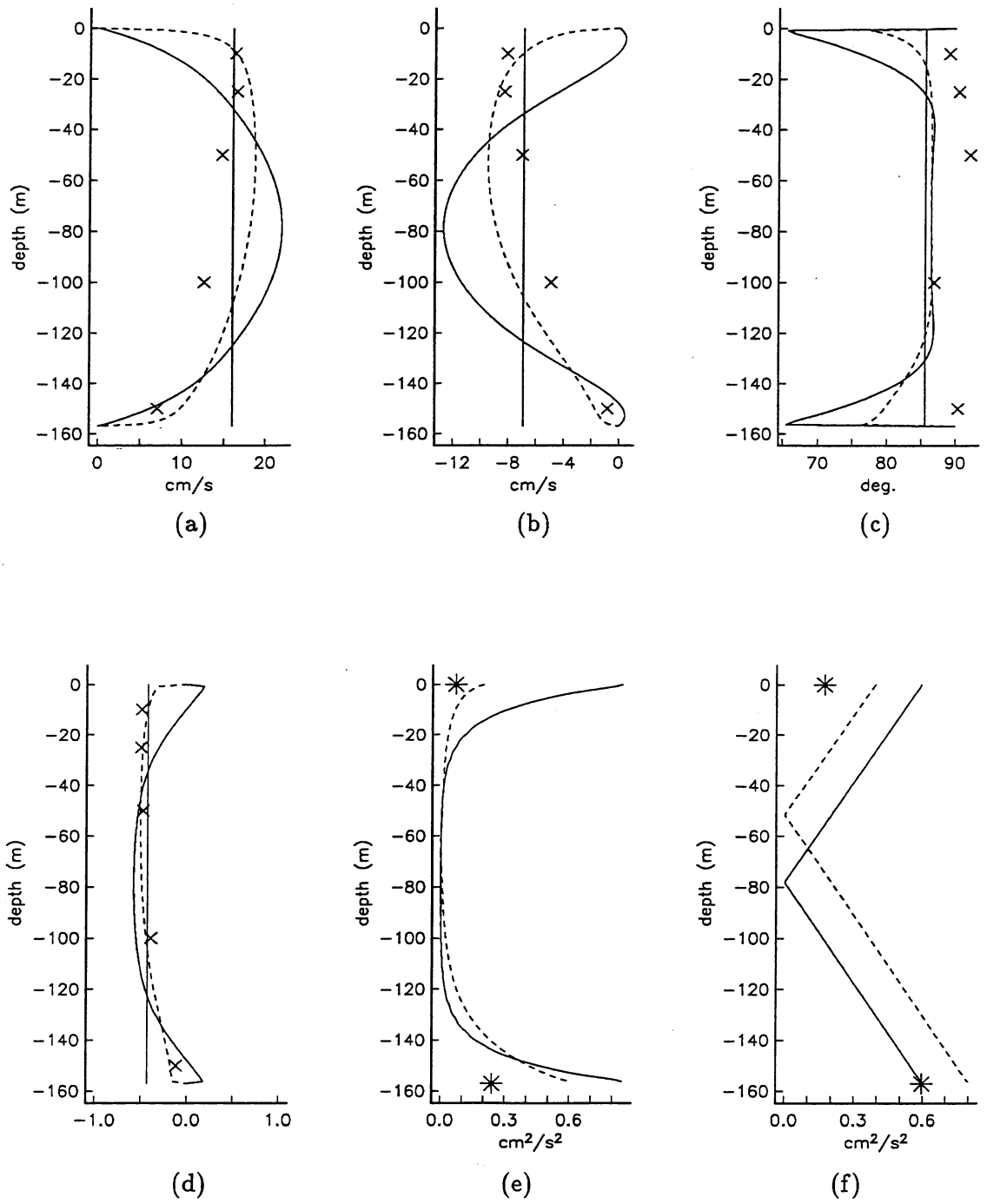

Figure 30: *Computed M_2 tidal current profiles at station S3 (75°20'N 24°59.4'E), water depth 157 m, for two eddy viscosity profiles; (———) and (- - - -) fig.1a and d respectively. (a) A major semi axis, (b) B minor semi axis, (c) θ azimuth orientation, (d) B/A eccentricity, (e) $|T_+|/\rho$ shear stress and (d) $|T_-|/\rho$ shear stress. × indicate the observed current data, the straight line represent the depth mean values and ∗ is the bed and surface stresses from the depth integrated model.*

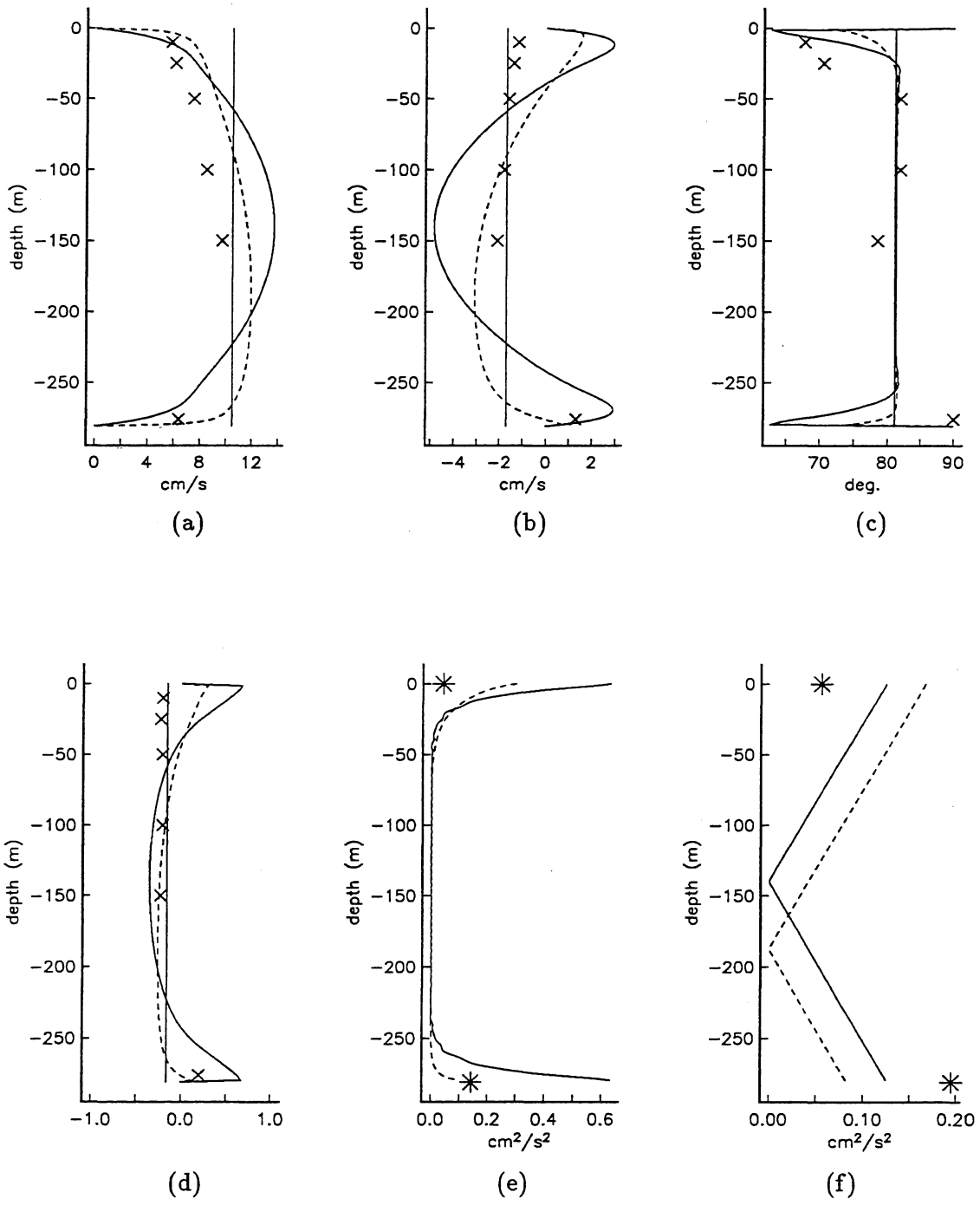

Figure 31: *Computed M_2 tidal current profiles at station S4 (75°2'N 27°6.9'E), water depth 281 m, for two eddy viscosity profiles; (———) and (- - - -) fig.1a and d respectively. (a) A major semi axis, (b) B minor semi axis, (c) θ azimuth orientation, (d) B/A eccentricity, (e) $|T_+|/\rho$ shear stress and (d) $|T_-|/\rho$ shear stress. × indicate the observed current data, the straight line represent the depth mean values and $*$ is the bed and surface stresses from the depth integrated model.*

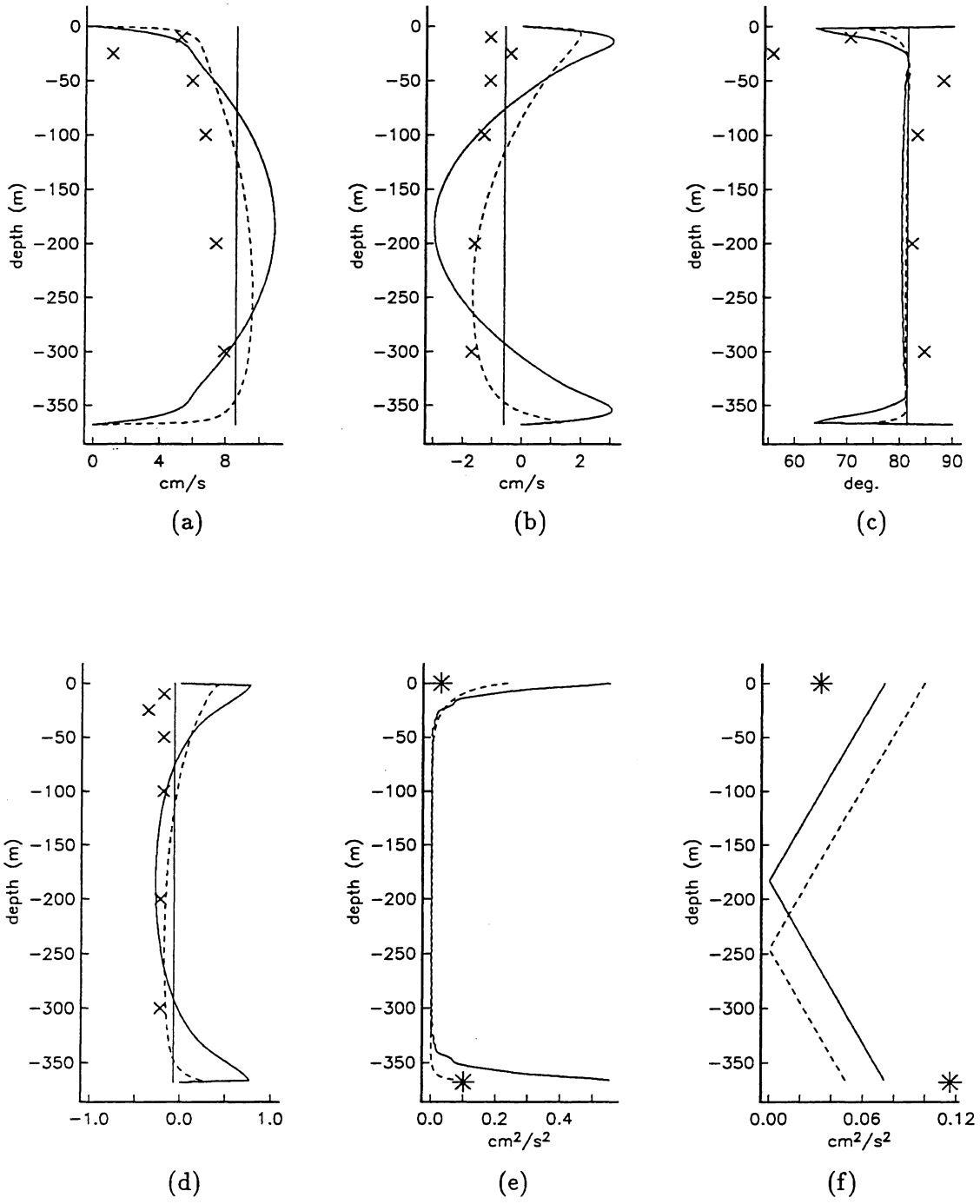

Figure 32: *Computed M_2 tidal current profiles at station S5 (74°51.2'N 28°43.3'E), water depth 368 m, for two eddy viscosity profiles; (———) and (- - - -) fig.1a and d respectively. (a) A major semi axis, (b) B minor semi axis, (c) θ azimuth orientation, (d) B/A eccentricity, (e) $|T_+|/\rho$ shear stress and (d) $|T_-|/\rho$ shear stress. × indicate the observed current data, the straight line represent the depth mean values and ∗ is the bed and surface stresses from the depth integrated model.*

6. Conclusions

The method of extracting current profiles from two dimensional hydrodynamic models, developed by Davies (1986, 1990), is presented for a general time dependent flow and for periodic motion as tidal wave. Both presentations include an arbitrary depth distribution of the eddy viscosity, but the latter is restricted for time independent eddy viscosity and for linear motion in time. The presentation includes various sea bed and sea surface boundary conditions, and we have focused on the consistency requirements of the method. Consistency require equal depth mean current, bed shear stresses and sea surface shear stresses from the two dimensional model and from the resulting current profiles.

The calculations of tidal current profiles with a constant eddy viscosity show that tidal current profiles in water deeper than the near bed stress layer, is sensitive to the magnitude of the eddy viscosity within the near bed stress layer, and above this stress layer the tidal current is essentially constant at its free stream value. Tidal current profiles in water shallower than the near bed stress layer, is sensitive to the magnitude of the eddy viscosity in the entire depth column.
Further the calculations presented here show no significant difference in the depth variations of the semi-diurnal M_2 constituent and of the diurnal K_1 constituent at geographical latitudes around the North Sea (55.6 °N). Here the thickness of the near bed stress layer is of the same order of magnitude for the two tidal constituents considered. Similar calculations at a latitude further north (74.3 °N) show that the M_2 tidal current profiles change their depth distribution more dramatic. The M_2 current profiles become more sensitive to variations in viscosity magnitude where the bed stress layer exceeds the water depth, even for very deep water. While the K_1 current profiles remain about the same as at 55.6 °N.
The thickness of the stress layer goes to infinity at the critical latitudes. The conclusion is that the tidal current profiles becomes very sensitive to variations of magnitude of eddy viscosity at positions close to the critical latitude for the considered tidal constituent. Near the critical latitude the thickness of the stress layer exceeds the water depth and goes to infinity at the critical latitude.

When the tidal current profiles are calculated with different eddy viscosity profiles, the entire method of extracting current profiles from two-dimensional hydrodynamic models is applied. The M_2 and K_1 tidal current profiles are calculated at positions located in the Barents sea where we have current observations. The tidal current calculations show acceptable good agreement with the observations at these positions.
The depth distribution of the M_2 current ellipse parameters are very sensitive to eddy viscosity variations in the Barents sea, and the current profiles are more sensitive in variations in the eddy viscosity the closer to the critical latitude the calculation positions are. For the M_2 constituent the thickness of the stress layer exceeds the water depth in the Barents sea, and the M_2 current profiles computed with various eddy viscosity depth distributions give different results in the entire water column. The M_2 current profiles depend strongly on changes of eddy viscosity profiles compared to the profiles of the K_1 constituent. The various K_1 current profile calculations with various eddy viscosity profile differ only in the near bed region i.e. within the bed boundary layer, and above this layer the profiles are approximately equal and constant in depth. The thickness of this near bed layer becomes larger relative to the total water depth as the water depth becomes shallower and as the calculations are done closer to

the critical latitude for the K_1 constituent.
These different current profile characteristics of the M_2 and K_1 tidal constituent may be explained by the location of critical latitude of the two constituents. The position where the calculations are done are close to the M_2 critical latitude and far away from the K_1 critical latitude.
The eccentricity here defined as the ratio minor to major semi-axis of the current ellipse, is not very sensitive to variations of the eddy viscosity profiles. The computed eccentricity agree very well with the observed, even though the computed semi-axis do not agree with the observed as well as the eccentricity. At stations with deep water the eccentricity of the M_2 current ellipse is close to zero and changes sign from minus to plus near sea bed. By this means that the M_2 current ellipse changes direction of rotation from anticyclonic direction at sea surface and mid-depth to cyclonic in the near bed region. This change of direction of rotation is not found for the K_1 current ellipse. In shallower water ϵ is closer to -1 and about constant with depth i.e. the M_2 current ellipse is more circular and rotates anticyclonic in the entire depth column, which is also the case for the K_1 constituent. These different results in deep and shallow water are robust due to variations of eddy viscosity profiles and are confirmed by the observations.
The value of the eddy viscosity in the calculations is determined such that the resulting current profile have the same depth mean current as in the depth integrated two-dimensional model. The viscosity value obtained when a constant eddy viscosity profiles is applied, is to high, while the layered eddy profile (fig. 1 b) gives viscosity values at sea bed and surface in the same range as indicated by Davies (1985). Generally the viscosity values obtained in the current profile calculations represent reasonable estimates.
Concerning the consistency of the bed shear stresses, calculations with the layered and the linear eddy profile (fig. 1 b, c) give best result. Further the anticyclonic stress component gives better consistency than the cyclonic, and we have obtained better consistency results for the M_2 constituent compared to the K_1 constituent.
To find the optimal eddy viscosity profile for the calculated current profile we must consider how the current at different depth agrees with observations (if observations are available), if the viscosity values represent physical reasonable estimates and which eddy profile that gives best consistency of the shear stresses at the boundaries.

The method of extracting current profiles from two-dimensional hydrodynamic models is also applied for calculating tidal current profiles under an ice covered ocean surface. The M_2 tidal current profiles are calculated at four stations where we have current observations under ice and which are located near the M_2 critical latitude.
The current profiles for these stations are classified in two groups. The observed current in the first group with relative strong current and shallow water, decreases with depth and the current ellipse is rotating cyclonic at all depth. The observed current in the second group with weaker current velocity and deeper water, increases with depth with a maximum below mid depth and the current ellipse changes direction of rotation in the near bed region. The calculations with a two layer eddy viscosity profile (fig1d) give current characteristics close to the observed. For the first group the surface eddy viscosity layer is thinner than the bed eddy viscosity layer, and for the second group the bed eddy layer is thinnest.

References

[1] Bowden K. F., Fairbairn L. A. and Hughes P. (1959)
The distribution of shearing stresses in a tidal current.
Geophysical journal of the Royal Astronomical Society, 2, pp 288–305.

[2] Butkov E. (1968)
Mathematicl Physics.
Addison–Wesley Publishing Company. Reading, Massachusetts.

[3] Davies A. M. (1983)
Formulation of a linear three-dimensional hydrodynamic sea model using a Galerkin – Eigenfunction method.
International Journal for Numerical Methods in Fluids, Vol. 3, pp 33–66.

[4] Davies A. M. (1985)
On determining current profiles in oscillatory flows.
Appl. Math. Modelling, Vol. 9, pp 419–428

[5] Davies A. M. (1986)
Numerical Modelling of marine systems.
Numerical Modelling – Application to Marine Systems -ed J. Noye Published North - Holland.

[6] Davies A. M. (1987)
On extracting current profiles from vertically integrated numerical models
Coastal Engineering , 11, pp 445–477

[7] Davies A. M. (1988)
On formulating two-dimensional vetically integrated hydrodynamic models with an enhanced representation of bed stress.
Journal of Geophysical Research, Vol. 93, No. C2, pp 1241–1263.

[8] Davies A. M. (1990)
On extracting tidal current profiles from vertically integrated two-dimensional hydrodynamic models
Journal of Geophysical Research, Vol. 95, No. C10, pp 18,317–18,342.

[9] Davies A. M. and Furnes G. K. (1980)
Observed and computed M_2 tidal currents in the north sea.
Journal of Physical Oceanography of Coastal and Shelf seas, No. 35, pp 189–266.

[10] Davies A. M. and Jones G. K. (1990)
Application of a three-dimentional turbulence energy model to the determination of tidal currents on the Northwest European shelf.
Journal of Geophysical research, Vol. 95, No. C10, pp 18,143–18,162.

[11] Fang G. and Ichiye T. (1980)
On the vertical structure of tidal current in a homogeneous sea.
Geophys. J. R. Astr. Soc., 73, pp 65–82.

[12] FINLAYSON B. A.(1972)
The Method of Weigthed Residuals and Variational Principles, with application in Fluid Mechanics, Heat and Mass transfer.
Vol. 87 in Mathematics in Science and Engineering. Academic press.

[13] FLATHER R. A (1976).
A tidal model for the north west European shelf.
Mém.Soc.Roy.Sci. Liége 6, X, 141–164.

[14] FOLDVIK A., MIDDLETON J. H. AND FOSTER T. D.(1990).
Tides in the southern Weddell Sea.
Deep-Sea Research, Vol. 37, No. 8, pp. 1345–1362.

[15] GJEVIK, B., NØST, E., AND STRAUME, T., (1990)
Atlas of tides on the shelves of the Norwegian and the Barents Seas.
Report Inst. of Math., Univ of Oslo, Oslo,Norway.

[16] MARCHUK G. I. AND KAGAN B. A. (1984)
Ocean tides. Mathematical Models and Numerical Experiments.
Pergamont Press. Translation editor D. E. Cartwright.

[17] MESINGER F. AND ARAKAWA A. (1976)
Numerical methods used in atmospheric models.
GARP publication series No 17, 64 pp.

[18] NØST, E. (1988)
Simulation of tides in the Haltenbank area; depth mean values and current profiles.
Cand.Scient thesis, Inst. of Math., Univ of Oslo,Norway.(in norwegian)

[19] PRANDLE D. (1982)
The vertical structure of tidal currents.
Geophys. Astrophys. Fluid Dynamics, Vol. 22, pp 29–49.

[20] SCHWIDERSKI,E,W., (1980)
On charting global ocean tides.
Rev.Geophys. and Space Physics 18,243-268.

[21] SOULSBY R. L. (1983)
The bottom boundary layer of shelf seas.
Physical Oceanography of Coastal and Shelf seas, editor B. Johns, Elsevier Oceanography Series, No. 35, pp 189–266.

[22] SIELECKI A. (1968)
An energy-conserving difference scheme for the storm surge equations.
Monthly Weather Review, Vol. 96, No.3, pp 150-156.

[23] SVERDRUP (1926)
Dynamic of tides on the North Siberian Shelf
Geophys. Publ., 4 75 pp

[24] WOLF J. (1980)
Estimation of shearing stresses in a tidal current with application to the Irish sea.
In: Marine Turbulens, J. C. J. Nihoul, editor, Elsevier, pp 319–344.

[25] RODI W. (1980)
Turbulence models and their applications in hydraulics : a state of the art review.
Delft 1980 - XII, 104p

[26] WILKINSON J. AND REINSCH C. (1971)
Handbook for Automatic Computation.
Vol II, Linear Algebra, Springer Verlag pp 241–248.

[27] ZITMAN T. J. (1990)
Analysis of the vertical structure of the horizontal current velocity components.
Progress Report, Delft Hydraulics, The Netherlands.